**TECHNISCHE
UNIVERSITÄT
WIEN**
Vienna University of Technology

Master Thesis

Optimization of a cloud chamber for the production of snow by CFD methods

Flow simulations using ANSYS Fluent under given general conditions

In partial fulfilment of the requirements for the degree of

Master of Science

under supervision of

Ass.Prof. Dipl.-Ing. Dr.techn. Michael Harasek
(E166 Institute of Chemical Engineering)
Proj.-Ass. Dipl.-Ing. Christian Jordan
(E166 Institute of Chemical Engineering)

submitted to TU Wien

Faculty of Mechanical and Industrial Engineering

by

Christian Mahr

0825485 (066 482)

Stockwiese 13

2474 Gattendorf

Wien, im Juni 2017   _____

Christian Mahr

Acknowledgements

Allen voran möchte ich mich bei Michael Bacher bedanken, der in den letzten zwei Jahren nicht nur mein Arbeitgeber, sondern oft auch Mentor und Motivator war. Auch wenn der Zeitraum für eine Diplomarbeit ein verhältnismäßig langer war und vermutlich nicht nur mein Durchhaltevermögen auf die Probe gestellt hat, konnte ich in den vergangenen beiden Jahren viele Erfahrungen machen, die ich mit großer Sicherheit sonst nicht gemacht hätte.

Weiters möchte ich mich bei David Mazur, Michele Battistin, Aniko Rakai, Martin Doubek und Manuel Gómez Marzoa bedanken, mit denen ich in Genf bei CERN zusammenarbeiten durfte. Ohne die Hilfsbereitschaft und die Motivation dieser Kollegen hätte die Kollaboration zwischen der Neuschnee GmbH und dem CERN auch nicht stattfinden können.

Mein Dank gilt auch Christian Jordan, der mich bis zum Schluss wegweisend unterstützt und motiviert hat und in für mich ausweglos scheinenden Situationen die richtigen Worte gefunden hat. Danke auch an Professor Harasek, der mich betreut hat und auch eingewilligt hat, das Thema noch einmal aufzurollen. Dies hat nach langem Stagnieren letztendlich den notwendigen Anstoß gegeben, durch den ich letztendlich doch meine Diplomarbeit zu diesem Thema zu Ende zu bringen konnte.

Von Anbeginn und auch im Laufe meines Studiums hat mich besonders meine Familie immer bedingungslos unterstützt und meine Pläne verständnisvoll akzeptiert, auch wenn ich oft nicht den direkten Weg gegangen bin sondern manchmal ebendieser eher das Ziel war als der Abschluss.

Danke auch an Johannes, Ullrich, Ursula, und alle anderen Involvierten der Neuschnee GmbH, die mit mir diesen Weg gegangen sind und mit denen ich Erfahrungen und Erlebnisse der letzten beiden Jahre teilen durfte.

Abstract

This master thesis treats the further development of an artificial cloud, which includes a 3D numerical model and field research at the actual prototype.

The process aims to produce snow of dendritic structure. Inside the cloud chamber two-component nozzles perform the atomization of water into small droplets. Some of the tiny water particles serve as ice nuclei and the rest of the water droplets convert into water vapour. The water vapour adheres to the ice nuclei so they can grow to snow crystals. For numerical modelling, the ANSYS software package Fluent was used which is suitable for parallel processing and therefore allowed the performance of calculations at the computational clusters of TU Wien and the European Organization for Nuclear Research.

Within the master thesis, empirical measurements of the jets, using the medium air, were executed and compared to analytical equations at transonic conditions. Results of the measurements showed a high correlation to outcomes of the analytical calculations. Findings were used to define inlet boundary conditions of the numerical model. Furthermore, the work treats the generation and comparison of different meshes, aiming to represent the components and geometry used within the process. An airflow model was setup to compare two numerical solvers, the influence of different near-wall models and turbulence modelling using several Reynolds-averaged Navier-Stokes-equations (RANS).

Results of the comparison show that high near-wall resolutions are not favourable for grid qualities and therefore downgrade convergence behaviour of the model. Furthermore the influence of near-wall treatment to jet spreading needs to be treated carefully. Calculation results could be achieved in about 10 % of iteration steps with the pressure-based, coupled solver, compared to the density-based, explicit solver. Also, the k-ε turbulence models showed faster convergence behaviour, compared to the other RANS models, while results developed the same way after a certain calculation time with all tested turbulence models. Numerical results of the flow field could not be validated on-site because of missing measurement methods and components.

Despite to the neglecting of water droplets, ice crystals and water vapour in the numerical model of the cloud chamber, outcomes of this thesis already represent the foundation of a numerical model for an artificial cloud.

Further knowledge on the prototype performance relating environmental conditions could be achieved by the performance of field measurements.

Kurzfassung

Diese Masterarbeit behandelt die Weiterentwicklung einer künstlichen Wolke. Das beinhaltet den Aufbau eines numerischen 3D Modells und die Feldforschung am Prototypen selbst.

Der behandelte Prozess zielt auf die Produktion dendritischer Schneekristallen ab. In der Wolkenkammer wird Wasser von Zweistoffdüsen zerstäubt. Einige der erzeugten Wassertropfen dienen als Eisnukleatoren, während der Rest der Tröpfchen zu Wasserdampf umgewandelt wird. Dieser bindet sich an die Eiskeime, womit Schneekristallen wachsen können. Für die numerischen Simulationen wurde die ANSYS Software Fluent verwendet. Diese ist für parallele Berechnungen gut geeignet, was die Verwendung der Computercluster an der Technischen Universität Wien und an der Europäischen Organisation für Kernforschung möglich macht.

Im Rahmen der Masterarbeit wurden empirische Messungen der Düsen mittels Luft durchgeführt und mit analytischen Gleichungen bei transsonischen Bedingungen verglichen. Die Resultate der Messungen und der analytischen Berechnungen zeigten hohe Übereinstimmungen. Die Ergebnisse wurden für die Definition der Eintritts-Randbedingungen des numerischen Modells verwendet. Weiters behandelt die Arbeit die Erstellung und den Vergleich verschiedener Gitter zur Diskretisierung. Ein Modell reiner Luftströmung wurde aufgebaut und zwei numerische Solver, der Einfluss verschiedener Wandfunktionen und die Behandlung von Turbulenz unter Verwendung verschiedenen RANS-Modellen wurde verglichen.

Ergebnisse der Vergleiche zeigen Probleme bei hohen Gitterauflösungen in Wandnähe, und folglich problematisches Konvergenzverhalten des Modells. Weiters ist die Ausbildung des Düsenstrahls sensibel gegenüber der Wandfunktion. Rechenergebnisse konnten unter Verwendung des Druck-basierten, gekoppelten Lösers in rund 10 % der Berechnungszeit im Vergleich zum Dichte-basierten, expliziten Lösers erreicht werden. Weiters zeigten die k-ε Turbulenzmodelle ein schnelleres Konvergenzverhalten, im Vergleich zu den restlichen RANS-Modellen, wobei nach einer gewissen Anzahl an Iterationsschritten sehr ähnliche Ergebnisse bei den getesteten Turbulenzmodellen erreicht wurden. Eine Validierung der numerischen Ergebnisse am Prototypen konnte wegen fehlender Messverfahren und –komponenten im Rahmen dieser Arbeit nicht durchgeführt werden.

Trotz der Vernachlässigung von Wassertropfen, Eiskristallen und Wasserdampf in der numerischen Simulation repräsentieren die Ergebnisse bereits ein brauchbares Fundament für ein numerisches Modell einer künstlichen Wolke.

Weitere Ergebnisse des Betriebsverhaltens des Prototypen in Relation zu den Umgebungsbedingungen konnten durch empirische Messungen erreicht werden.

Table of Content

List of figures

List of tables

Nomenclature

Name	Declaration	Unit
A	cross section of a vortex tube	[m^2]
b	Molecular volume of water in ice	[m^3/mol]
C	pre-exponential factor	[1]
C_D	Drag coefficient	[1]
c_p	specific heat	[J/(kg·K)]
D	jet perimeter	[m]
d	total differential	[1]
d_0	characteristic length	[m]
E	cross diffusion term	[1]
e	unity vector	[1]
F	force	[N]
ΔF	molar free energy	[J/mol]
G	generation of turbulent kinetic energy	[J/kg]
g	gravity	[m/s^2]
ΔG	Gibbs energy	[J/mol]
h	potential height	[m]
J	Arrhenius energy	[J/mol]
k	turbulent kinetic energy	[J/kg]
k_B	Boltzmann constant = $1,38064852*10^{-23}$	[J/K]
L	latent heat	[J/kg]
n	normal vector	[1]
p	pressure	[Pa]
P	equilibrium vapour pressure	[Pa]
q	heat energy per unit mass	[J/kg]
r	radius	[m]
R	specific gas constant = 287,058	[J/(kg·K)]
Re	Reynolds number	[1]
S	saturation ratio with respect to solid ice	[%]
t	time	[s]
T	temperature	[K]
ū	mean velocity	[m/s]
u'	velocity fluctuation compensation in x-direction	[1]
v	velocity	[m/s]
v'	velocity fluctuation compensation in y-direction	[1]
w'	velocity fluctuation compensation in z-direction	[1]
We	Weber number	[1]
x	position variable	[m]
X	dissipation rate due to turbulence	[1]

x'	turbulence fluctuation variable	[1]
y	interfacial energy between ice and supercooled water	[J]
Y	contribution of fluctuation dilatation in compressible turbulence to overall dissipation rate	[1]
α	Prandtl number	[1]
γ	control angle of a spherical ice nucleus on a flat surface	[°]
ε	turbulent dissipation rate	[J/(kg·s)]
ζ	energy barrier reduction in comparison to homogenous nucleation	[J/kg]
λ	linear interpolation factor	[1]
κ	isentropic exponent	[1]
μ	dynamic viscosity	[m^2/s]
ν	molecular volume of water in ice	[m^3]
ρ	density	[kg/m^3]
σ	surface tension	[Pa]
τ	stress tensor	[Pa]
ω, Ω	vorticity	[s^{-1}]

Indices

Name	Declaration
c	cubic
D	drag
E	node forward in the interpolation scheme
e	evaporation
F	fluid
fus	fusion
G	gravity
g	gas
het	heterogeneous
hex	hexagonal
i	ice
l	liquid
P	actual point of calculation
p	constant pressure
r	radial axis
s	solidification
turb	turbulence
W	node backward in the interpolation scheme
z	z-axis

φ,Φ	angular axis
0	v point
1	index 1
2	index 2

1 Introduction and Background

1.1 Motivation

Tourism is a substantial mainstay of Austria's economy. In 2013, just under 25 millions of international tourists were accounted. This corresponds to a worldwide market share of 2,3 % and equals about three times the inhabitants of Austria. [1] Furthermore, about 7 % of the country's GDP was generated by the tourism sector.

To stay competitive, snow guarantee counts as prerequisite for ski resorts and winter tourism in general. In order to fulfil these requirements, gigantic amounts of energy, water and financial resources are required. The annual water consumption of artificial snowmaking for the alp's slopes in 2004 amounts to about 93 million m^3, which equals that of a city with 1,5 million inhabitants. Energy consumption of the Alps' snow machines equals the usage of about 130 000 four-person households [2].

Looking at this conflict of interest between economic growth and ecological sustainability, it is necessary to develop a solution approach. Declared aim, therefore, is economic growth in a sustainable way in order to create a basis of value that lasts.

Based on this context on one hand, and the passion for powder skiing on the other hand, the idea to build a machine producing snow of dendritic structure was created. Using less energy for snow making, producing snow of excellent quality and getting to know more about ice nuclei generation were the main goals at the starting point of the project.

Former works of Michael Bacher et al [3] [4] have documented the development of a method that enables the production of powdery snow. In laboratory experiments, this procedure of nature-like snow crystal growth could actually be re-produced. The evolved system introduces atomized water and pressurized air in a cylindrical container in tangential direction. Pressurized air is cooled down to very low temperature levels and a creation of ice nuclei is forced locally. By creating an oversaturation of water vapour inside that volume, it adheres to the ice nuclei and creates snow crystals. Water and air properties are measured before their introduction to the cloud chamber and inside the vessel [3]. **Figure 1.1** shows the experimental setup. The achievement of the laboratory experiment is the production of dendritic snow and it's regulation via temperature and mass flow rate of introduced air and water. **Figure 1.2** shows the microscopic image of hexagonal snow crystals, produced in the cloud chamber at University of Natural Resources and Life Sciences Vienna (BOKU).
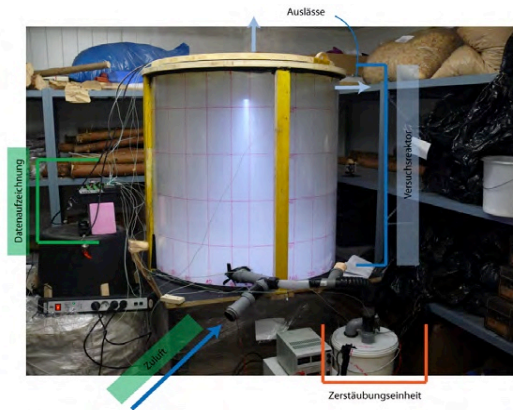
Figure 1.1: Cloud chamber BOKU Vienna [3]
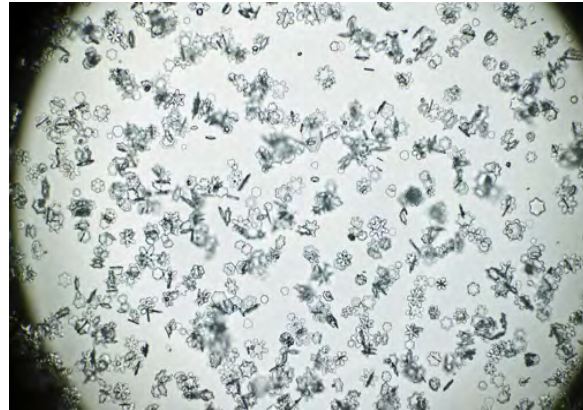
Figure 1.2: Microscopic image of snow produced during a test run in the cold chamber of BOKU Vienna [3]

The Neuschnee GmbH is a spin-off from the Technische Universität Wien (TU Wien) and the University of Natural Resources and Life Sciences Vienna. It was founded by Michael Bacher. Amongst others, one of the company's research goals was to build up an open-air laboratory in order to realize snow production in outdoor conditions. Achieved knowledge of the laboratory experiments should be applied and adapted to variable operating conditions. Tests were executed through the winter season 2014/15. A second prototype was built up during the winter season 2015/16, taking gained experience into account and further optimizing the process with regard to increased snow output.

1.2 Research Goal

For this thesis the main goal is to develop a 3D numerical model, and therefore generating knowledge on flow patterns and crystal spreading inside the snow machine. This should be achieved by applying the ANSYS Fluent [5] numerical code. Despite general guidelines for airflow simulations, no similar models are present in literature. The work presented is aimed at the analysis of the problem to the creation of a stable, numerical model. The process should be approached numerically and turbulence formation should be analysed. Therefore several turbulence models should be compared. Also, the influence of solvers on the model's stability is a topic. Furthermore heat production inside the dendrite generator and heat transfer between the cloud chamber and its surrounding should be regarded. As it was not possible to measure conditions in the real cloud chamber properly due to missing measurement methods and instruments, a comparison of the results to the numerical model cannot be made at this point. Outcomes of this work should represent a basic model, building the base for the further development of a cloud chamber model including phase changes and snow crystal formation, validated to a real future process.

2 Fundamentals and preliminary considerations

In this chapter, main parts of the cloud chamber itself will be described briefly to give an idea of the components that should be represented in the numerical model. Furthermore, fundamentals on essential physical properties in the cloud chamber will be discussed. An overview of ice crystal formation will be given, vortex formation will be characterized and the atomization process, used with nozzle technology will be a topic.

2.1 Cloud chamber

Figure 2.1 shows a schematic illustration of the cloud chamber prototype, constructed in SketchUp [6]. Visible here are the basic steel construction, the wooden platform around it and the PVC shell, which is featured transparently. The entire construction measures 8,5 m in height, while the PVC shell has dimensions of 6 m in height and diameter. What is not illustrated are the hydraulic and pneumatic pipeline systems that provide water and air for the applied nozzles, which are a central part of the cloud chamber. In the following chapter a closer look on shell technology, nozzle features and the chamber construction will be taken. Furthermore, relevant measurement techniques will be discussed.
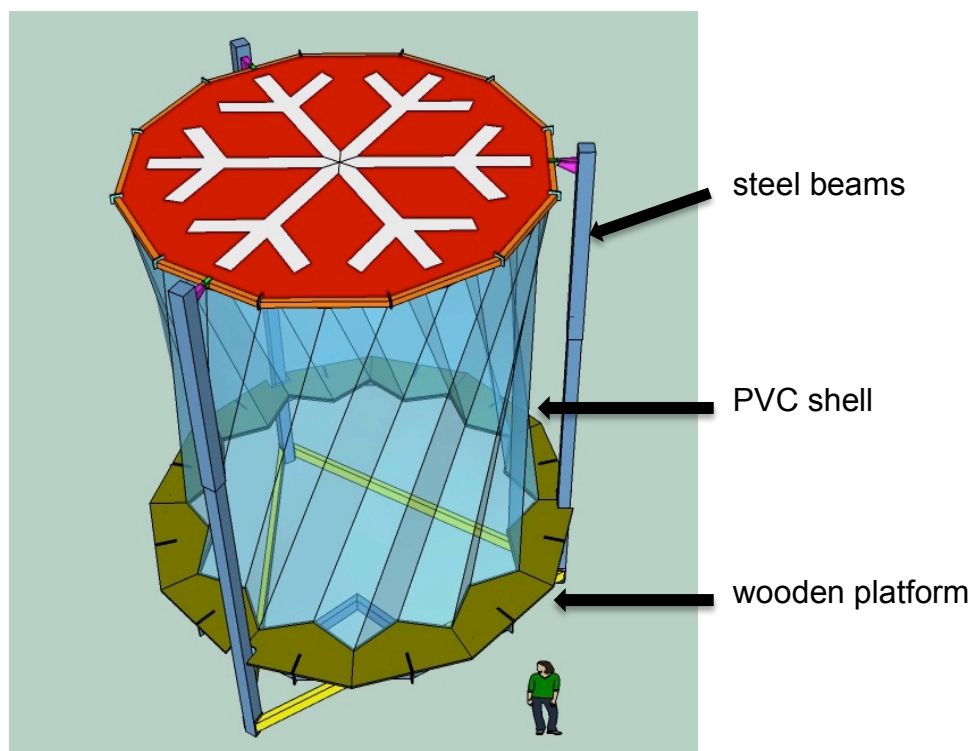
Figure 2.1: Cloud chamber design

2.1.1 Shell technology

The PVC cover forms the shell of the cloud chamber. It is an essential part, as it makes the process more controllable. Unlike snow lances and cannons, a majority of the atomized water is processed to snow in a delimited volume and losses are only present if desired for the purpose of cooling. This will be discussed further in Chapter 7 "Cooling Tower Analogy".

Therefore, requirements the shell of the cloud should fulfil are lightness in weight, stability, and favourable heat transfer properties and in ideal case the cover should be adjustable to enable a change of the cloud chamber size. Analysing these facts, a braced PVC tarpaulin was chosen to be the right material. The company *Koch Industries, Inc.* supported us by providing the needed hardware and know-how.

The technology, applied by our partner enables the application of a PVC cover, which is a tear-resistant, rather light material. Very stable surfaces and constructions can be formed by the application these techniques. As there is no pressure load, applied to the walls of the cloud chamber, this method combines advantages perfectly. The material is brought into its form via aluminium rails at the bottom and top of the cover. The jagged form was chosen to enlarge the surface of the chamber, which is favourable for the heat transfer. The surface of the PVC shell measures 137 m^2.

2.1.2 Basic construction

Basically, the applied construction is a hydraulically adjustable tripod built of square steel girders. Hydraulic components are responsible for inclination adjustment in order to enable positioning at uneven sites. Furthermore they enable the tensioning of the shell. A lower steel ring represents both, a static load-carrying element and the working platform. The total construction measures 9,11 m in height at fully extended status. Construction plans are provided in Appendix A.

2.1.3 Nozzle technology

Supplier of the applied nozzles is the company *Spraying Systems Co*. The challenge of nozzle selection is to obtain a high flow rate of water and small droplet sizes at the same time. The technology used, to fulfil this, is based on the parallel influx of water and air. A hollow cone spray pattern is produced through atomization of liquid via compressed air and an internal mix impingement atomization forms droplets in a micrometre-range.

Droplet sizes vary in a range between 15 and 400 μm, depending on water and air pressure. [7]

Figure 2.2 shows a sectional view of the applied nozzles. More information on the jets is captured in Appendix B. Further review of the analytical perspective on the atomizing process and influencing parameters are given in Chapter 2.2.2 "Basics on the atomization process".
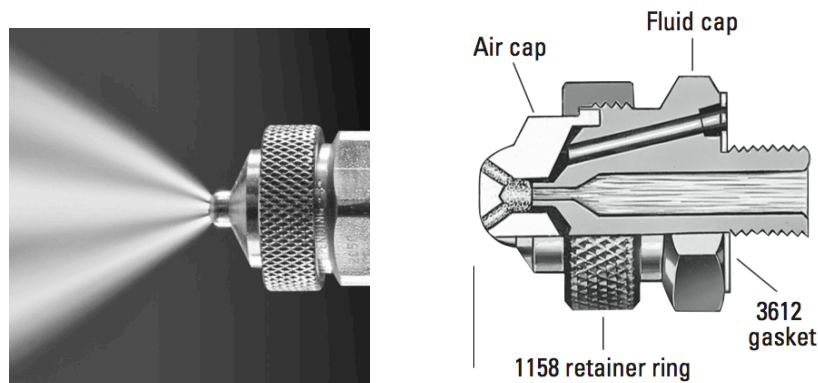
Figure 2.2: Nozzle scheme [7]

2.2 Fundamentals - physical processes

The process, which underlies the production of powdery snow, is the controlled reproduction of hexagonal ice crystal formation in a way it can be observed in natural clouds as well. To enable crystal growth, ice crystals should be kept in the air as long as possible. This should be achieved by a rotating flow field. A central ingredient of the process is water in its different states. In the following, properties of the mentioned will be discussed.

2.2.1 Water – its phases and changes

Water as a substance, probably studied more than any other matter [8], is present in the atmosphere in three different states, which are liquid as water, solid as ice and gaseous as vapour. It can be transferred into its different physical states by supplying or removing thermal energy. Every phase transition underlies different processes, illustrated in **Figure 2.3**. Between the gaseous and the liquid state condensation and evaporation take place, between the liquid and solid state, transformation processes are called crystallization and fusion (melting). Phase change between the solid and gaseous state is called sublimation and deposition.
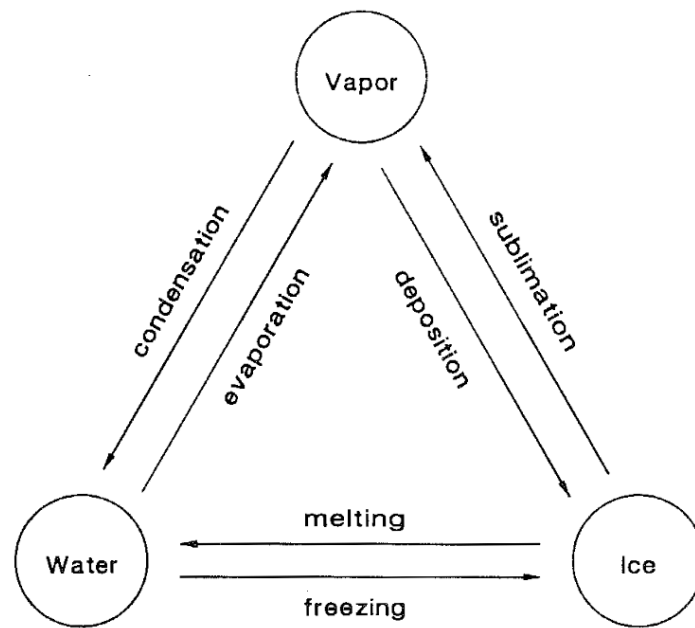
Figure 2.3: Nomenclature for phase transition in the water system [9]

In analogy to natural clouds, some of these processes take place in the cloud chamber. Condensation happens when water vapour deposits on small water droplets where the vapour deposits. The process of crystallization takes place in form of developing ice nucleus, which can grow further on.
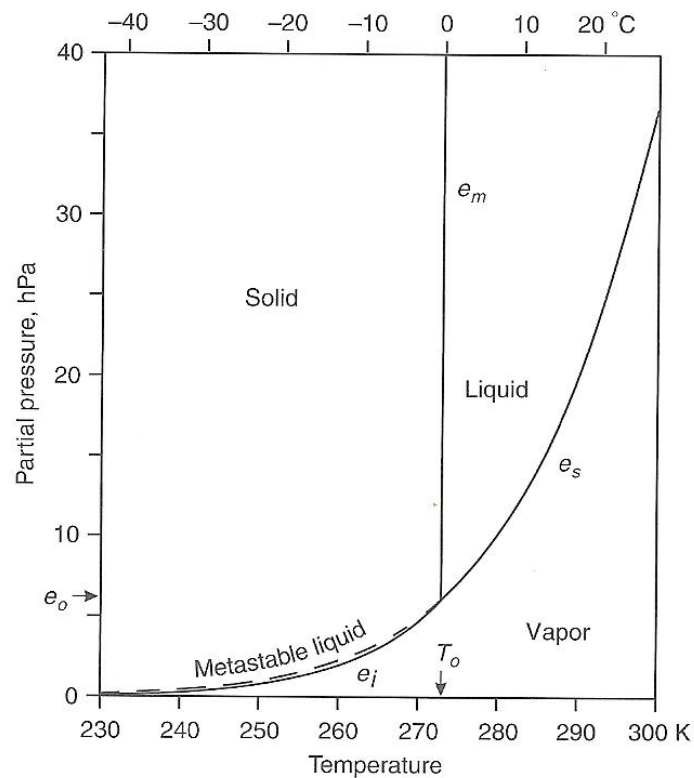
Figure 2.4: Phase diagram of pure water [10]

Figure 2.4 shows a pressure temperature diagram of water, also showing curves of phase changes. The development of cloud particles is determined by the process of nucleation. The nucleation processes can occur via formation of water drops through condensation or freezing. The process of nucleation will be examined in Chapter 2.2.1.3.

As mentioned before, the enforcement of the process requires addition or removal of energy. In other words, water has to be heated or cooled to initiate the processes, which is connected to the motion of molecules. Heating leads to an augmentation, cooling to a reduction of molecular activity. The amount of energy required to heat a unit mass of water by one degree Celsius is called the specific heat.

2.2.1.1 Specific heat

Specific heat, more generally, is the ratio between the amount of heat added to one mass unit of water and the resulting change in temperature. It can be defined regarding constant volume or pressure. If adding an amount of heat to a material, assuming constant volume, the internal pressure will raise. On the other hand, assuming constant pressure, the material can extend and increase its volume without changing the internal pressure. Regarding the atmospheric conditions, interest lies at the specific heat at constant pressure of 1 atm, which is defined by:

$$c_p = \frac{dq}{dT}$$ (2-1)

where dq is the quantity of heat given to an unit mass and dT is the temperature change due to the added heat [11]. The specific heat is different for different temperature of the substance. Furthermore the specific heat of water vapour is more sensitive to such variations in temperatures than the specific heat of dry air. Data, found in literature is related to temperatures above 0 °C. But the results of Krauss [12] are based on the empirical polynomial equation for the calculation of the specific heat of water at the gaseous state $c_{p,g}$ for temperatures between 237,16 K and 373 K:

$$c_{p,g} \left[\frac{J}{kg \cdot K}\right] = 1,3824 * 10^3 + 6,3974 * T - 2,9274 * 10^{-2} * T^2 + 4,524 * 10^{-5} * T^3$$ (2-2)

Additionally the polynomial fits for water in the solid and liquid state, $c_{w,i}$ and $c_{w,l}$, are derived from experiments of Speedy [13] and Tombari et al [14], respectively:

$$c_{p,i} \left[\frac{J}{kg \cdot K}\right] = 1,315 * 10^2 + 7,2105 * T$$ (2-3)

$$c_{p,l} \left[\frac{J}{kg \cdot K}\right] = 4,1243 * 10^3 + \frac{1,79348 * 10^6}{(T - 222)^{2,5}}$$ (2-4)

Figure 2.5 shows the specific heat for each phase between 240 and 275 K:
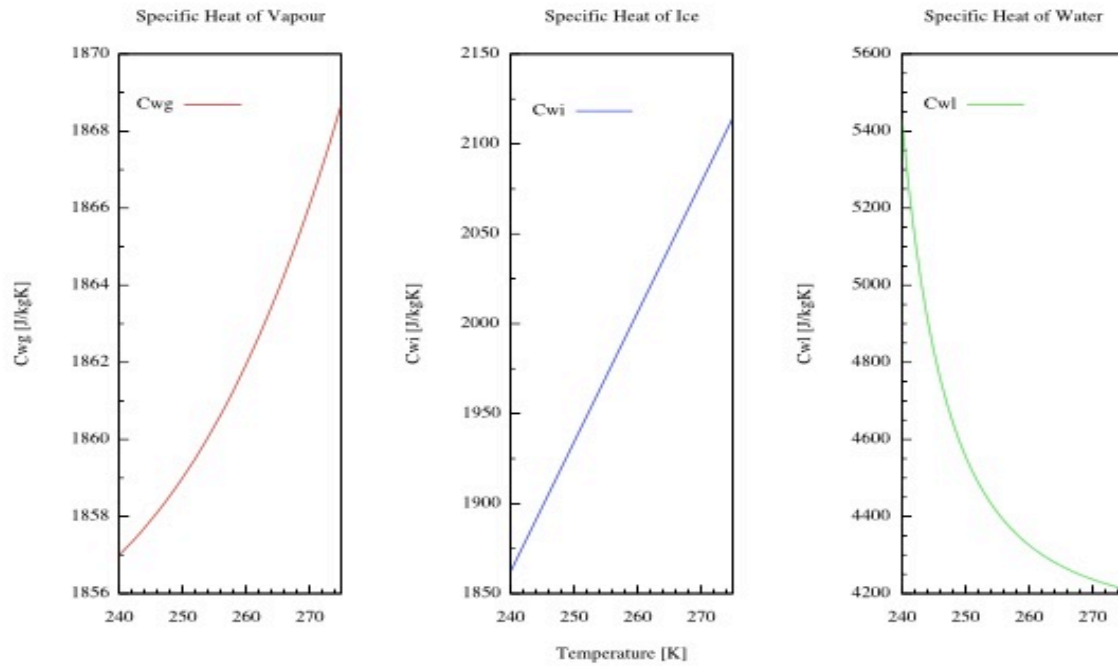
Figure 2.5: Specific heat of gaseous, liquid and solid water at 1 atm [15]

2.2.1.2 Latent heat

An additional amount of heat, the so called latent heat, is released or supplied once the water, regardless in which state it is, reaches the temperature of phase change from. In other words, latent heat is the energy that has to be removed or supplied to transfer a substance from one phase to another. In general it is defined by the difference between the heat content (in our case the specific heat under constant pressure) of the two phases involved. The following relations can be derived from evaluation of the Kirchhoff's equations [15]:

$$\frac{dL_e}{dT} = C_{p,g} - C_{w,l}; \quad \frac{dL_S}{dT} = C_{p,g} - C_{p,i}; \quad \frac{dL_m}{dT} = C_{p,l} - C_{p,i}; \qquad (\,2\text{-}5\,)$$

where L_e, L_s and L_m represent the latent heat for evaporation, sublimation and melting, respectively.

And from the law of energy conservation (first law of thermodynamics) follows at the triple point (0,01 °C):

$$L_S = L_e + L_m \qquad\qquad (\,2\text{-}6\,)$$

Combining the equation of specific heat (2-1) with the equations of latent heat (2-5) and solving the result by integration using the reported heat capacities leads to the following relations:

$$L_s[\tfrac{J}{kg \cdot K}] = 2{,}65898 * 10^6 + 1{,}2509 * 10^3 * T - 0{,}40655 * T^2 - 9{,}758 * 10^{-3} * T^3 +$$
$$1{,}131 * 10^{-5} * T^4 \qquad (\,2\text{-}7\,)$$

$$L_e[\tfrac{J}{kg \cdot K}] = 3{,}14369 * 10^6 - \frac{3{,}61472*10^2 - 1{,}62825*T}{(4{,}5045*10^{-3}*T-1)^{2,5}} - 2{,}7419 * 10^3 * T + 3{,}1987 * T^2 -$$
$$9{,}758 * 10^{-3} * T^3 + 1{,}131 * 10^{-5} * T^4 \qquad (\,2\text{-}8\,)$$

$$L_m[\tfrac{J}{kg \cdot K}] = -4{,}8476 * 10^5 + \frac{3{,}61473*10^2 - 1{,}62825*T}{(4{,}5045*10^{-3}*T-1)^{2,}} + 3{,}9928 * 10^3 * T - 3{,}6053 * T^2 \;(\,2\text{-}9\,)$$

An evaluation of these equations for temperatures between 240 K and 273,15 K is shown in **Figure 2.6**:
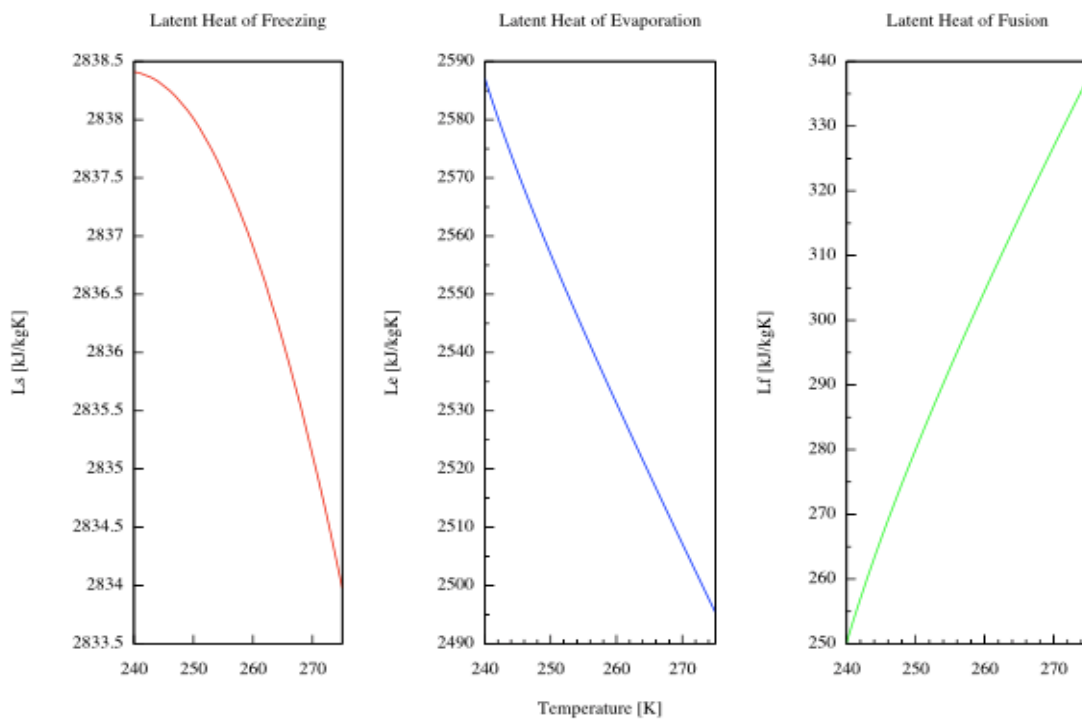
Figure 2.6: Latent heat of sublimation, evaporation and fusion calculated from (2-6), (2-7) and (2-8) [15]

2.2.1.3 Ice crystal formation

Aiming to grow a snowflake, an ice nucleus (IN) of hexagonal structure is needed. In fact, it builds the base for a snowflake. The process, by which supercooled fluids form stable, crystalline solids, is statistical in nature and because of the set of intermediate states, very short-lived [16]. There are several ways, ice formation in clouds can happen. Forms of nucleation can be separated in two main groups, namely homogenous and heterogeneous ice formation. In **Figure 2.7**, homogenous freezing and three mechanisms that account for the group of heterogeneous ice nucleation are illustrated.
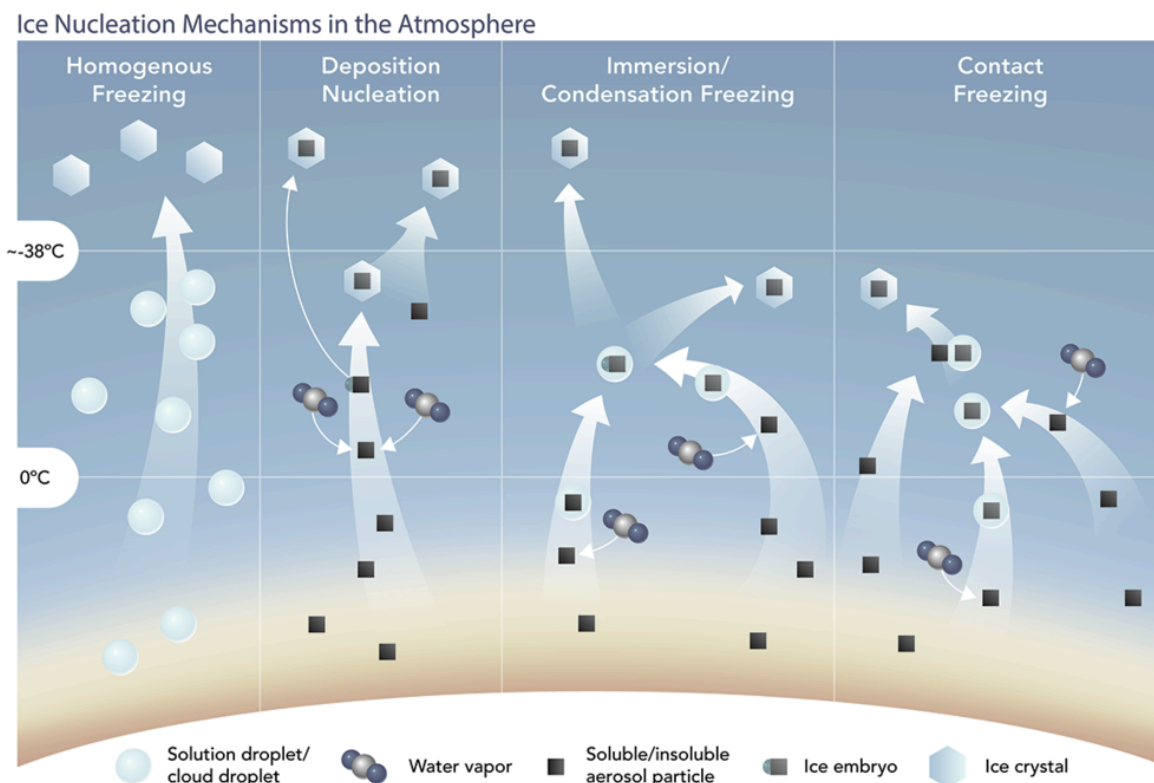
Figure 2.7: Ice nucleation mechanisms [17]

Homogenous crystal formation

At the very left, the process of homogenous freezing can be observed. For this process, no additional substances are part of the ice crystal formation, and a homogenous structure of water droplets in the air fulfils the requirements for the formation of ice nuclei. The unique properties of water in supercooled (metastable) state are not fully understood. Thus, a well-known fact is the independence of crystal formation to the nature of the aqueous solution, present in the water droplets, and its relation to the water activity. Koop et al defines water activity as the "ratio between the water vapour pressure of the solution and of pure water under the same conditions" [18]. Ice crystals grow due to the difference of water vapour pressure between ice and super cooled water. Fine water droplets experience spontaneous ice formation at temperatures below 235 K referring to ambient conditions.

The metastable state, where this spontaneous process is possible, is called Ostwald-Miers region. Homogenous formation of IN happens when the ice nuclei is crossing the border of the critical nuclei radius. In order to form an ice cluster of critical size, above which the cluster will grow spontaneously into a macroscopic crystal, a certain energy gap is required. This difference in energy levels can be described as the Gibbs energy, which can be written the following way:

$$\Delta G = \frac{16\pi y^3 b^2}{3(k_B T \ln S)^2}$$

(2-10)

in which y is the interfacial energy between ice and supercooled water, v is the molecular volume of water in ice, k_B is the Boltzmann constant, T is temperature and S is saturation ratio with respect to solid ice (either I_h or I_c). S is defined as

$$S = \exp\left(-\frac{\Delta F_{fus}}{RT}\right) = \frac{P_l}{P_i}$$

(2-11)

where ΔF_{fus} is the molar free energy of fusion and P_l is the equilibrium vapour pressure over a flat liquid water surface, P_i is the equilibrium water vapour pressure over a flat ice surface and R is the gas constant. [19]

The Arrhenius equation introduces the correlation of the Gibbs energy and the nucleation coefficient. It can be written for both, homogeneous and heterogeneous crystal formation. For the homogeneous case, the equation (2-12) is valid for ζ = 1.

Heterogeneous crystal formation

The other ways of ice crystal formation, described in **Figure 2.7**, account for the category of heterogeneous ice crystal formation. Heterogeneous ice formation on the substrate of dust aerosols is initiated by the nucleation of an ice embryo, often thought of as a spherical cap, on which the macroscopic ice crystal can grow. Which one of those nucleation models is the most efficient and therefore the dominant process of ice formation depends on the temperature and saturation history of an ice-forming particle, the particle properties and the ambient conditions, the particle experiences.

Deposition nucleation is the formation of critical ice clusters on the surface of an insoluble aerosol. Ice nuclei form directly from the vapour phase. Two possible mechanisms of formation (referred to as Type 1 and Type 2) have been described by Federer [20] and Pruppacher and Klett [16] :

- Type 1: A critical ice germ forms on an active site, primarily by surface diffusion of adsorbed water molecules to this site.
- Type 2: Critical ice germs grow directly by adsorption of water molecules from the ambient air.

Requirements, necessary for the formation of a stable ice cluster, were clearly expressed by Welti et al [21]: "The amount of water molecules necessary to form a stable ice cluster from the vapour phase depends on the properties of the IN substrate, temperature, and relative humidity with respect to ice (RH_i). Deposition nucleation can take place as soon as saturation with respect to ice is exceeded."

Immersion freezing occurs when an aerosol particle first serves as a cloud condensation nucleus (CCN). Afterwards, the cloud droplet needs to be supercooled down to a temperature where ice nucleation is catalyzed on the particle-water interface in order to cause the particle to freeze. Immersion freezing is an important mechanism for ice formation in mixed-phase clouds and has been implied to dominate heterogeneous cirrus cloud formation via freezing of solution droplets containing IN. [22]

Ice formation is attributed to condensation freezing when water condenses on an IN at supercooled temperatures (T < 273 K) and ice nucleation spontaneously occurs without further cooling of the condensed water. When a liquid water layer forms on the IN surface, four processes that favor ice formation could take place (which will be referred to as forms of condensation freezing numbered I, II, III, and IV).

(I) refers to nucleation during the process of water condensation at the growth boundary of condensing water clusters where water molecules have higher degrees of freedom or entropy than in the bulk. [23]

In (II), a subcritical ice cluster formed from the vapour phase could be incorporated into a growing water cap as proposed by Cooper [24]. This process favours ice nucleation by allowing an ice cluster, subcritical in the vapour phase, to become stable in the water phase where the critical radius is smaller (i.e., fewer water molecules are required to form a critical ice germ).

(III) is nucleation in capillary condensed water. Ice embryo formation in small confinements is facilitated owing to the reduced chemical potential of capillary-held water caused by the capillary pressure. [21]

The fourth form (IV) is mechanistically equivalent to ice nucleation by immersion freezing. A critical embryo forms at the interface of the condensed water and the particle substrate.

The last form to account for this group of heterogeneous ice crystal formation is called **contact freezing**. This expression refers to the initiation of the ice nucleation process by contact of an interstitial particle with a supercooled water droplet. A nucleation process similar to the condensation freezing mechanism, described above, might then initiate freezing. [21]

The Arrhenius equation for heterogeneous ice nuclei formation can be written the following way:

$$J_{het}(T) = C_{het}\exp\left(-\frac{\Delta G * \zeta}{kT}\right) \qquad\qquad (\,2\text{-}12\,)$$

Where C_{het} het is a pre-exponential factor and φ is the factor by which the presence of a solid surface reduces the height of the energy barrier relative to homogeneous nucleation. This factor is depending on the ice nucleating efficiency parameter, m:

$$\zeta = \frac{(2+\cos(\gamma))(1-\cos(\gamma))^2}{4} \qquad (\text{2-13})$$

γ describes the contact angle of a spherical ice nucleus on a flat surface. When referred to in literature, values of γ can be understood as a semi-empirical measure of a material's ice nucleation catalysation property. [19] [25] [26]

Ice crystal processing in the cloud

Water and air is introduced in the cloud chamber. This happens via the application of two-fluid nozzles.

Due to high velocities at the exit of the nozzles, the effect of expansion cooling is proceeding. The cooling process, happening in this area is responsible for temperatures in a very low range. In fact, theory of compressible fluids let estimate temperatures in a region below 235 K. Analytical calculations on compressible fluid flow are listed in Appendix C.

By the application of air and water filtration systems the level of particles inside the cloud should be kept as low as possible, which is mandatory for controlled ice nuclei processing in the cloud. Low temperatures at nozzle exits favour local spontaneous ice nuclei formation. Clean air and water should prevent from different, heterogeneous forms of nucleation and therefore regulate IN production. By controlling the number of ice nuclei, a controlled snow crystal growth should be achieved. By controlling the relation of water vapour to the number of ice nuclei, the amount of water vapour per ice nucleus should be controlled.

2.2.2 Basics on the atomization process

In this chapter, an overview of the atomization process, using water-jets will be given in order to give an understanding of atomization.

A clear definition of atomization can be found in Bayvel et al [27]: "The process of atomization is one in which liquid is disintegrated into drops by the acting forces." Thin jets or sheets of liquid are a favourable form to disintegration because they have a high surface energy and therefore a great instability. It follows that atomizing nozzle applications must first develop jets or sheets of liquid. Crucial phenomena for the further development into particles are waves on the liquid surface. Breakup conditions can be generated nearby and further from the outlet of the nozzle in dependence of the waves on the liquid surface. The disintegration from sheets or jets into droplets is called primary breakup. Kinetic forces between the surrounding gas

and the droplets cause further breakup into smaller droplets. This process is called secondary breakup. **Figure 2.8** shows a picture, taken by a high-speed camera. It illustrates the primary and secondary breakup zones of a hollow cone nozzle spray.
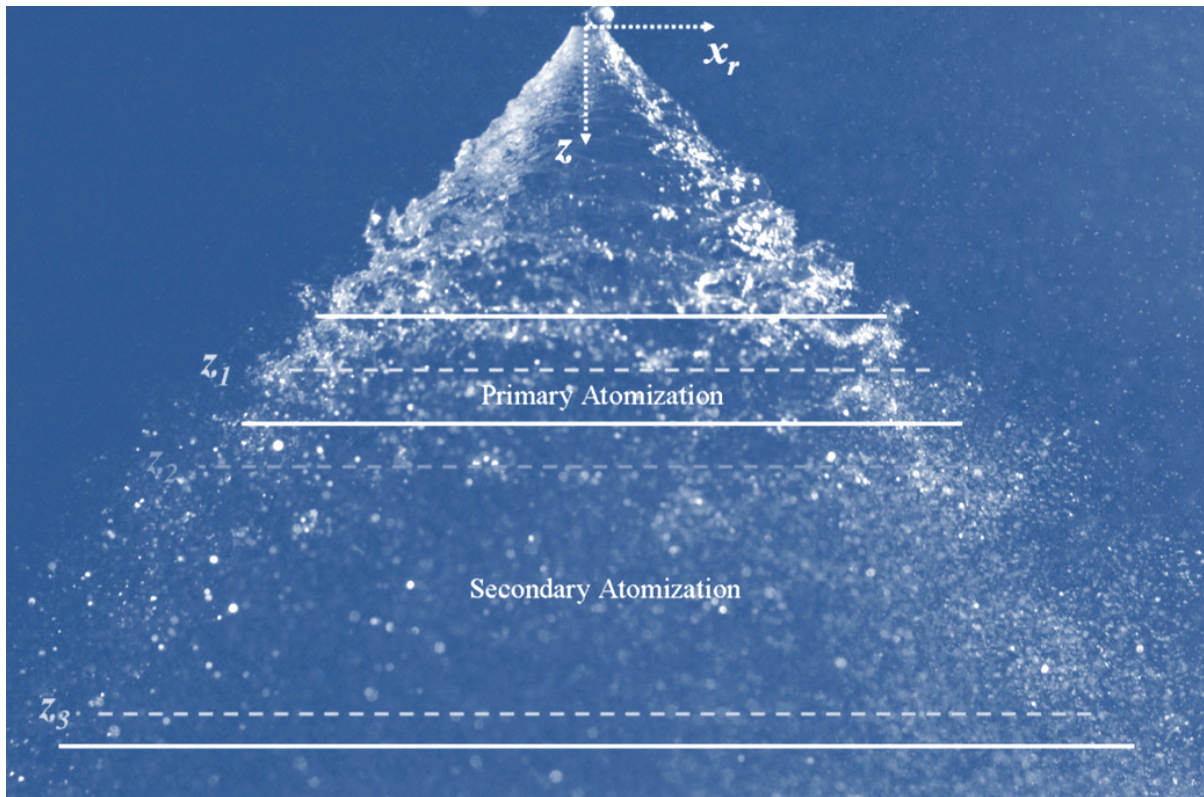
Figure 2.8: Hollow cone nozzle spray breakup zones [28]

2.2.2.1 Primary breakup

The primary breakup process for liquid jets can be classified by the velocity of discharge from the nozzle. There are three characteristic forms of disintegration, caused by axisymmetric waves, asymmetric waves and aerodynamic forces.
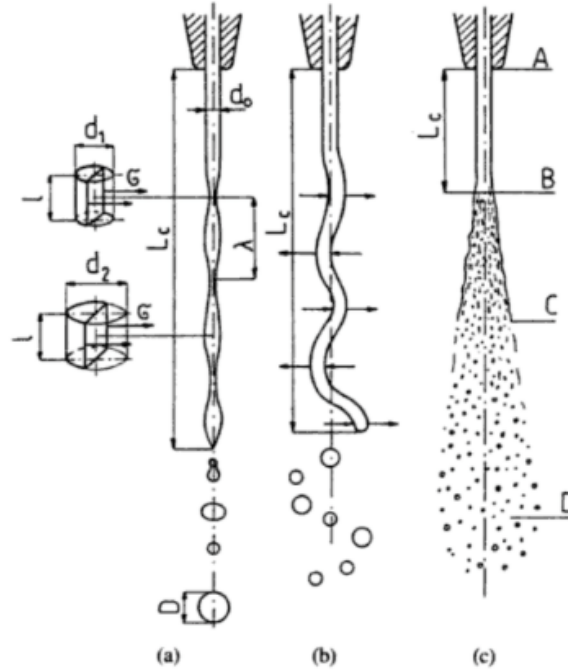
Figure 2.9: Disintegration of a cylindrical jet of liquid caused by **(a)** axialsymmetric waves, **(b)** asymmetric waves, **(c)** aerodynamic forces [27]

For axisymmetric waves, the loss of surface tension on the liquid surface is responsible for the sheet breakup. Rayleigh's solution [29] on the breakup model concludes in a jet breakup under the condition that the wavelength is bigger than the perimeter of the jet. Weber [30] included the fluid viscosity to Rayleigh's solution, which ends up in:

$$\frac{D}{d_0} = 1{,}436 \left(1 + 3 \frac{We_l^{0.5}}{Re} \right)^{1/6}$$

(2-14)

where We_l is the Weber number

$$We_l = \frac{\rho_l v_l^2 d_0}{\sigma}$$

(2-15)

and Re the Reynolds number

$$Re_l = \frac{\rho_l v_l d_0}{\mu_l}$$

(2-16)

for liquids, respectively. The variable D represents the jet perimeter and d_0 is the characteristic length. [27]

For an increase of discharge velocity, the jet is influenced more and more by aerodynamic forces that cause distortions of its axis (**Figure 2.9 (b)**). The air moving along the jet accelerates in the vicinity of convexities and decelerates in the vicinity of concavities in the jet. Overpressure and underpressure develop under the influence of asymmetric waves, and the jet disintegrates into smaller drops than those produced by axisymmetric waves. If aerodynamic forces are even bigger, direct disintegration into smaller droplets is possible.

2.2.2.2 Secondary Breakup

The theory of atomization also includes the disintegration of drops into smaller droplets, which proceed within the flow in a gaseous medium. Attempts, similar to the theory of primary breakup have been made but failed due to severe deformations of the drop.

Deformations of droplets make it difficult to derive drop drag coefficients. The critical weber number for droplet breakup was calculated under the assumption of symmetrical droplet deformation with respect to the flow direction and constant influence of normal and shear stresses. [27] Further literature is not taken in account, as the theory on it is adapted on every specific case.

2.2.3 Compressible fluid flow

If velocities higher than Ma = 0,3 occur within a gas flow, it cannot be seen as incompressible any more. In that case, analytic fluid mechanics refers to the energy equation of compressible fluids [31]. The first simplification, which is done here, is that air is treated as an ideal gas.

An ideal gas is considered to be composed of randomly moving point particles that do not interact except when they collide elastically. The ideal gas concept is useful because it obeys the ideal gas law, a simplified equation of state, and is amenable to analysis under statistical mechanics. At normal conditions such as standard temperature and pressure, most real gases behave qualitatively like an ideal gas. Many gases such as nitrogen, oxygen, hydrogen or noble gases can be treated like ideal gases within reasonable tolerances. [32]

The energy equation for an ideal gas [31] has the following form:

$$\frac{u_2^2}{2} + \frac{\kappa}{\kappa-1} \cdot \frac{p_2}{\rho_2} + g \cdot h_2 = \frac{u_1^2}{2} + \frac{\kappa}{\kappa-1} \cdot \frac{p_1}{\rho_1} + g \cdot h_1 \qquad (2\text{-}17)$$

whereas κ is the quotient of isotherm and isobar heat capacity.

$$\kappa = \frac{c_P}{c_v} \tag{2-18}$$

As in the formulas of the incompressible case, we are looking at a stagnation point case in the following paragraph. Additionally, the change of state is seen isentropic, which means that there is no entropy produced during the process. Under these conditions, the following isentropic correlations [30] are valid:

$$\frac{p_0}{p_1} = \left(\frac{T_0}{T_1}\right)^{\frac{\kappa}{\kappa-1}} \tag{2-19}$$

$$\frac{\rho_0}{\rho_1} = \left(\frac{T_0}{T_1}\right)^{\frac{1}{\kappa-1}} \tag{2-20}$$

Furthermore, the sound of speed for an ideal gas [30] is defined as:

$$c = \sqrt{\left(\frac{dp}{d\rho}\right)_s} = Ma \cdot \sqrt{\kappa R T} \tag{2-21}$$

This defines the value of Ma = 1 for conditions of given temperature and pressure of the jet case.

Technically, velocities above Ma = 1 can be reached through Laval nozzles. The problem of outpouring flow of a boiler through a plain orifice is the case that fits this jet problem as there is no Laval geometry applied to the used jets

The maximum velocity, which can be reached under those conditions is Ma = 1. Conditions for which the velocity at the smallest cross section is sonic are called critical flow conditions in terms of state-thermodynamics [30].
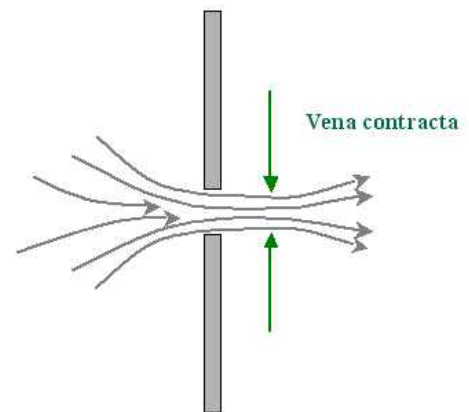

Vena contracta

Figure 2.10: Plain orifice [33]

$$\frac{p_{crit}}{p_0} = 0,528 \tag{2-22}$$

$$\frac{\rho_{crit}}{\rho_0} = 0,634 \tag{2-23}$$

$$\frac{T_{crit}}{T_0} = 0,833 \tag{2-24}$$

Figure 2.11 shows the pressure ratio in relation to the mass flow rate. Air velocity cannot increase above the value at the critical point, where Ma = 1 is reached. Mass flow although can be risen by increasing the upstream pressure further. Lowering the pressure at the outlet cannot increase the mass flow above the value at the critical
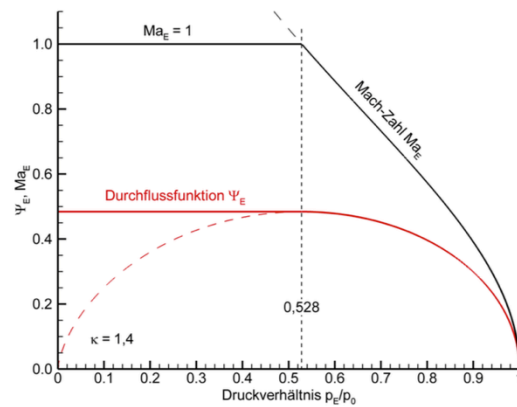
point.

Figure 2.11: Choked flow pressure vs. massflow [34]

Self-evident, mass flow and velocity at the orifice can also be calculated from isentropic relations [35]:

$$\dot{m} = \frac{p_{01} A^*}{\sqrt{T_{01}}} \sqrt{\frac{\kappa}{R} \cdot \left(\frac{2}{\kappa+1}\right)^{\frac{\kappa+1}{2(\kappa-1)}}} \tag{2-25}$$

$$v_{out} = \sqrt{\frac{2\kappa}{\kappa-1} \cdot \frac{p_0}{\rho_0} \left[1 - \left(\frac{p_1}{p_0}\right)^{\frac{\kappa-1}{\kappa}}\right]} \tag{2-26}$$

Referring to the conditions at the jet outlets, there are three cases, which can be distinguished:

- The pressure ratio $p_U/p_0 > 0{,}528$, implying that $p_U > p_{crit}$ and velocity at the outlet is subsonic. The gas is being expanded to $p_{exit} = p_U$ at the outlet, which influences the outlet velocity.

- The pressure ratio $p_U/p_0 = 0{,}528$ is just critical, so $p_U = p_{crit}$ and the velocity at the outlet is just sonic.

- The pressure ratio $p_U/p_0 < 0{,}528$, also meaning that $p_U < p_{crit}$. The flow velocity at the exit equals Ma = 1 and the pressure equals the critical pressure, so $p_{exit} = p_{crit}$. Just after the orifice, the jet is object to a post expansion. The jet is widened up and compressed alternately until the excessive pressure energy is compensated by friction. [34]

Illustrations for subcritical and critical conditions can be found in **Figure 2.12**, for supercritical conditions in **Figure 2.13.**
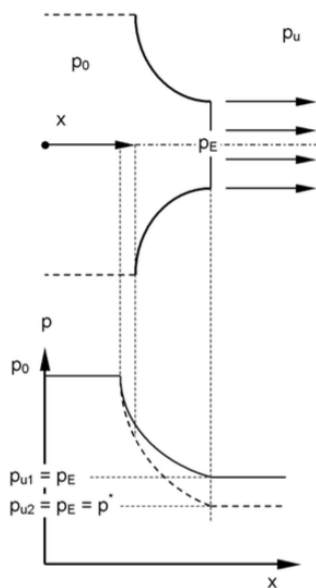
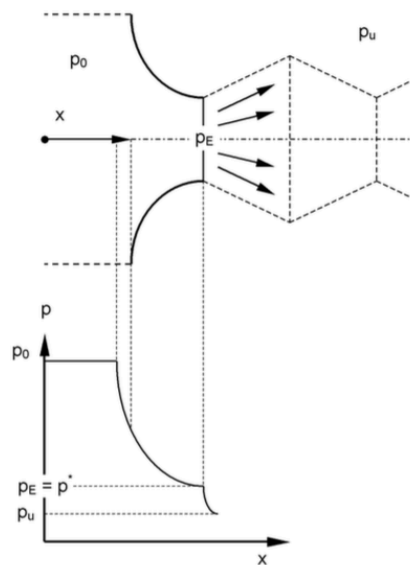**Figure 2.2**: subcritical, critical [34]   **Figure 2.13**: supercriticals [34]

In **Table 2.1**, values needed for the calculation of the compressible fluid flow problem related to the given case are listed. Furthermore the outcomes of the calculations are listed. These will be used for the definitions of the inlet conditions.

Table 2.1: Calculations for compressible fluid flow

A_SU16_measured	$7,53*10^{-7}$	m^2	Critical_pressuredrop	0,528	
A_SU26+26B_measured	$3,015*10^{-6}$	m^2	Critical_pressure@atm	$1,89*10^5$	N/m^2
R	287	J/(kgK)	Density_crit_pressuredrop	2,3305	kg/m^3
T	283,15	K	Density_out_isentropic	1,4769	kg/m^3
kappa_air	1,4		Temp_out_isentropic	235,95	K
			Speed_of_sound	307,90	m/s

2.2.4 Vortex

A very decisive parameter, concerning the fluidic design of the cloud chamber process is the formation of a vortex inside the cloud chamber and the control of the variables that influence the development of the above-mentioned.

2.2.4.1 Definition and general considerations

A clear and commonly valid definition of a vortex does not exist. A pretty vivid approach of explanation was done by Wu et al [36]:

"Vortices may be qualitatively defined as connected fluid regions with high concentration of vorticity. They include vortex layers and axial vortices with vorticity concentration in one and two spatial dimensions, respectively. An axial vortex is usually simply called a vortex; it represents the strongest existence form

of the vorticity field and the most important structures in at least low-Mach-number flows."

Helmholtz's vortex theorems are listed in the following section, in order to give a closer understanding for vortices.

2.2.4.2 Helmholtz' vortex theorems

There are difficulties with vortex quantifications and definitions. Helmoltz's vortex theorems give a clear basic idea of what a vortex is like. They are defined as follows:

(I) If a substantial fluid element is non-vorticial, it stays non-vorticial for all times:

$$\boldsymbol{\omega}(t = 0) = 0 \Rightarrow \boldsymbol{\omega}(t > 0) = 0 \qquad\qquad (2\text{-}27)$$

(II) If a substantial fluid element is situated on a vortex line at one instant, it is situated on the vortex line for all times, i.e. vortex lines 'move with the fluid'.

(III) The strength of a vortex is constant over time. [31]

The above-mentioned term vortex line is defined as follows:

"A vortex line is, at any particular time t, a curve which has the same direction as the vorticity vector

$$\boldsymbol{\omega} = \boldsymbol{\nabla} \times \mathbf{v} \qquad\qquad (2\text{-}28)$$

at each point." [37]

Figure 2.13 shows a vortex tube. Its boundaries are formed by vortex lines, which pass through simply structured, closed curves in space. Supposing an inviscid, incompressible fluid with constant density, moving due to a conservative force, then the second Helmholtz' vortex theorem is valid. [35] The condition of conservative body forces is given due to Kelvin's circulation theorem which is defined as :

$$\frac{d\Gamma}{dt} = 0 \qquad\qquad (2\text{-}29)$$

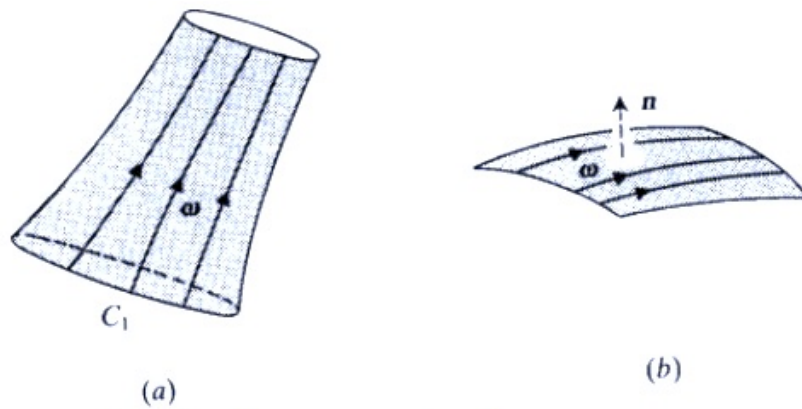This means that in a frictionless flow the circulation around a closed, substantial curve is constant in time [30].

Figure 2.14: Vortex tube (a) and vortex surface (b) [37]

"The quantity

$$\Gamma = \int_A \boldsymbol{\omega} \cdot \boldsymbol{n} \, dA \qquad\qquad (2\text{-}30)$$

is the same for all cross-sections A of a vortex tube. " [37]

A very descriptive illustration of a vortex' nature is given when observing a smoke ring. In the following part, a description, made by Acheson et al is shown:

"*In axisymmetric flow the vortex tubes are therefore ring-shaped around the symmetric axis. According to the first vortex theorem they move with the fluid. In doing so they will, in general expand and contract about the symmetry axis, and thus change in length. When in axisymmetric flow, an isolated vortex tube is surrounded by irrotational motion, we speak of it as a vortex ring. The familiar 'smoke-ring' is perhaps the most common example, and provides a vivid illustration of the Helmholtz vortex theorems, though the vortex core occupies only a fraction of the smoke ring as a whole.*" [37]

Figure 2.15: Vortex ring [38]

2.2.4.3 Vortex-related motion

Besides the Helmholtz' vortex theorems, some common definitions of rotational motion are presented. Following definitions of different vortex-related flow motions should give a further idea of what vortices can look like and how to differentiate between them.

Solid-state rotation

A simple vortex movement is given by the solid-state rotation with rotation speed Ω. Given the velocity field $v(r) = \Omega r$, vorticity equals:

$$\boldsymbol{\omega} = \boldsymbol{\nabla} \times \boldsymbol{v} = \boldsymbol{\nabla} \times \mathrm{v(r)}\boldsymbol{e_\varphi} = \frac{1}{r}\frac{\partial}{\partial r}rv(r)\boldsymbol{e_z} = 2\Omega\boldsymbol{e_z} \qquad (\,2\text{-}31\,)$$
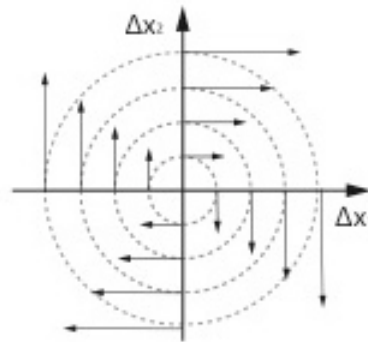
Figure 2.16: Solid state rotation [31]

Vorticity for a solid-state rotation is therefore constant. As the entire flow rotates by Ω, so does every fluid element around the centre of rotation. **Figure 2.15** shows streamlines and velocity vectors of a planar solid-state rotation.

Vortex-sink flow

A combined movement of a vortex and a sink can, for example, be observed in a cyclone-separator or at the outflow of a washbasin.

A favourable presentation of this movement can be made via potential theory.

Figure 2.17: Vortex-sink flow [31]

For the two flow patterns, two constants can be introduced:

$$C_1 dr = v_r r \qquad (2\text{-}32)$$

accounting for the sink flow

$$C_2 d\varphi = v_\varphi r \qquad (2\text{-}33)$$

accounting for the swirl flow.

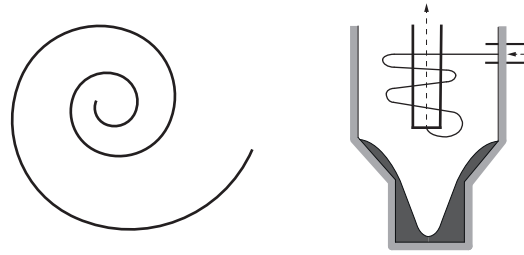Superimposing the equations of those two movements results in the following representation of velocity:

$$\boldsymbol{v} = \frac{C_1}{r}\boldsymbol{e}_r + \frac{C_2}{r}\boldsymbol{e}_\varphi \qquad (2\text{-}34)$$

which leads to the fact, that the relation of radial to azimuthal velocity is constant over the entire velocity field. [30]

$$\frac{v_r}{v_\varphi} = \frac{\frac{dr}{dt}}{\frac{rd\varphi}{dt}} = \frac{dr}{rd\varphi} = \frac{C_1}{C_2} = const. \qquad (2\text{-}35)$$

Lagrangian Coherent Structures (LCS)

Another concept that deals with swirling flow is the idea of coherent structures. In order to give another viewing point to the topic, this should be mentioned as well.

In general, any form of pattern arising in fluid flow that has an effect on transport is considered a coherent structure. Sections of a velocity field, having less mixing as in the rest of the flow structure are also called coherent. Wu et al gives the following definition of a coherent structure: "Vortices are coherent structures, and while the inverse is generally true, it is not necessarily so." [36]

Lagrangian Coherent Structures are coherent structures, identified by using methods of the Lagrangian field, which means that fluid flow structures are studied in terms of fluid trajectories [36]. A separation of LCS in attracting and repelling structures is

possible. Fluid particles either get pulled into or pushed away from the flow structure, which includes vortices in the first of the two groups. Results of the LCS-concept are partitioning the fluid in dynamically distinct regions. Therefore it is useful for finding the edges of a vortex.

2.2.4.4 Fluent's Physics of Swirling and Rotating Flows
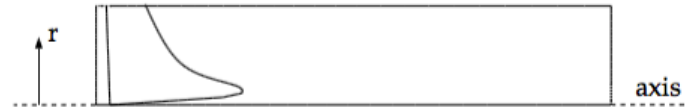

Figure 2.18: Typical Radial Distribution of ω in a Free Vortex [39]

As working with Fluent as main instrument to gain research results, its definitions with regard to simulation-outcomes should be mentioned as well. Fluent guidelines approach that "in swirling flows, conservation of angular momentum ($r\omega$ or $r^2\Omega = \mathrm{const.}$) tends to create a free vortex flow, in which the circumferential velocity, ω, increases sharply as the radius, r, decreases with ω decaying to zero near $r = 0$ as viscous forces begin to dominate." [40] A tornado is one example of a free vortex. **Figure 2.17** shows the radial distribution of ω in a typical free vortex.

It can also be shown that for an ideal free vortex flow there is equilibrium between the centrifugal forces, created by the circumferential motion, and the radial pressure gradient [40]:

$$\frac{\partial p}{\partial r} = \frac{\rho\omega^2}{r}$$

(2-36)

Most-likely dealing with non-ideal vortices, it should be mentioned that the evolvement of angular momentum also changes the form of its radial pressure gradient. As a result, radial and axial flows are created. Fluent therefore indicates changes in the distribution of static pressure and corresponding radial and axial velocities. According to Fluent's literature, "it is this high degree of coupling between the swirl and the pressure field that makes the modeling of swirling flows complex". [40]

2.2.4.5 Characteristic variables

The distribution of velocity and vorticity (the curl of the flow velocity) are used to characterize vortices. In most vortices, the fluid flow velocity is greatest next to its axis and decreases in inverse proportion to the distance from the axis. Once formed, vortices can move, stretch, twist, and interact in complex ways. In the following paragraphs, several quantification methods will be represented. Some of them will also be used to evaluate the numerical studies.

Vorticity

The most obvious approach in quantifying a vortex is to quantify the angular velocity, or vorticity, at a point of interest.

In the next step a mathematical definition of the index ω will be given. At first, the Navier-Stokes equation needs to be shown. In vector form it looks as follows:

$$\frac{\partial \boldsymbol{v}}{\partial t} + \boldsymbol{v} \cdot \nabla \boldsymbol{v} = -\nabla \left(\frac{p}{\rho} + gh\right) + \nu \nabla^2 \boldsymbol{v} \qquad (\,2\text{-}37\,)$$

By taking the curl of the Navier-Stokes equations the vorticity equation is obtained. In detail and taking into account $\nabla \times \boldsymbol{u} \equiv \boldsymbol{\omega}$ this results in

$$\nabla \times (\text{Navier} - \text{Stokes}) \rightarrow \nabla \times \frac{\partial \boldsymbol{v}}{\partial t} + \nabla \times (\boldsymbol{v} \cdot \nabla \boldsymbol{v}) = -\nabla \times \nabla \left(\frac{p}{\rho} + gh\right) + \nabla \times (\nu \nabla^2 \boldsymbol{v})$$

$$(2\text{-}38\,)$$

Assuming density as uniform, after some transformations, the vorticity equation can be written in its most common form

$$\frac{d\boldsymbol{\omega}}{dt} = (\boldsymbol{\omega} \cdot \nabla)\boldsymbol{v} + \nu \nabla^2 \boldsymbol{\omega} \qquad (\,2\text{-}39\,)$$

also implying fixed reference frames. [41]

Although it has an exact physical definition, its physical significance is still not clear. While circulation is a large-scale measure of rotation, vorticity is a microscopic, and therefore non-visible measure of rotation. Furthermore, vorticity is the cornerstone of circulation, and the individual locations of vorticity describe pure circulation. [42]

Fluent's Swirl Number

Another variable to characterize a swirling flow, also used by ANSYS Fluent, is the swirl number. The swirl number is defined as the ratio of the axial flux of angular momentum to the axial flux of axial momentum:

$$S = \frac{F_\theta}{L F_Z} \qquad (\,2\text{-}40\,)$$

where L is called the hydraulic radius or characteristic length.

The terms F_θ and F_Z are the axial flux of angular momentum and the axial flux of axial momentum, respectively and are given by

$$F_\theta = \int_0^\infty \rho u_z u_0 r^2 dr \qquad (\,2\text{-}41\,)$$

and

$$F_z = \int_0^\infty (\rho u_z^2 + p) r dr \qquad (\,2\text{-}42\,)$$

The swirl number has been shown to be an important similarity variable for geometrically similar swirl generators. [43] However, it should be used with caution when comparing the swirl intensity produced by different types of swirl generators. There is some uncertainty due to the choice of a characteristic length in (2-40) and S is often calculated neglecting the pressure term in (2-42).

Q-Criterion

In order to eliminate uncertainties in comparing swirl strengths, a second criterion should help out. In Holmén et al [44] a lucid comparison of vortex identification methods is given. Methods based on velocity gradient tensors are favourable to be implemented in Fluent due to it being based on the Navier-Stokes-equations. From the ones listed, the Q-criterion and Δ-criterion will be described.

This criterion looks at the second invariant of the velocity gradient tensor, Q. A vortex is defined as an area where

$$Q = \frac{1}{2}[|\mathbf{\Omega}|^2 - |\mathbf{St}|^2] > 0 \qquad (\,2\text{-}30\,)$$

where $\mathbf{St} = \frac{1}{2}[\nabla\mathbf{v} + (\nabla\mathbf{v})^T]$ ist the rate-of-strain tensor, and $\mathbf{\Omega} = \frac{1}{2}[\nabla\mathbf{v} - (\nabla\mathbf{v})^T]$ is the vorticity tensor. [45] [46]

For a three-dimensional smooth velocity field $\mathbf{v}(\mathbf{x}, t)$, available Galilean-invariant vortex criteria use the velocity gradient decomposition

$$\nabla\mathbf{v} = \mathbf{St} + \mathbf{\Omega} \qquad (\,2\text{-}31\,)$$

Δ-criterion

As well as the Q-criterion, the Δ-criterion is another Galilean-invariant criterion, by Chong, Perry & Cantwell [47]. According to them, a vortex core is a region of space where the vorticity is sufficiently strong to cause the rate-of-strain tensor to be dominated by the rotation tensor, i.e. the velocity gradient tensor ∇v has complex eigenvalues.

$$\mathbf{\Delta} = \left(\frac{Q}{3}\right)^3 + \left(\frac{det\nabla\mathbf{v}}{2}\right)^2 > 0 \qquad (\,2\text{-}32\,)$$

Whether the eigenvalues are complex can be determined by looking at the sign of the discriminant. [45]

3 Field research

Between January and March 2016, field experiments with the cloud chamber were executed. At first, the development and assembling of a system was performed. This included the building of the following components:

- Tripod steel construction, including pneumatic adjustable pillars
- PVC shell
- Insulation
- Water pipe and distribution system
- Air pipe and distribution system
- Air compressor
- Heating system for freeze protection (pipes and jets)
- Measuring components
- Control technology

Figures 3.1 to **3.4** show pictures of the on-site installed components, including water distribution, control technology and air compressor are shown.

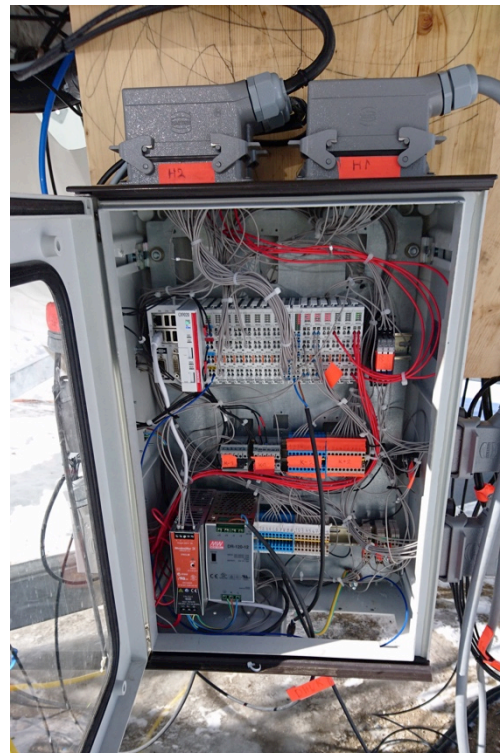**Figure 3.1**: Water distribution system

Figure 3.2: Control technology box

Figure 3.3: Air compressor

Figure 3.4: Air filtration

Construction and assembling took around 2 months, until a properly working process was obtained.
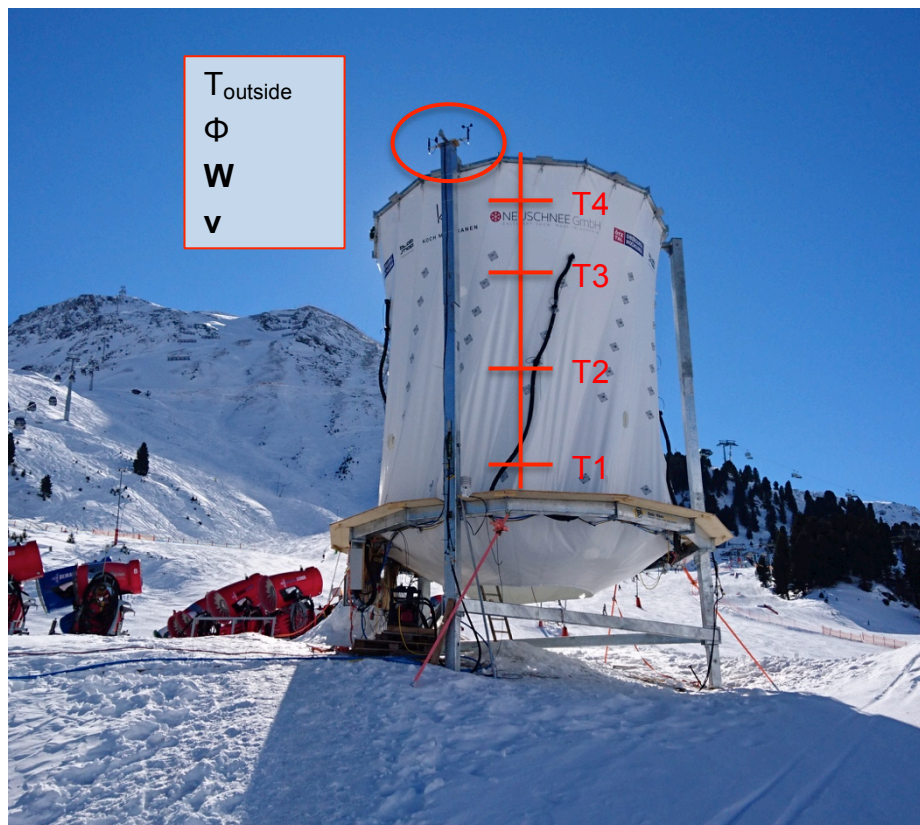

Figure 3.5: Cloud chamber in operation © Neuschnee GmbH

The research goal was, to get a better understanding for the process, its limits and properties under given conditions. Therefore, the following characteristics were measured:

  − Air temperature of the atmosphere ($T_{outside}$)
  − Air temperature inside the cloud chamber (T_1-T_4)
  − Radiation properties in the atmosphere (**W**)
  − Wind speed (**v**)

Measurement locations are shown in **Figure 3.5**. At the top of the pilot plant, a weather station is mounted. Outside conditions are read off that device. T_1-T_4 are located at the centre of the cloud chamber where a vertical temperature profile is measured. **Figure 3.6** and **Figure 3.7** show the characteristic behaviour of measured values during an experiment. For this trial, 2,8 l/min water were introduced to the cloud chamber. By measuring a snow density of 230 kg/m^3 , this equals a snow production rate of 0,73 m^3 snow per hour. The test started at 18:15, where an immediate rise of temperature in the cloud chamber was monitored. At around 18:50, stable conditions were observed. Temperatures T_1 to T_4 showed an even gradient of 4 K at the beginning and 5,5 K at the end of the experiment, compared to the outside temperature.
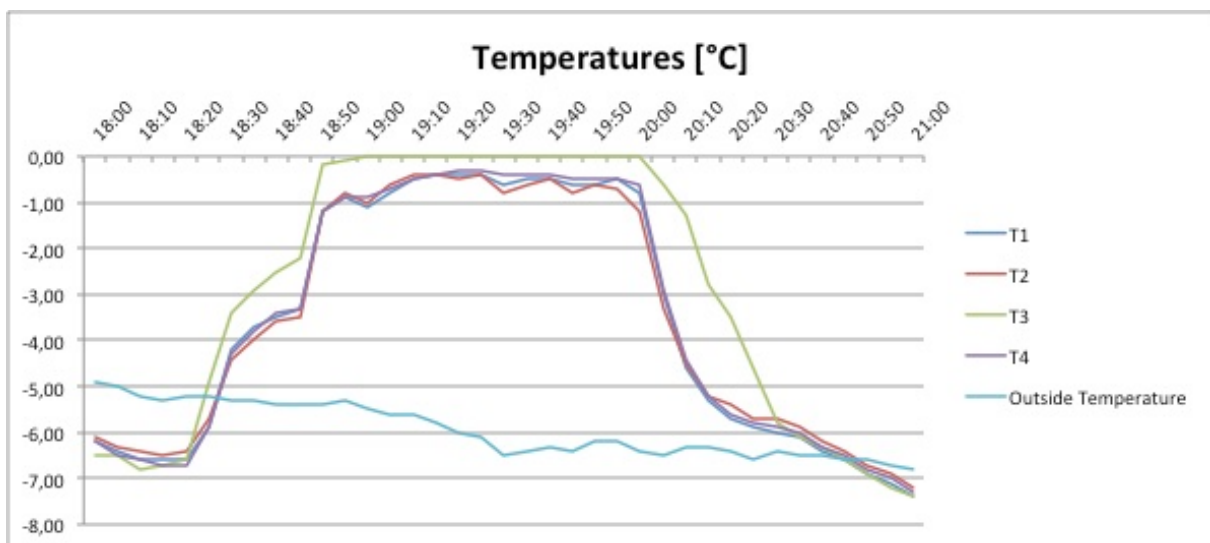

Figure 3.6: Temperature measurements Obergurgl 2016 © Neuschnee GmbH

Radiation measurements are representative for the ability of heat transfer into the atmosphere. Absolute values above 100 W/m^2 indicated clear skies, measured values between 30 and 70 W/m^2 were an indicator for cloudy conditions and therefore reduced heat removal abilities of the cloud chamber. During this experiment, values from 140 to 80 W/m^2 were measured, which is illustrated in **Figure 3.7 (left)**. The effect of radiation to the snow-making process reflects in the change of temperature difference from 4 K to 5,5 K, that develops during the

experiment. The presence of wind is assumed, to have a cooling effect on the process as well. This could, however, not be quantified yet. During the experiment, wind speeds of up to 7 m/s could be measured
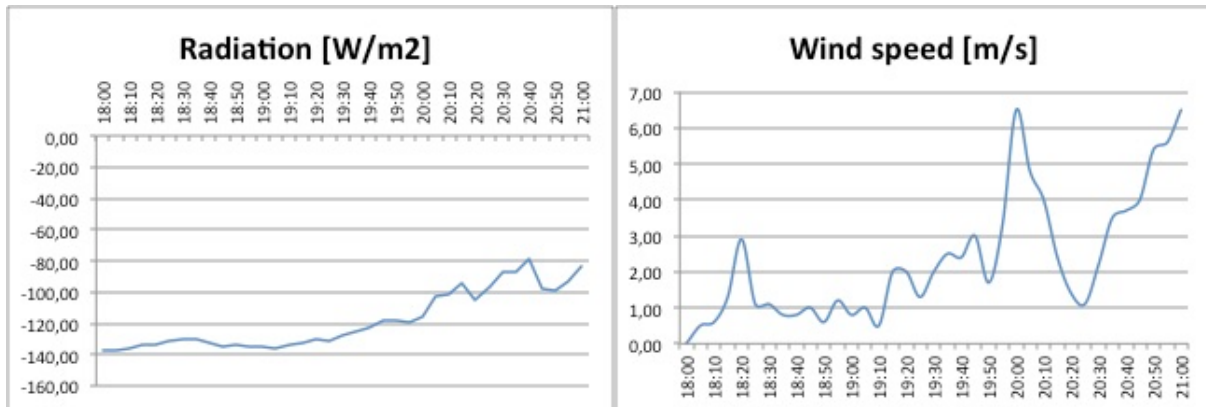

Figure 3.7: Radiation (left) & wind speed (right) measurements Obergurgl 2016 © Neuschnee GmbH

While the above-mentioned measurements helped understanding the process, quantification of crystal growth, flow velocity and flow patterns would be of high interest. Due to the difficulty of measurement processes and the availability of instruments, this could not be performed. Furthermore, the assumption, that a temperature gradient inside the cloud chamber would develop, could not be confirmed. The development of a numerical model followed the aim, to raise knowledge on the data and accelerate the further development of the system.

4 Numerical solution methods

Streams and similar phenomenon can be described by partial differential equations, which cannot be solved analytically in most cases. In the present case, the Navier-Stokes equations (NSE) for Newtonian compressible fluids represent the underlying system of equations that should be solved. This happens via numerical methods. Instead of solving the analytical problem, it is approximated by a system of algebraic equations. By the application of these methods to small areas in space and/or time, the numerical solution provides results in space and time. [48]

4.1 Mesh

A numerical grid defines discrete points, at which the variables are calculated. The grid is a discretized representation of a geometrical domain. It separates the solution domain into a finite number of subdomains. The generation of a good grid is the base of any numerical simulation.

In general, numerical grids can be divided into structured and unstructured grids. Structured grids consist of sets of gridlines with the property that the members of a set don't cross and only cross the members of another set once. This is the most simple grid structure and any point has exactly four neighbours. Structured grids consist of regular matrices, simplify programming and often lead to faster solutions of numerical models. On the other hand, structured grids are only applicable to relatively simple geometrical structures.

Complexity of the geometry very often augments with 3D geometries. For 3D geometries, unstructured grids are often more favourable. These grids, in the 3D case, consist of hexahedral or tetrahedral structures. Unstructured grids represent the most flexible grid type, so do the solver models, developed for unstructured grids. These are, among other methods, used with the Finite volume (FV) method. The FV method is also used by the ANSYS Fluent solver. [48]

4.2 Solvers

In order to get a better understanding of the processes in the cloud chamber, conservation laws for mass, momentum and energy should be solved. Therefore, the software ANSYS Fluent is used. The 3D Navier-Stokes equations represent the base for the simulations.

As these non-linear differential equations cannot be solved analytically, in most cases, they are solved numerically. Fluent offers two distinct numerical solvers:

- pressure-based solver
- density-based solver

Initially, the pressure-based approach was developed for low-speed incompressible flows, while the density-based approach was mainly used for high-speed compressible flows. Recently both methods have been developed and reformulated to solve and operate for a wide range of flow conditions beyond their original intent.

The density-based solver solves the governing equations of continuity, momentum, and (where appropriate) energy and species transport simultaneously. Governing equations for additional scalars will be solved afterward and sequentially.

The pressure-based solver employs an algorithm, which belongs to a general class of methods called the projection method [49]. In the projection method, wherein the constraint of mass conservation (continuity) of the velocity field, is achieved by solving a pressure (or pressure correction) equation. The pressure equation is derived from the continuity and the momentum equations in such a way that the velocity field, corrected by the pressure, satisfies the continuity.

Independent of the method, Fluent will solve the governing integral equations for the conservation of mass and momentum, energy and other scalars such as turbulence and chemical species [50].

Using the pressure-based approach, the pressure field is extracted by solving a pressure or pressure correction equation, which is obtained by manipulating continuity and momentum equations.

In both methods the velocity field is obtained from the momentum equations. In the density-based approach, the continuity equation is used to obtain the density field while the pressure field is determined from the equation of state.

Since the governing equations are nonlinear and coupled to one another, the solution process involves iterations wherein the entire set of governing equations is solved repeatedly until the solution converges [50]. **Figure 4.1** illustrates solution procedures of the solvers.
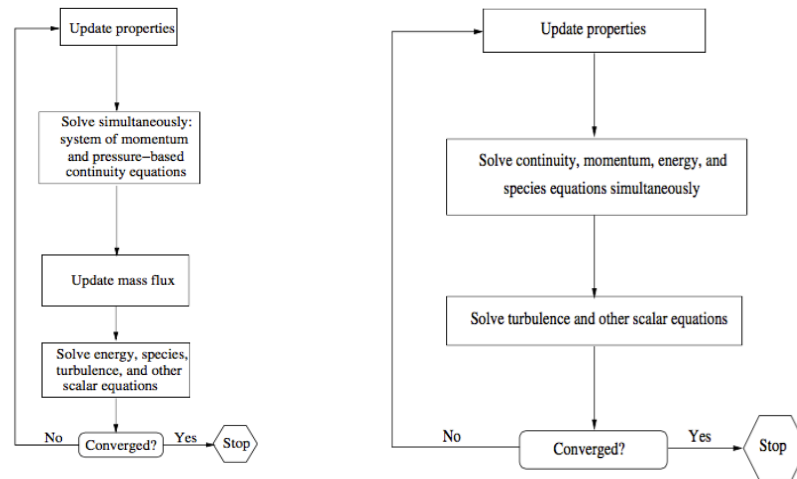
Figure 4.1: Coupled pressure-based (left) & density-based (right) solution methods [50]

4.3 Discretization methods

The Navier-Stokes equations are partial differential equations, which in most cases don't have an analytical solution. They are solved numerically by Fluent. In order to find a numerical approximate solution of the problem, a discretization method needs to be found. The differential equations are be approximated by a system of algebraic equations which can be solved by the software. The approximations are applied for small areas in space and/or time for which the numerical solution provides results at discrete points.

There are three different discretization methods, used for numerical simulations:

- Finite difference method
- Finite element method
- Finite volume method

In the field of flow simulations, the finite volume method is the most common one. It uses the integral form of the conservation law as a starting point. The solution domain is divided in a finite number of not overlapping control volumes and the conservation law is applied to every control volume. Calculation points are situated in the control volume's centres of mass. Afterwards, conservation laws are integrated approximately via squaring formulas. The transformation of volume integrals into surface integrals includes global conservativeness in the method, which is an advantage towards other discretization models. This method is also independent of coordinate systems and the applied grid [46].

4.4 Interpolation

Interpolation methods are necessary in order to determine convective fluxes at the cell surface by using cell centre saved, convective variables. The behaviour of interpolation methods varies in accuracy, stability and required calculation capacity. There are numerous types of interpolation methods. Some of the most common ones will be explained here.

4.4.1 Upwind interpolation

The approximation of φ_e by the value of φ in the control volume centre upstream of e is equivalent to the usage of a back- or forward approximation of the first derivative in Finite difference methods (depending on the flow direction), which is why this approximation is termed as upwind difference although it is not a difference, but an interpolation:

$$\varphi_e = \begin{cases} \varphi_P & if \ (v \cdot n)_e > 0; \\ \varphi_E & if \ (v \cdot n)_e < 0. \end{cases} \tag{4-1}$$
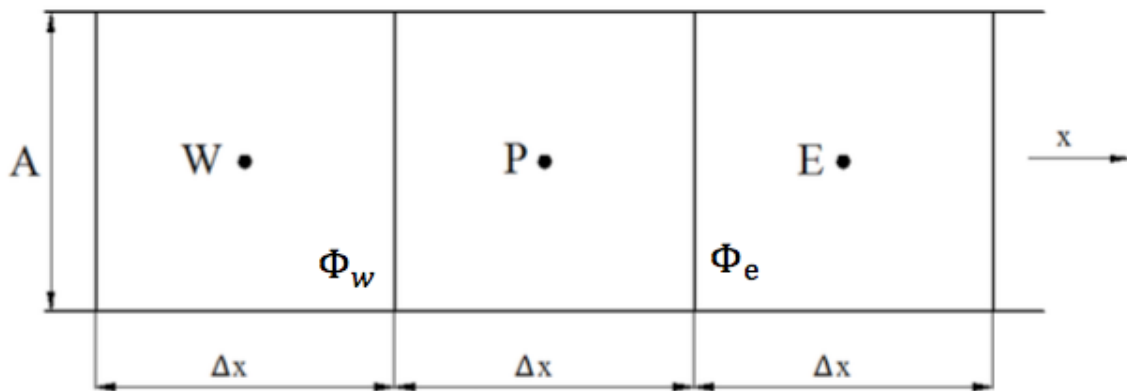
Figure 4.2: Schematic representation of the control volume [46]

This method, illustrated in **Figure 4.2**, represents the only approximation that unconditionally fulfils the requirements in boundedness because of first order accuracy. It does not give oscillating solutions but its leading stop error is of diffusive form. The diffusivity of the method causes smearing of spatial gradients. This effect can be overcome with a fine grid.

4.4.2 Linear interpolation

This method equals the central-difference approximation of the first derivative for the Finite difference method. It is the linear interpolation between the two adjacent calculation nodes. On a Cartesian grid, the following applies at the node e:

$$\varphi_e = \varphi_E \lambda_e + \varphi_P (1 - \lambda_e) \qquad\qquad (\,4\text{-}2)$$

,where the linear interpolation factor λ_E is defined as:

$$\lambda_e = \frac{x_e - x_P}{x_E - x_P} \quad . \qquad\qquad (\,4\text{-}3\,)$$

The method's accuracy is of 2nd order. It's leading stop error is proportional to the square grid distance, independent of whether grid is equidistant or not. Like all approximations of order greater than one, oscillating solutions can be produced. The linear interpolation is the simplest one and furthermore it is suitable with Large Eddy Simulations (LES). [48]

4.5 Modeling turbulence

4.5.1 Turbulent flow

In terms of turbulence, flows can be classified in laminar and turbulent. Most engineering problems deal with turbulent flows. The dimensionless index of whether a flow is laminar or turbulent is called Reynolds number (2-16).

Turbulent flows unfold velocity components orthogonal to the main flow direction that amplify impulse exchange. Vortex structures cause 3D velocity fluctuations and altering velocities around an average. Nevertheless mass conservation is given. These properties make it excessively harder to build models, which describe turbulent flows with reasonable calculation effort and sufficient accuracy.

4.5.2 Simulating turbulent flow

The most exact way of turbulence simulation is the solution of the Navier-Stokes equations without any approximation or averaging except numerical discretization where the error is assessable and controllable. This direct numerical simulation (DNS) dissolves every range of movement. Again, calculation capacities are the reason, why this is not possible or reasonable in most cases.

Two methods of avoiding the exact resolution of eddy structures have been developed. One method relies on Reynolds-averaging (RANS), the other one filters out small scale eddies (LES). To compensate these simplifications, additional terms are included in the Navier-Stokes equations. In the first case, turbulence fluctuations are modelled. In the second case, small scales are modelled.

The following list gives an overview of some common methods to solve turbulent flow:

- **Reynolds-averaged Navier-Stokes-equations**
  - k-ε models
    - o Standard k-ε model
    - o RNG k-ε model
    - o Realizable k-ε model

  - k-ω models
    - o Wilcox k-ω model
    - o k-ω-SST model
- **Large Eddy Simulation**

  - Smagoronsky-Lilly-Modell

  - One-Eq-Eddy-Modell

  - Deardorff Differential Stress Modell

- **Direct numerical simulation (DNS)**

4.5.3 Large eddy simulation (LES)

LES is based on the negligence of small scale eddies because of their little impact on energy conservation and transport. It requires a 3D, time dependent calculation, what still keeps it relatively resource demanding. It is a compromise, compared to DNS, suitable for problems with complex geometries or high Reynolds numbers. In order to find a velocity field that only contains large-scale components one method is to filter the velocity field. The outcome is a velocity field of local averages. The filtered velocity in one dimension is defined as

$$\overline{u_i}(x) = \int G(x, x')u_i(x') \, dx' \qquad (4\text{-}4)$$

where $G(x, x')$ is the filter core that represents a local function. Depending on the application, these filter cores can have different forms [48].

4.5.4 Reynolds-averaged Navier-Stokes equations

RANS turbulence models can rather be seen as qualitative approximations for engineering applications than application of physical laws. As mentioned before, a high frequency of transient processes happens in turbulent flows. Applying Reynolds-averaged methods on turbulent flows, the entire fluctuation in time is seen as turbulence and therefore averaged. The non-linearity of the Navier-Stokes equations leads to terms that need to be modelled as well.
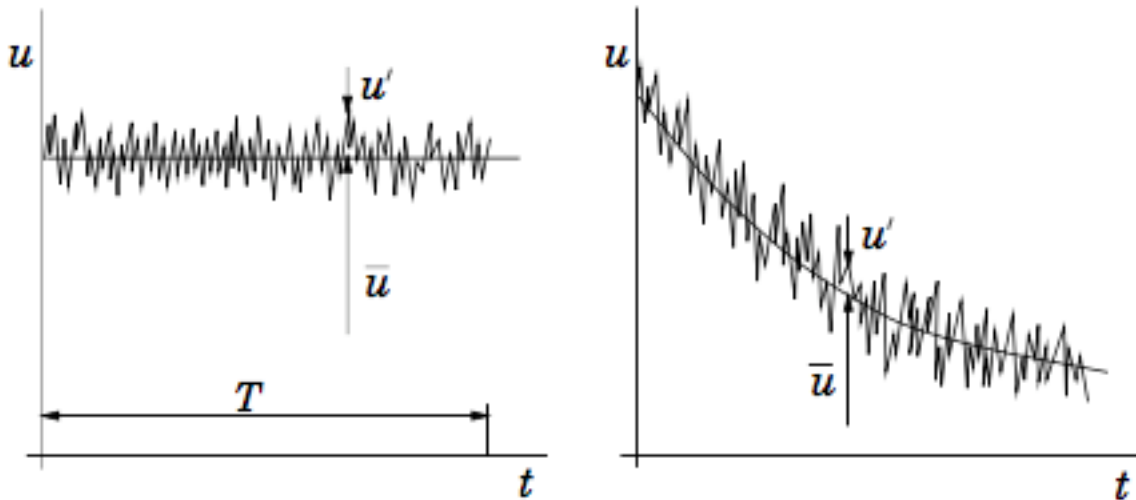
Figure 4.3: RANS illustration [50]

The basic form of Reynolds-averaging is the statistically stationary case. Any variable can be represented as a time average and a fluctuation around this value:

$$\phi(x_i, t) = \bar{\phi}(x_i, t) + \phi'(x_i, t).$$
(4-5)

Applying this procedure to the Navier-Stokes equations results in a new system of equations, the Reynolds-averaged Navier-Stokes equations [50]. Furthermore, additional terms are created due to the approximation process.

These so-called Reynolds-stresses can be written in matrix format:

$$\boldsymbol{\tau}_{turb} = -\rho \begin{pmatrix} \overline{u'u'} & \overline{u'v'} & \overline{u'w'} \\ \overline{v'u'} & \overline{v'v'} & \overline{v'w'} \\ \overline{w'u'} & \overline{w'v'} & \overline{w'w'} \end{pmatrix}$$
(4-6)

Due to the symmetry of the stress tensor six new variables remain. So four conservation laws face for the averaged values face ten unknown variables. The system of equations is therefore not closed. This is called the closure problem of turbulence. In order to solve this particular problem, turbulence models are applied [50].

As in this work RANS simulations will be applied, two model types will be described further.

4.5.5 RNG k-ε model

Two-equation turbulence models allow the determination of both, a turbulent length and time scale by solving two separate transport equations. Robustness, economy and reasonable accuracy for a wide range of turbulent flows explain their popularity in industrial flow simulations [50].

The RNG k-ε model is a further development of the standard k-ε model. It was derived using a statistical technique called renormalization group theory. Additional terms in its ε-equation improve accuracy for rapid strained flows, the effect of swirl in turbulence enhance accuracy for swirling flows and an analytically derived differential formula for effective viscosity accounts for low-Reynolds number effects.

Governing equations for k and ε are represented below:

$$\frac{\partial}{\partial t}(\rho k) + \frac{\partial}{\partial x_i}(\rho k u_i) = \frac{\partial}{\partial x_j}\left(\alpha_k \mu_{eff}\frac{\partial k}{\partial x_j}\right) + G_k + G_h - \rho\varepsilon - Y_M + S_k \qquad (4\text{-}7)$$

$$\frac{\partial}{\partial t}(\rho\varepsilon) + \frac{\partial}{\partial x_i}(\rho\varepsilon u_i) = \frac{\partial}{\partial x_j}\left(\alpha_\varepsilon \mu_{eff}\frac{\partial\varepsilon}{\partial x_j}\right) + C_{1\varepsilon}\frac{\varepsilon}{k}(G_k + G_{3\varepsilon}G_h) - C_{2\varepsilon}\rho\frac{\varepsilon^2}{k} - R_\varepsilon + S_\varepsilon \qquad (4\text{-}8)$$

G_k represents the generation of turbulence kinetic energy due to the mean velocity gradients, G_h is the generation of turbulence kinetic energy due to buoyancy, Y_M represents the contribution of the fluctuating dilatation in compressible turbulence to the overall dissipation rate and the variables α_k and α_ε are the inverse Prandtl numbers for k and ε [50].

4.5.6 k-ω SST model

The shear-stress transport k-ω model was developed to effectively combine the free stream independence of the k-ε model in the far field and the near-wall accuracy of the k-ω model. Both models are multiplied by a blending function, which enables the application of different models in different zones. The k-ω SST model is stable and able to give accurate solutions for complex flows. [50]

It's governing equations have the following form [50]:

$$\frac{\partial}{\partial t}(\rho k) + \frac{\partial}{\partial x_i}(\rho k u_i) = \frac{\partial}{\partial x_j}\left(\Pi_k\frac{\partial k}{\partial x_j}\right) + G_k + -X_k + S_k \qquad (4\text{-}9)$$

$$\frac{\partial}{\partial t}(\rho\omega) + \frac{\partial}{\partial x_j}(\rho\omega u_j) = \frac{\partial}{\partial x_j}\left(\Pi_\omega\frac{\partial\omega}{\partial x_j}\right) + G_\omega + -X_\omega + E_\omega + S_\omega \qquad (4\text{-}10)$$

4.6 Near-wall treatment

The treatment of near-wall regions is a topic that has to be taken in account, especially for turbulent air flow problems. Fluent's User Guide gives the following explanation [50]:

"Turbulent flows are significantly affected by the presence of walls. Obviously, the mean velocity field is affected through the no-slip condition that has to be satisfied at the wall. "

"Numerous experiments have shown that the near-wall region can be largely subdivided into three layers. In the innermost layer, called the viscous sublayer, the flow is almost laminar, and the (molecular) viscosity plays a dominant role in momentum and heat or mass transfer. In the outer layer, called the fully-turbulent layer, turbulence plays a major role. Finally, there is an interim region between the viscous sublayer and the fully turbulent layer where the effects of molecular viscosity and turbulence are equally important." [50] **Figure 4.4** illustrates this three-layer-model:
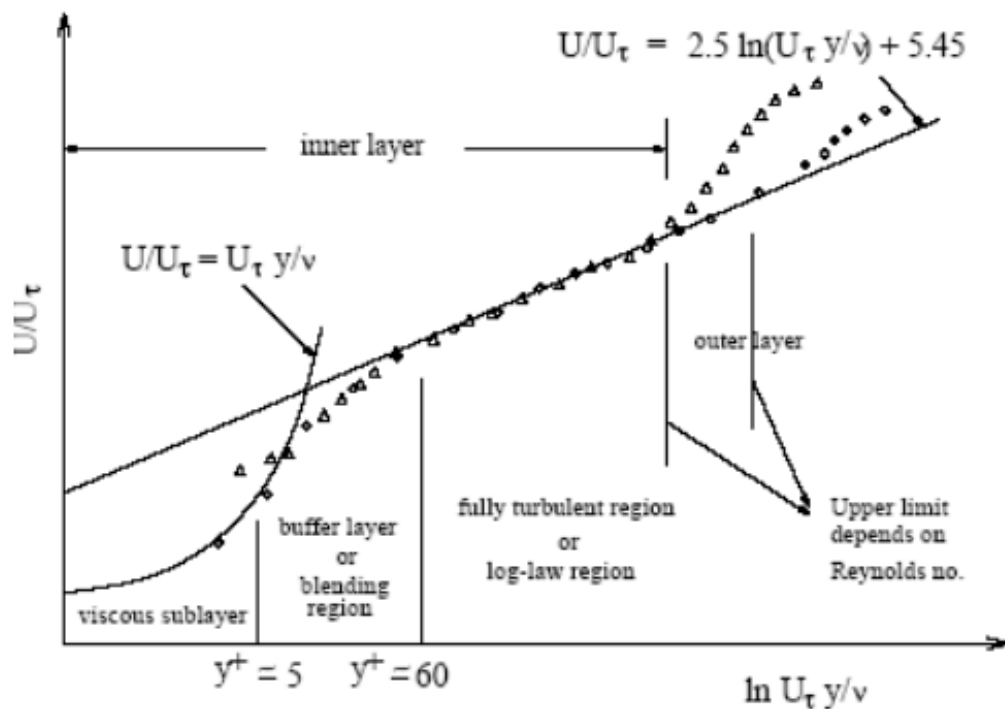
Figure 4.4: Three-layer model [50]

Traditionally, there are two approaches to modeling the near-wall region. Using one approach, the viscosity-affected inner region (viscous sublayer and buffer layer) is not resolved. Instead, semi-empirical formulas called wall functions are used to bridge the viscosity-affected region between the wall and the fully turbulent region. The use of wall functions obviates the need to modify the turbulence models to account for the presence of the wall.

In another approach, the turbulence models are modified to enable the viscosity-affected region to be resolved with a mesh all the way to the wall, including the viscous sublayer.

Cell sizes vary significantly with the application of different wall approaches. As for the wall function, a high resolution in the wall region is not required and cells are larger in general, the cells for the near-wall-model are significantly smaller, because of the high resolution near the wall. The two approaches are illustrated in **Figure 4.5**.
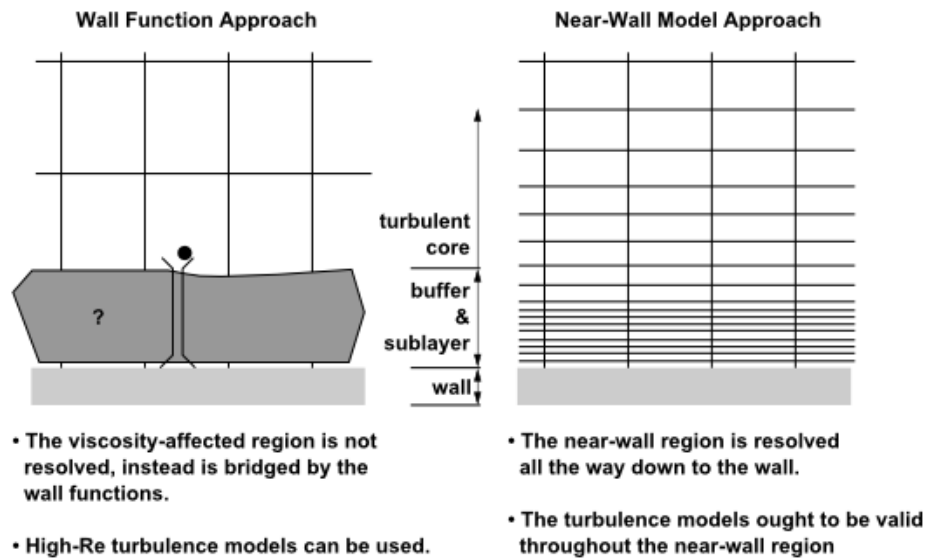
Figure 4.5: Wall Function Approach and Near-Wall-Model Approach [50]

5 Realization of the CFD Model

The aim is to develop a numerical model in which processes, happening inside the snow machine, are simulated. To receive this, several cases were built up. They will be discussed and compared in this chapter. However, some of the conditions stayed the same for all the cases. In the following part a general idea of the model approach should be given at first. Generally applied conditions will be discussed and furthermore three executed cases will be described. For the performed simulations, the software version Fluent 17.1 was used. The applied license is owned by the European research institute CERN in Geneva.

5.1 Inlet boundary condition

Air is entering the cloud chamber through nozzles. The technology is described briefly in 2.1.3 **"Nozzle technology".** As there is little manufacturer data available on the applied jets and simulation or measurement results are not given to product customers right away, a lot of information on jet properties is missing. Therefore, measurements of the airflow properties at the nozzle exit were executed for desired operation points. Declared aim of those measurements was to find out, whether flow can be treated as compressible or incompressible. This fact can be determined by relating it to the phenomenon of choked flow, which was discussed in 2.2.3. "Compressible fluid flow".

In **Figure 5.1**, airflow and absolute pressure are illustrated in relation. An estimated pressure drop of $\Delta p = 1{,}8$ bar correlation to values at sonic condition, calculated by choked flow theory. Operating conditions are in between 2 bar and 4 bar air pressure. Those values are above critical pressure values for choked flow, which leads to the conclusion sonic velocities including sonic booms, occur at the jet outlets. Based on this knowledge, CFD inlets were designed. Further information on massflow calculations can be found in Appendix B.
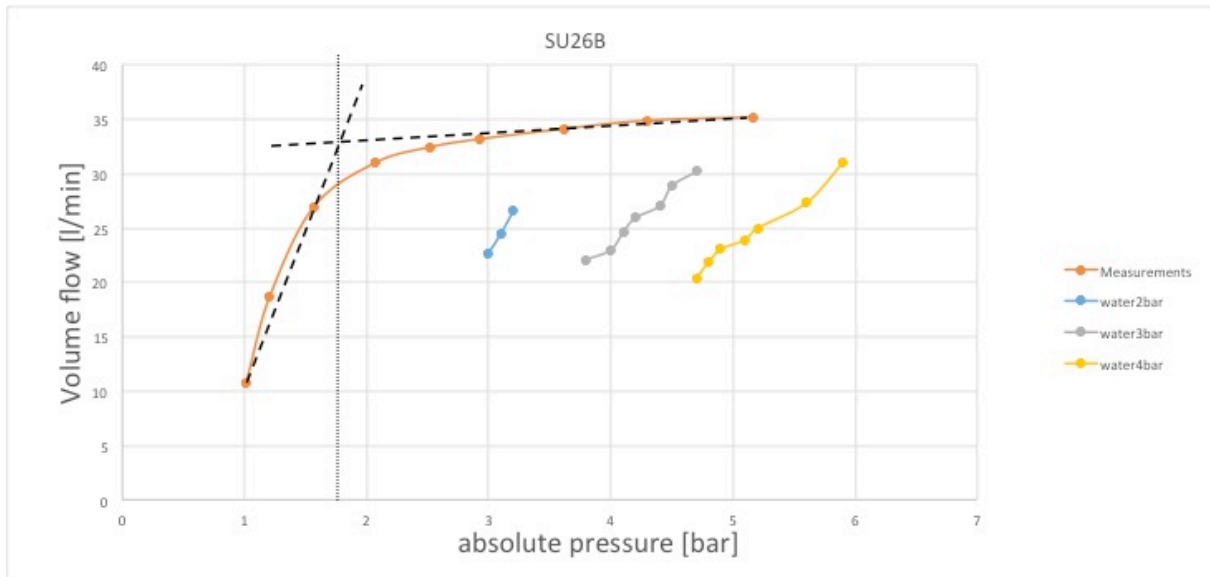
Figure 5.1: Choked flow measurements SU26B

Figure 5.2 illustrates the velocity vector profile, which was used to embed the nozzle's spray jets. The inlet was realized as a mass-flow inlet. Due to size and complexity of the model, importance was attached to the simpleness of the inlet boundary and therefore a profile file was used to give inputs of massflow and direction at the inlets instead of representing the entire nozzle geometry in the mesh.
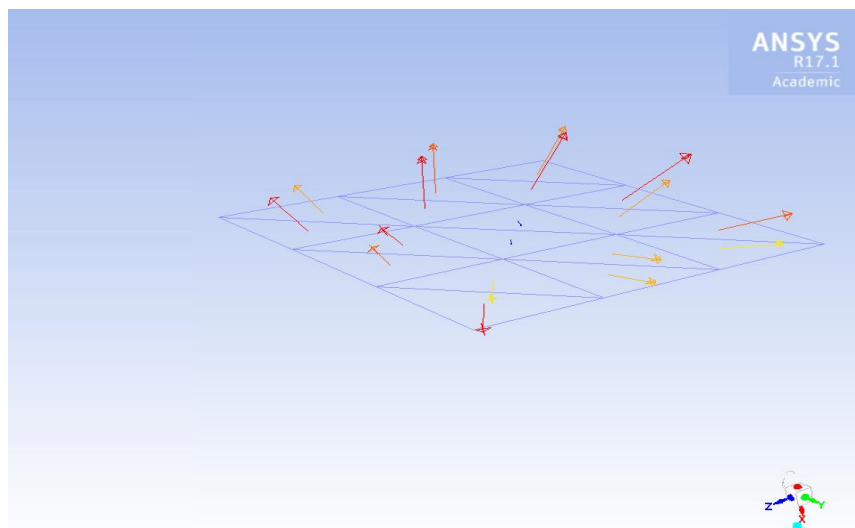

Figure 5.2: Velocity vector profile coloured by Mach number

Each of the inlets consists of 18 cells. **Figure 5.3** presents the contour plot of Mach numbers from the cells of one of the inlets. Number and structure of cells are the same for all inlets.
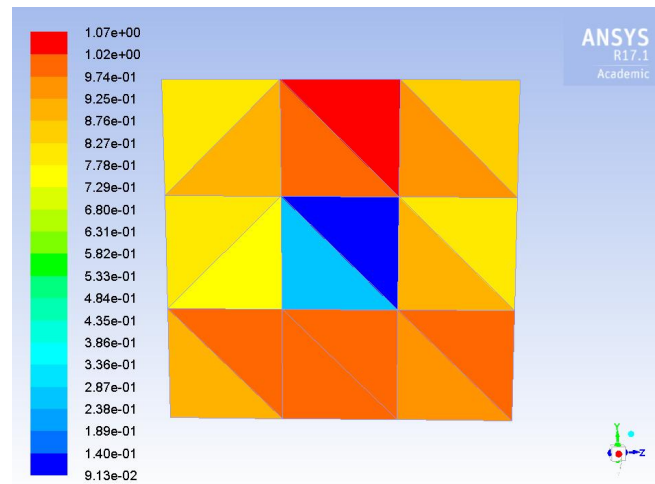
Figure 5.3: Mach number @ inlet2

Table 5.1 representatively shows calculated values of Mach numbers, absolute pressure and cell size at inlet 2. Cell numbers are sorted ascending from left to right, top to bottom. The model has three inlets in total (see **Figure 5.4**), through those air enters the domain.

Table 5.1: Values calculated by Fluent @ inlet2

Cell #	Mach number [1]	Absolute pressure [Pa]	Cell face area [mm^2]
1	0,916	102 640	1,140
2	0,970	89 132	1,154
3	0,976	92 892	1,149
4	0,992	82 677	1,150
5	0,994	81 548	1,153
6	1,015	81 861	1,141
7	0,767	61 505	1,147
8	0,272	49 461	1,139
9	0,797	81 243	1,147
10	0,893	62 533	1,150
11	0,091	55 902	1,148
12	1,013	78 995	1,149
13	0,792	84 044	1,140
14	0,955	67 092	1,151
15	0,855	92 905	1,150
16	1,072	85 173	1,149
17	0,883	74 069	1,141
18	0,807	90 276	1,141

Mach-numbers were aimed to reach values in the region of Ma = 1. Due to the influence of the airflow passing the inlet, mass-flow values had to be adjusted in iterative steps, whereas the mutual influence between the cells made impossible to reach the exact values.

The inlets of the domain consist of nine equally divided square faces. Eight of them are used as massflow faces and the one in the middle is supposed to represent a velocity-less area. So the overall surface area of the eight squares should equal the nozzle exit area as close as possible. All of the nine squares are divided in the middle due to the structure of the mesh. The relevant inlet area of the mesh measures 20,64 mm^2, while the real exit area of the nozzle measures 18,84 mm^2. This corresponds to a deviation of 8,72%. In regard to the enormous mesh domain, this value is small.

5.2 Periodic boundary condition

When developing a numerical model, limits of computational resources are a considerable topic. In terms of grid creation, one is aiming to represent the case with as little cells as possible. In general, a close look on the possibility of representing the problem in 2D is taken at first. This could not be achieved because the process is not representable in 2D. I would consider the problem as highly three-dimensional. Another approach is the consideration of only a subfield of the entire geometry. The control volume can be divided into 12 similar parts around the vertical axis. **Figure 5.4** shows the twelfth part of the main cloud chamber, which is rotationally symmetric around the periodic axis **(4)**. Among other criterions, this symmetry allows the creation of a cyclic periodic model. More precisely, this is possible, when "the physical geometry of interest and the expected pattern of the flow/thermal solution have a periodically repeating nature." [46] For fluid flow problems that means, if "the flow entering the computational model through one periodic plane is identical to the flow exiting the domain through the opposite periodic plane". [46]
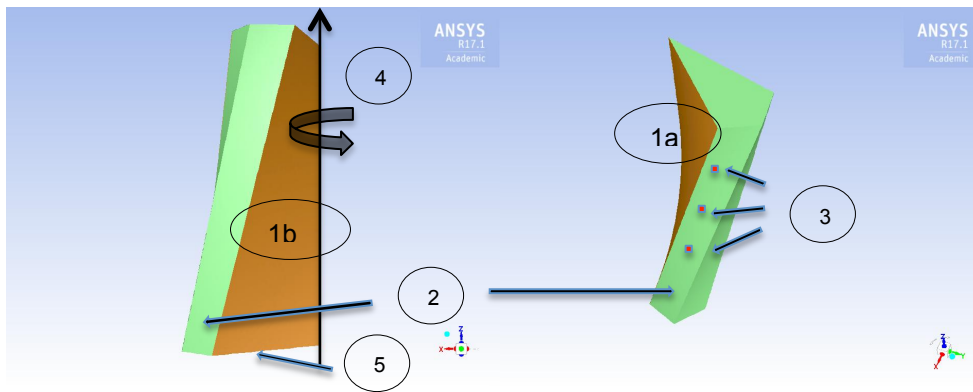
Figure 5.4: Boundaries of the numerical grid

In **Figure 5.4**, this condition is illustrated for the present model. The inlets 1-3 **(3)** are presented disproportionally big, as they are tiny in the proper model. The airflow is entering the domain through the inlets tangentially with respect to the cylindrical model. The flow, exiting the domain at one periodic boundary **(1b)** is entering that domain at the other periodic boundary **(1a)**. Through these twelve sets of inlets a swirling flow should be created. A precondition of the flow equality at the periodic boundaries is that the mesh at the periodic faces 1a and 1b is identical. The outlet, treated as pressure outlet condition, happens to be at the bottom of the domain **(5).** Wall boundaries **(2)** are represented in green.

5.3 Test cases

In advance it should be mentioned, that the executed cases were developed consecutively with gaining knowledge on the case and its difficulties. Three cases that are distinctive in shape, solvers, boundary conditions, near-wall treatment and turbulence modelling, will be discussed.
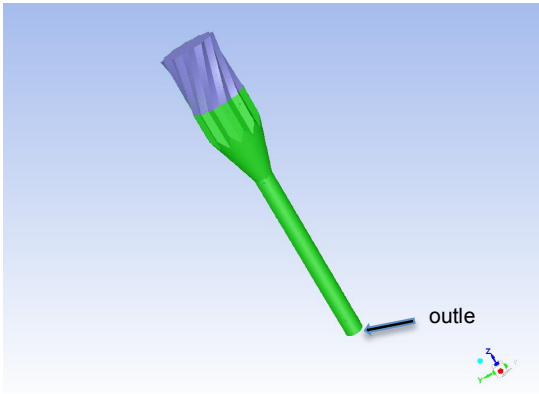
Table 5.2: Case characteristics

Case	Topic	Solver	Near-wall treatment
Case I	comparison of two outflow variations	Density-based	Enhanced wall treatment
Case II	comparison of four different turbulence models	Density-based	Scalable Wall-functions
Case III	comparison of two different solver models	Density-based/Pressure-based	Scalable Wall-functions

5.3.1 Case I

The aim of this first case was to create a fine resolution representation of the problem. This should be achieved by a highly resolved grid, in particular in near-wall regions and the consideration of compressibility effects in the entire domain. As conditions at the outlet happened to be unfavourable for steady outflow of the domain, two grid variations were tested to solve this problem.

Outlet Type	Conic outlet	Outlet Type	Cylindrical outlet
Grid type	unstructured	Grid type	unstructured
Cell type	Tetrahedrons	Cell type	Tetrahedrons
Number of cells	385 667	Number of cells	393 162
Max skewness	0,99	Max skewness	0,99
Min Orth Quality	$2,6*10^{-10}$	Min Orth Quality	$1,7*10^{-9}$
Max Aspect Ratio	$3,12*10^{3}$	Max Aspect Ratio	$8,6*10^{3}$
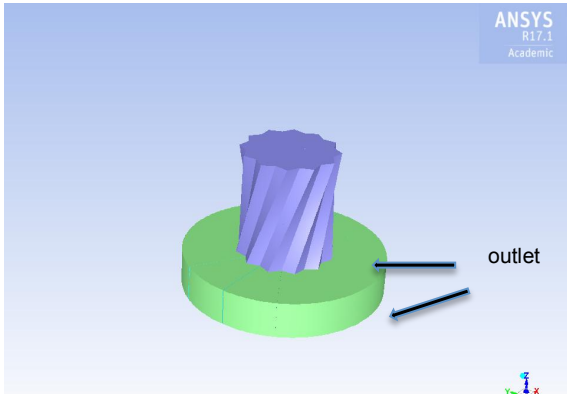
Figure 5.5: Grid properties Case I conic model (left) and cylindrical model (right)

5.3.1.1 Geometrical boundary conditions

Key data relating the applied grids is shown above. The core area of the model (coloured in violet) is the same for both models. On the left side, an extension, straight at first, then narrowing in order to bundle and accelerate the flow, is shown. Green surfaces represent walls. Its outlet is situated at the bottom. The right hand side shows a cylinder, attached to the core area. In this picture, all existing outlets are represented by green surfaces. The main difference to the left model is that the flow is restricted by an additional boundary condition at the bottom. While it flows out of the domain vertically in the conic domain, it is bounded in the vertical direction at

the model at the right side. The aim of this approach is the radial outflow of the domain, which is similar to practical operating conditions (see Chapter 3).

5.3.1.2 Solver, models, solution methods

These cases were solved parallel, using 6 cores. Steady, density-based solver was used, also solving the energy equation. Airflow was considered here only. It was treated as an ideal gas. So for the calculation of its density, the ideal gas law was used. For turbulence modelling, the standard k-ε model was used and explicit first order upwind discretization was applied.

5.3.1.3 Near-wall treatment

As it was the aim to produce a high resolution model here, Enhanced Wall Treatment serves this requirement as the equations are solved all the way to the walls. This demands a very fine grid at the wall boundary. This fine grid resolution can be achieved by applying a boundary layer.
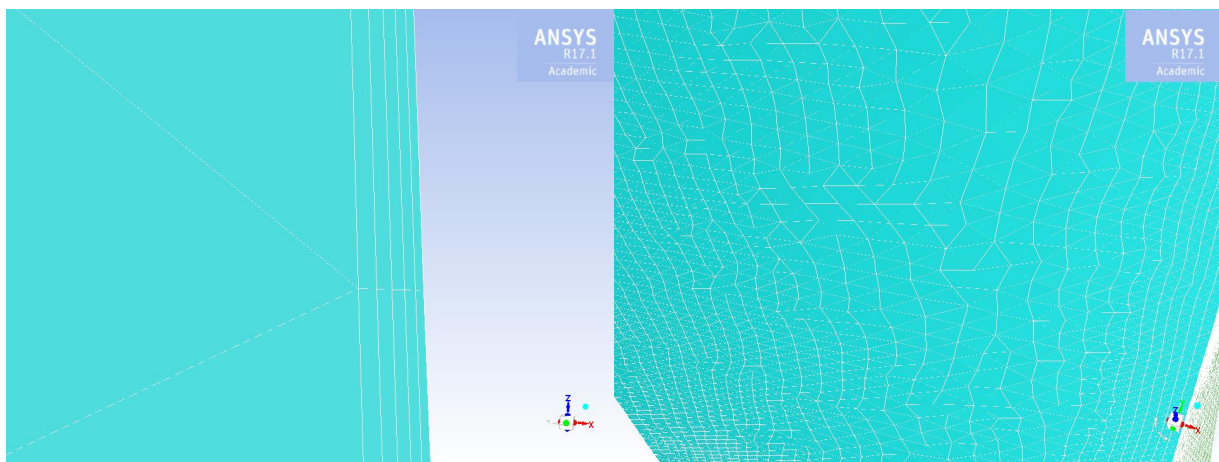
Figure 5.6: Near-wall grid of the two compared models

Figure 5.6 illustrates the dimension of the resolution. On the right side, the tetrahedral surface mesh of the periodic boundary is shown. The left side shows the boundary layer, where the its horizontal stretching is only a fraction of the tetrahedral piece next to it.

5.3.2 Case II

Motivation of the second approach was the comparison of several turbulence models. While using a coarser, numerically more favourable grid, the formation of turbulence was tested on its sensibility on different turbulence models.

5.3.2.1 Grid

Grid type	Unstructured
Cell type	Tetrahedrons
Number of cells	314 985
Max skewness	0,75
Min Orth Quality	0,24
Max Aspect Ratio	17,59
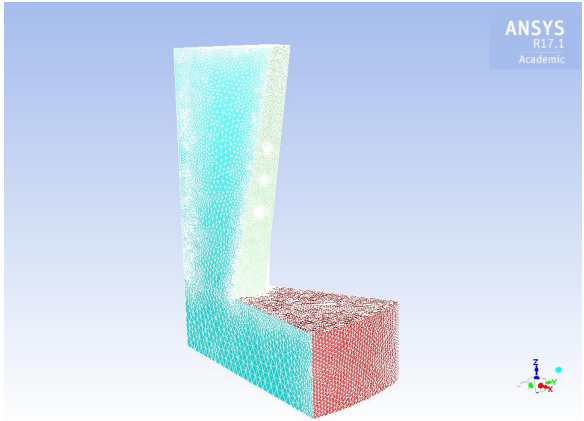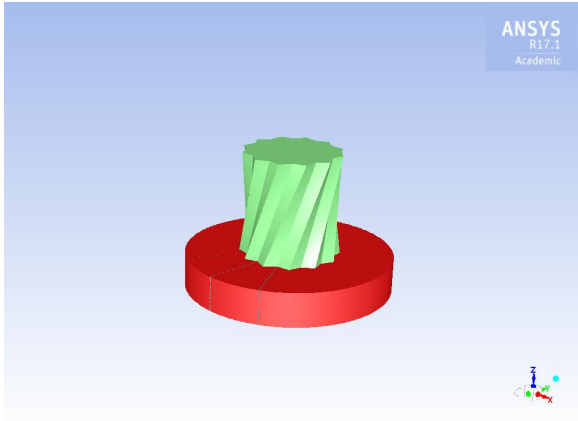
Figure 5.7: Grid properties Case II

5.3.2.2 Solver, models, solution methods

Conditions for this case remained the same as described in **5.3.1.2**, except for turbulence modelling.

5.3.2.3 Turbulence modelling

Outcomes of simulations using different turbulence models had to be compared due to the lack of literature for flow simulations similar to this one. While in many cases, models based on the Boussinesq approximation perform very well, RSM models are superior for flows in which the anisotropy of the flow plays a large role, which is the case in highly swirling flows. To prevent the high computational effort, which follows RSM models, a solution, using a Boussinesq model is favourable. [33] While Fluent offers the k-ε RNG for swirl dominated flows, no certainty on the consideration of

rotational forces on our model is given. A comparison on flow patterns and convergence characteristics was performed for the following turbulence models:

- Standard k-ε
- Realizable k-ε
- RNG k-ε
- k-ω SST

5.3.2.4 Near-wall treatment

Near-wall regions were treated with Scalable Wall Function (SWF). Losses in precision of the near wall solution of the NSE themselves can bring an advantage on mesh structure quality.

As the faces of the treated geometry are twisted against themselves, it is hard to achieve a low skewness level for the grid. The extra refinement at the wall boundaries, necessary for Enhanced Wall Treatment (EWT), makes it even harder to preserve a grid of low skewness. High velocity spectrums next to the walls require boundary layers of different sizes. Using the Enhanced Wall Treatment-model , achieving accurate Y^+ values is a factor of uncertainty in terms of grid quality. Scalable Wall Function should therefore augment the stability of the model while presenting good solutions in near-wall regions.

5.3.3 Case III

The third case, discussed in this thesis, differs from the others as another solver is used to calculate the compressible fluid flow case. Convergence behaviour of this solver should be monitored and results will be compared to the other cases.

5.3.3.1 Grid

Grid type	Unstructured
Cell type	Tetrahedrons/Hexahedrons
Number of cells	218 549
Max skewness	0,89
Min Orth Quality	0,10
Max Aspect Ratio	36,46
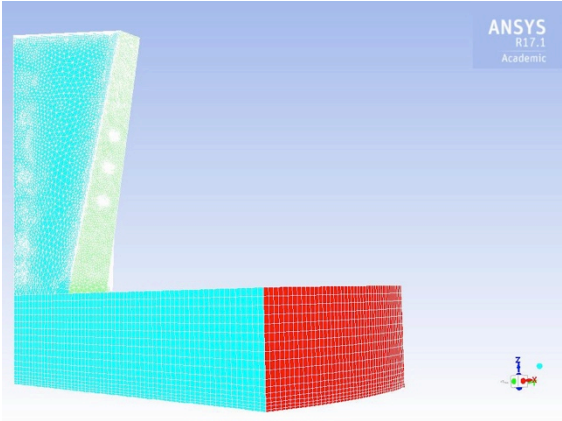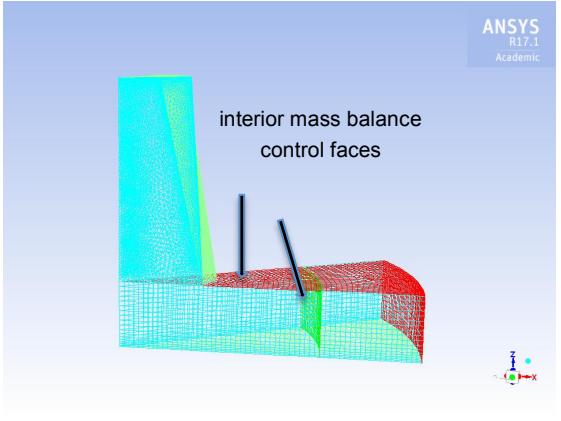
Figure 5.8: Grid properties Case III

Key data of the used grid is listed in **Figure 5.8**. What is noticeable is the hexagonal mesh structure of the cylinder slice at the bottom of the grid. Furthermore, an internal surface is presented in the right picture. This radially enlarged face serves to achieve more information on the convergence of the model. It presents a control face at which mass flow fluctuations are monitored and compared to values, charted at the outlets.

5.3.3.2 Solver, models, solution methods

Unlike the two former cases, this model was set up, using the steady pressure-based solver. Again, to account for compressibility effects in the domain, air was treated as an ideal gas and coming with that, the energy equation was solved as well. For

pressure-velocity coupling, the coupled-scheme was used. The Least squares cell based-scheme was used for gradient discretization and except for turbulent kinetic energy and dissipation rate, second order upwind schemes were used. Turbulence was considered via the Realizable k-ε model, as it gave the steadiest solution within the other trials.

5.3.3.3 Near-wall treatment

Again, Scalable Wall-Functions were used for the calculations in near-wall regions.

6 Analysis of the results

In the following, the performed cases will be represented and compared. In order to being able to compare them, dimensioned and dimensionless parameters of interest will be analysed. In **Figure 5.4** the model boundaries are described. In addition to those, internal faces are used to judge the cases. Before starting to compare parameters of interest for the three cases, I would like to name locations of control surfaces in the domain, as they will be used for representation in all models.
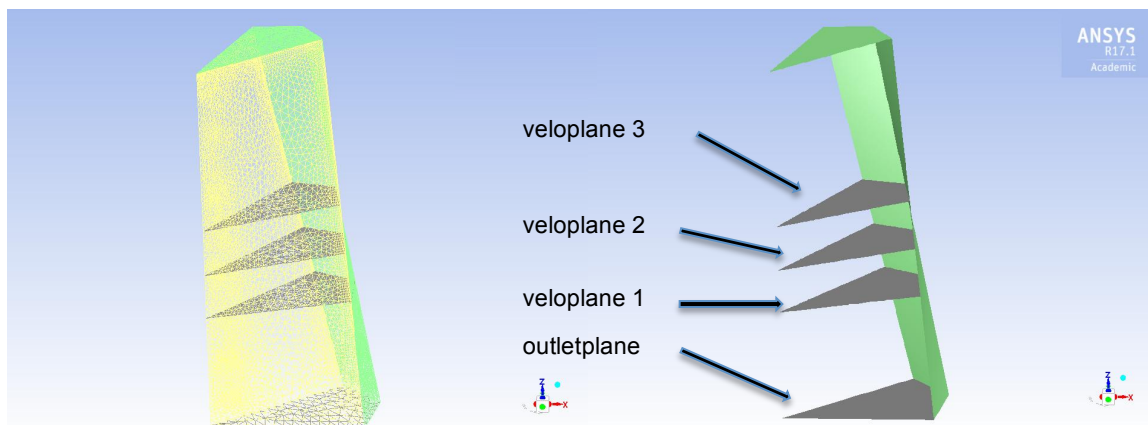
Figure 6.1: Internal faces for data evaluation and plotting

Figure 6.1 shows the horizontal planes veloplane 1, 2 and 3. They are located at z= 2 m, z=2,75 m and z =3,5 m. These locations were chosen due to the presence of the inlets at those heights and therefore the significance of plots at those locations. The face outletplane represents computing domain's counterpart to the lower ending of the cloud chamber.

6.1 Case I – comparison of geometrical boundaries

6.1.1 Convergence

One prerequisite of the comparison of a simulation is the presence of a converged solution. While there is the concept of residuals, which gives an idea of the numerical state of the solution, it doesn't necessarily judge convergence in all physical aspects. Therefore, mass imbalance, turbulence and velocity values were also monitored over time at relevant regions. **Figure 6.2** shows monitor values of the conic model, and their development during 10 000 iterations.
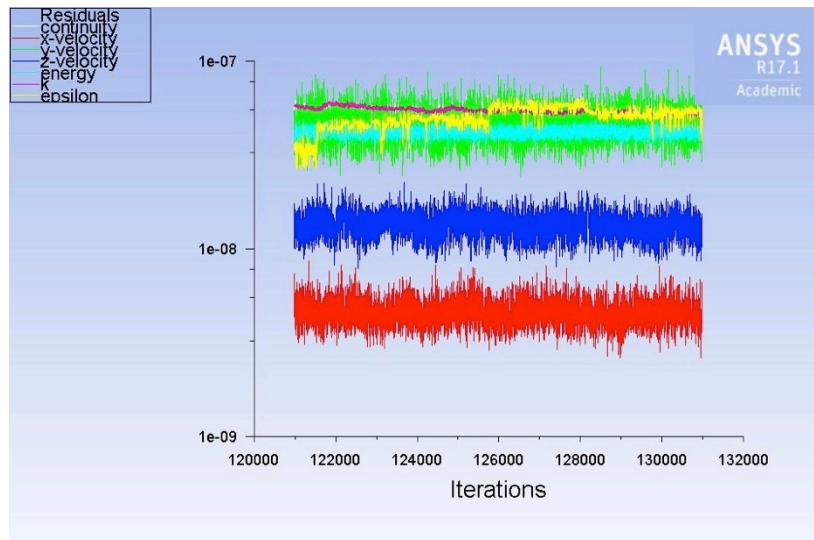
Figure 6.2: Convergence plot conic case

Residuals of this simulation are at a magnitude of 10^{-7} to 10^{-9}. As residuals are required to fall below a magnitude of 10^{-6} for the energy's residual and 10^{-3} for all other residuals in order to consider the solution as converged, observed values look pretty satisfying after 131 000 iterations.
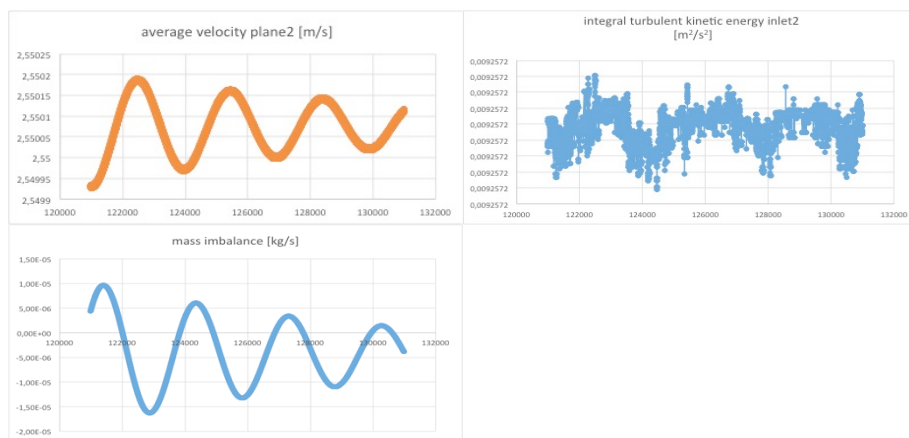
Figure 6.3: Monitor plots conic case

Figure 6.3 is representative for monitored values aiming to control on convergence. The upper left graph illustrates the mass-averaged velocity at the veloplane2 plane, the upper right graph shows the integrated kinetic turbulence energy at inlet 2 and the lower left graph illustrates mass imbalance between all inlets and outlets. Values in the first two graphs vary in the fifth significant place, which corresponds to a variation, smaller than 0,01 % of the absolute value. The smallest mass inlet value is at $1{,}2*10^{-3}$. The variation of the mass imbalance lies in a region smaller than 1 % of that value. Monitored values at the other control planes are presented in Appendix C.

In analogy to the convergence criteria, presented above, **Figure 6.5** and **Figure 6.6** show residuals and monitored values for the cylindrical outlet model.
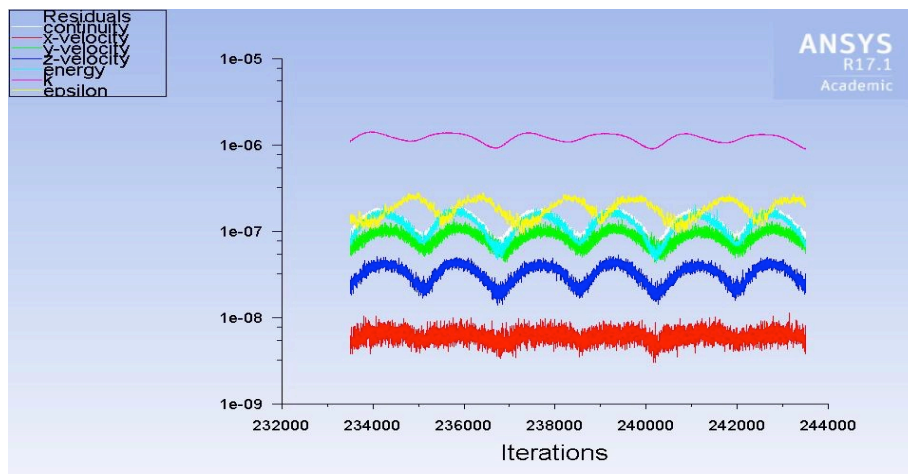
Figure 6.4: Convergence plot cylindrical case

This case was run for 244 thousand iterations. Residual values are lying in a range between 10^{-6} to 10^{-9}. Still, residual values alternate continuously with period durations of almost 2 000 iterations. This phenomenon can also be observed with the monitors of mass imbalance, turbulence and velocity, where flow velocity varies in a range of 3 % of its absolute value. Integral turbulence is more stable. Monitoring shows variations of 0,0012 % at maximum. Monitoring mass imbalance shows variation in between 0,03 and -0,02 kg/s. The overall inlet mass flow accounts for 0,0098 kg/s.

Monitored residuals, turbulence and velocity values show numbers in acceptable ranges. Fluctuations of those values although indicate a constant change of the solution. This altering solution does not allow a constant mass imbalance in an acceptable range. In order not to waive this result, velocity, and turbulence fields, five solutions in the range of the period length were compared. What could be found is a marginal change in all checked values. (See Appendix C) So the solution was compared with the conic outlet case.
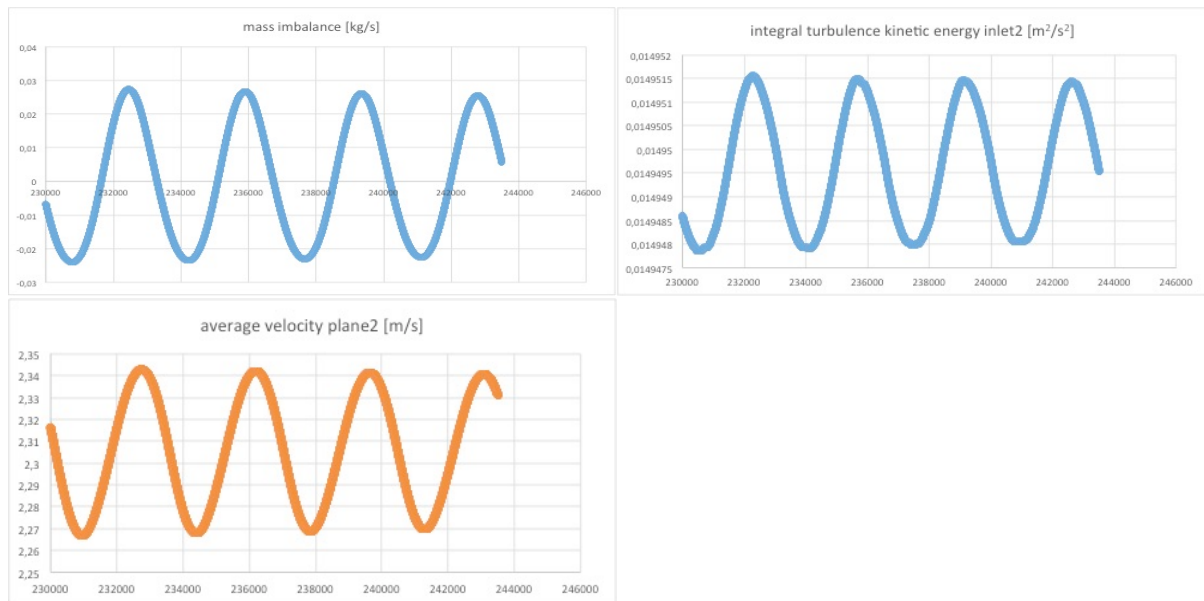
Figure 6.5: Monitor plots cylindrical case

6.1.2 Flow field
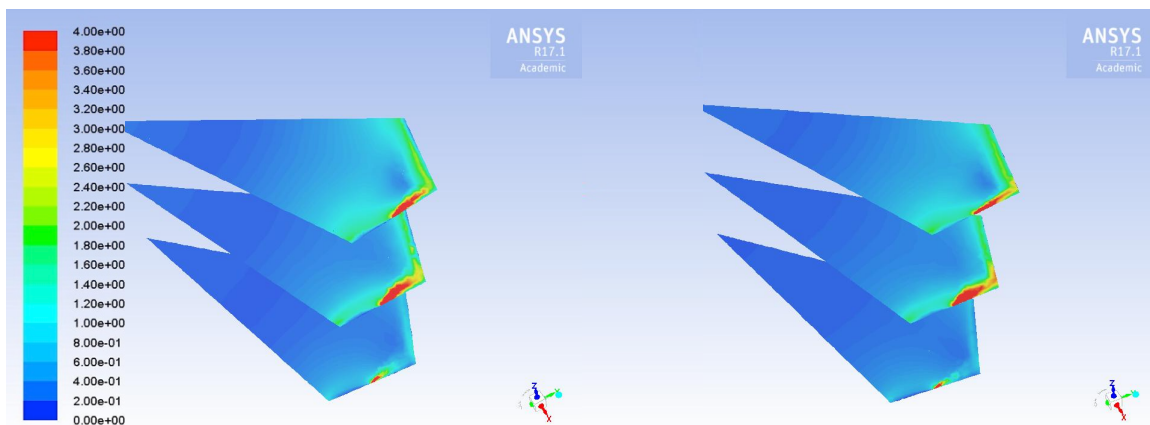
Figure 6.6: Veloplane 1-3 velocity magnitude contour conic (left) and cylindrical (right)

In **Figure 6.6**, velocity contours are displayed on veloplane 1,2 and 3. The left picture shows the conic outlet model, the right one the cylindrical outlet model. In order to see flow contours on the entire plane, maximum values are limited with 4 m/s. Values above 4 m/s are coloured in red as well. Both flow contours show a similar picture. At nozzle exits, maximum values are reached. Near-wall regions have the highest velocity values as they decrease towards the core volume. From this illustration, no significant difference in overall flow patterns is visible.

Figure 6.7 illustrates vertical velocity profiles at the respective periodic plane of the case. Higher velocities are shown in near wall regions of the model. Furthermore, velocities are higher in the centre-regions at upper z-axis locations of the model. Maximum velocities on this plane are located at 2,92 m/s for the conic model and at

2,70 m/s for the cylindrical model. Again, both cases show similar velocity contours. What is identifiable is the further spreading of the inlet sprays in the cylindrical model.
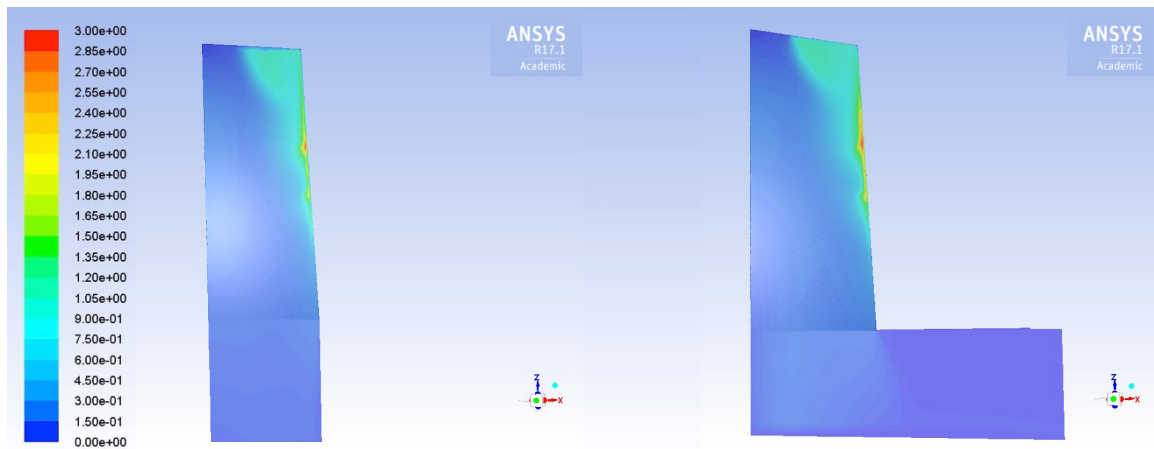
Figure 6.7: Periodic plane velocity magnitude contour conic (left) and cylindrical (right)

Figure 6.8 shows contours at the very bottom of the cloud chamber itself. The location of this plane is visualised in **Figure 6.1,** in which it is named outletplane.
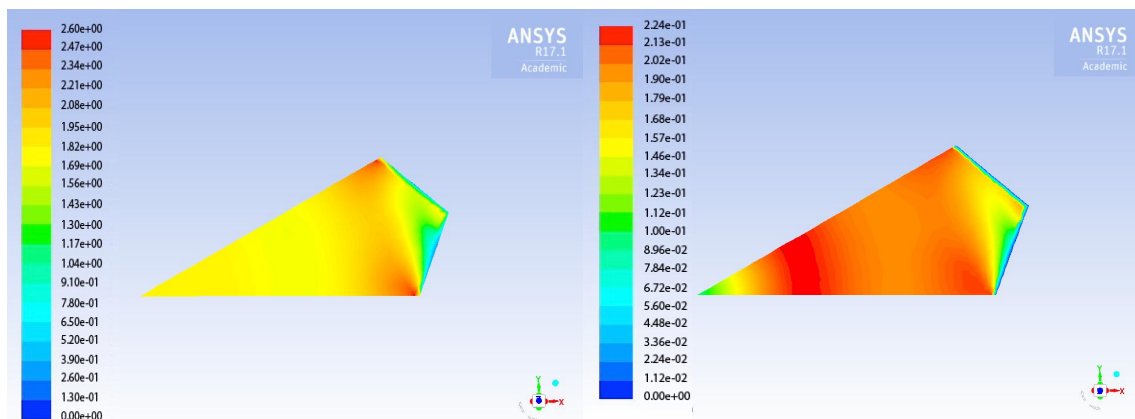
Figure 6.8: Velocity magnitude outlet plane conic (left) and cylindrical (right)

The left figure illustrates velocity contours at minimum of 0 m/s and maximum of 2,6 m/s, the right one shows contours between 0 and 0,22 m/s. A significant difference on flow patterns can be observed for this plane. The approximate inner two thirds of the left picture remain yellow, which corresponds to values of around 0,19 m/s In the right picture, values in the very core region remain at around 0,12 m/s, but the large part is coloured in red, and values of 0,22 m/s are present for the major part of the plane. This velocity gradient from the centre to the main part is the most significant difference in terms of flow patterns.

Static pressure contours in **Figure 6.9** show values in a range of $-3,9*10^{-2}$ to $2,19*10^{2}$ Pa for the conic case and $-8,52*10^{-2}$ to $4,26*10^{-3}$ Pa for the cylindrical case. While the cylindrical case displays a consistently spread pressure profile consisting of negative values in the middle to positive pressure values at the walls, the pressure profile of the conic case is not as balanced with its pressure distribution.
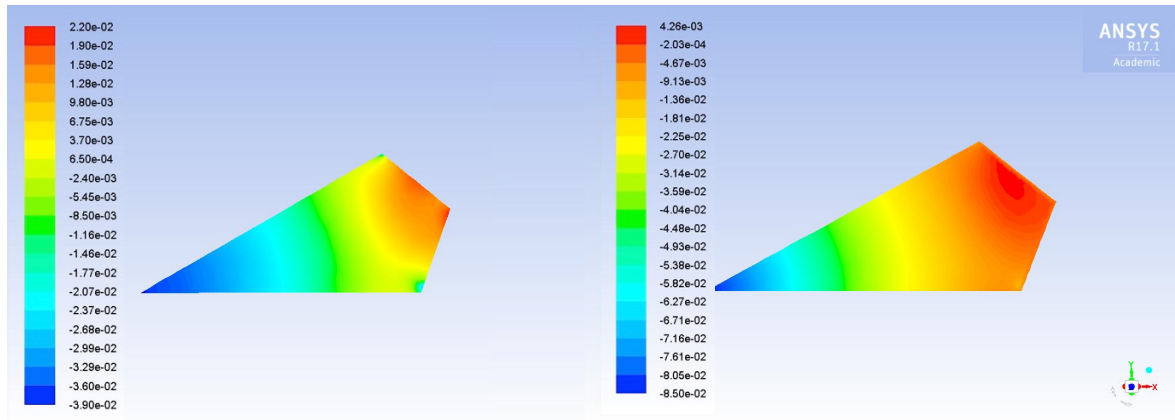
Figure 6.9: Outletplane static pressure contours conic (left) and cylindrical (right)

The difference in pressure distribution is also shown in **Figure 6.10**, where radial pressure distribution of a radial line through the centre of the domain is illustrated. This difference shows that the geometrical outlet condition also influences the simulation results in the area of main interest.
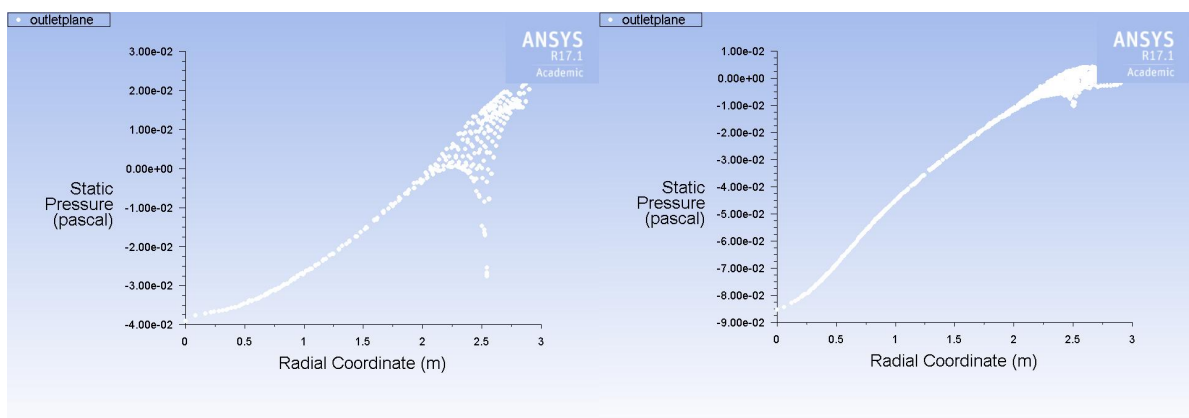
Figure 6.10: Outletplane static pressure plot conic (left) and cylindrical (right)

6.1.3 Outflow conditions
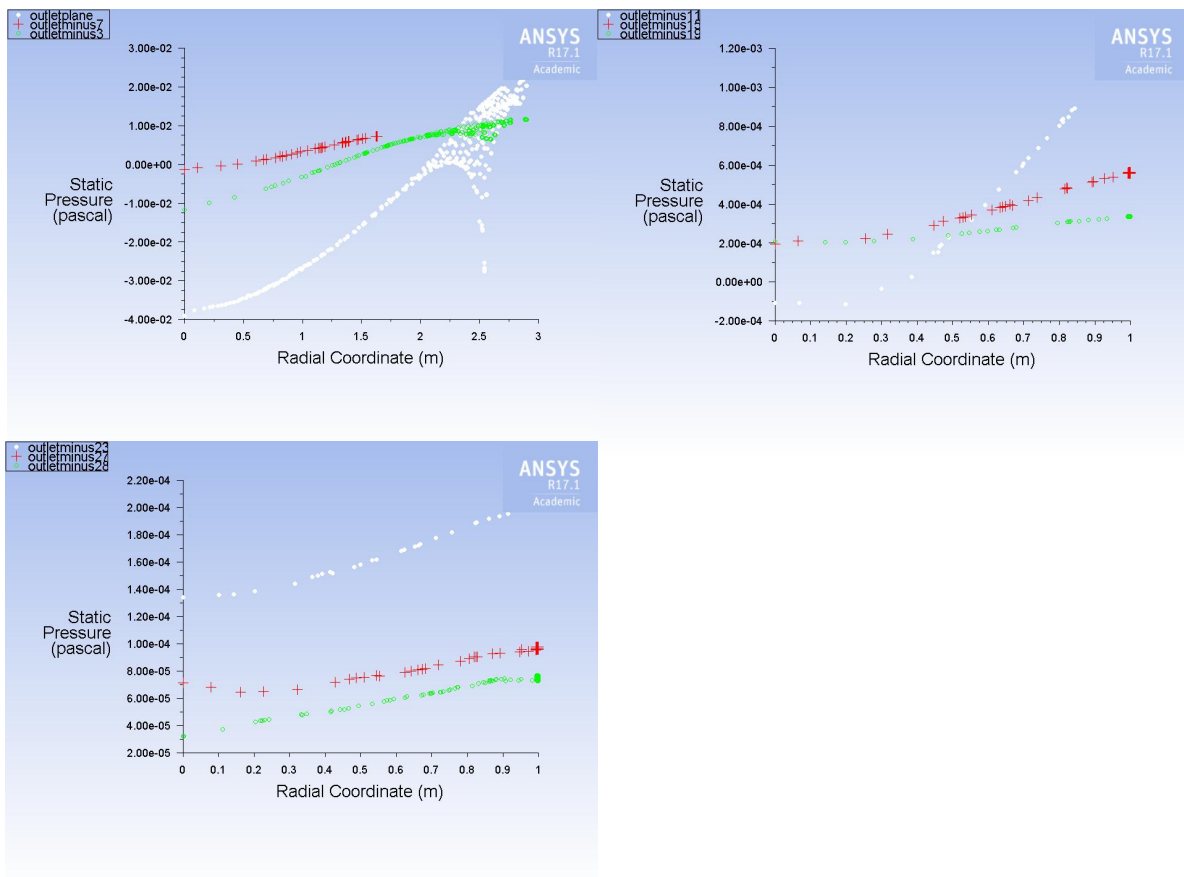
Figure 6.11: Horizontal static pressure plots conic case from outlet plane to domain end in 4 m gaps
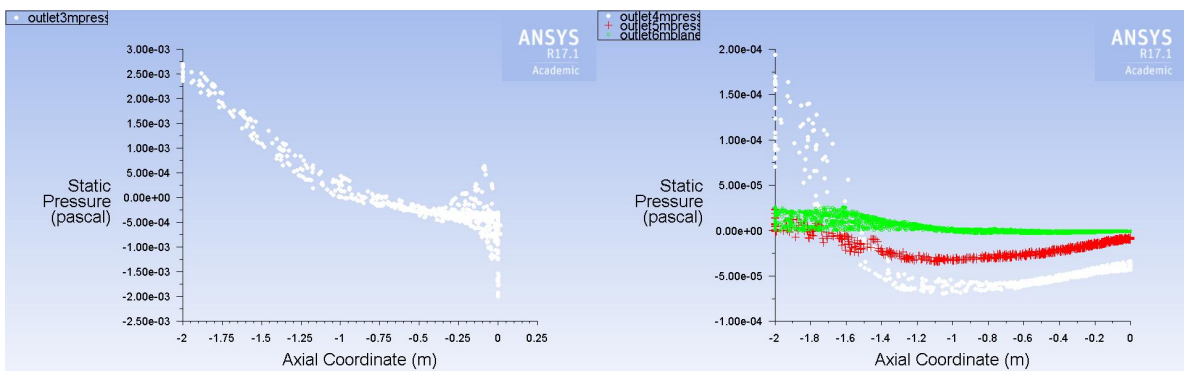
Figure 6.12: Vertical static pressure plots cylindrical case at 3,4,5 and 6 m distance from the center

In **Figure 6.11** and **Figure 6.12** pressure contours in the outflow region of the domains are presented for the compared cases. For the conic outlet case, horizontal planes in descending z-heights, beginning from the outletplane, show a disappearance of the high pressure point agglomeration at the walls with lower z-

values and a continuous flattening of the radial pressure profiles towards the pressure outlet.

In the cylindrical outlet case, vertical planes are compared, as the main outflow vector is expected to point in radial direction. The left picture shows an agglomeration of points around the z-coordinate of 0 m, where the wall boundary meets the pressure outlet boundary. With augmenting radial coordinates, the pressure profile straightens out in direction of a horizontal line. This shows that an enlargement of the calculation domain in radial direction seems to smooth out the outflow behaviour.

6.1.4 Dimensionless parameters
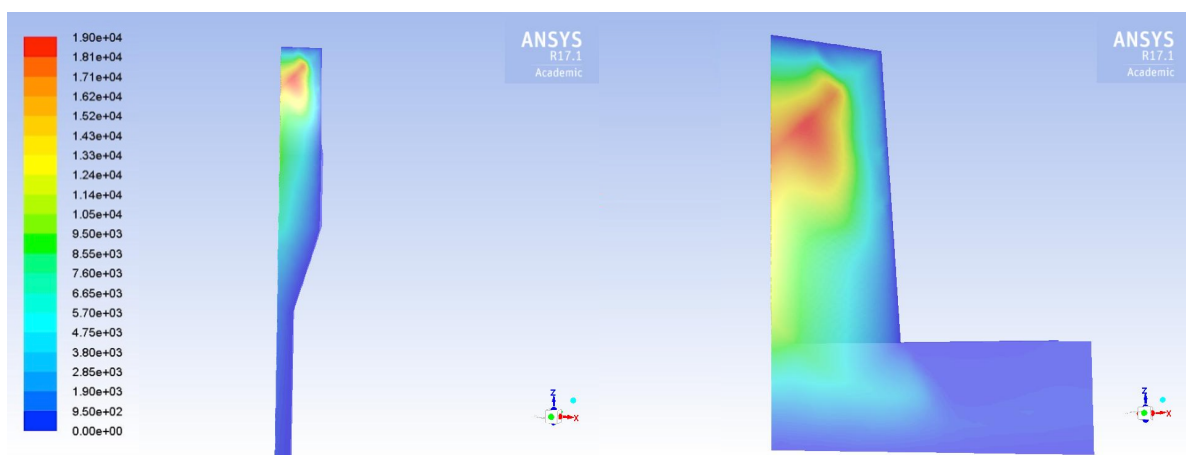
Figure 6.13: Turbulent Reynolds-number contour conic (left) and cylindrical (right)
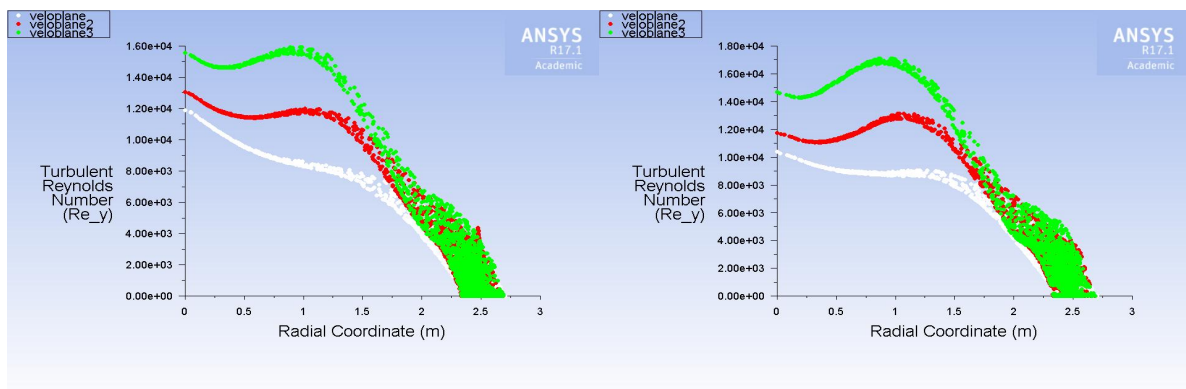
Figure 6.14: Veloplane 1-3 Turbulent Reynolds-number contour conic (left) and cylindrical (right)

In **Figure 6.13** contours of the turbulent Reynolds-number at the periodic plane are shown. Values of around $1{,}89*10^4$ and $1{,}77*10^4$ represent maxima. While the core turbulence region lies in the upper centre of the domain and has a very similar shape, development of Re_y looks different further downwards. The similarity of the Re_y development in the core region is also visible in **Figure 6.14**.

The airflow approach of the cloud chamber is aimed to be particle residence time maximizing. This should be achieved by applying swirling flow conditions in the chamber. Therefore, the swirl number is probably the most significant key figure when evaluating the flow.

Figure 6.15 shows vorticity values applied over the z-axis. Maximum values range up to $6*10^3$ and $1,4*10^4$ s^{-1}. Propulsion of the swirling flow is delivered by the nozzles, which are situated at the wall.

The three peaks in vorticity magnitude in both pictures can be interpreted as an illustration of the propulsion on three different levels. In the cylindrical case plot, three layers of vorticity magnitude are identifiable.
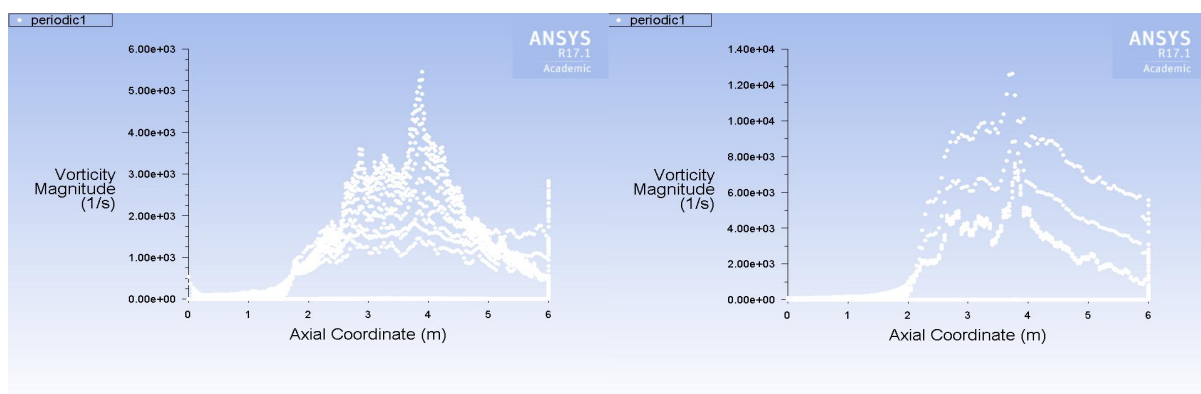
Figure 6.15: Vorticity contour conic (left) and cylindrical case (right)
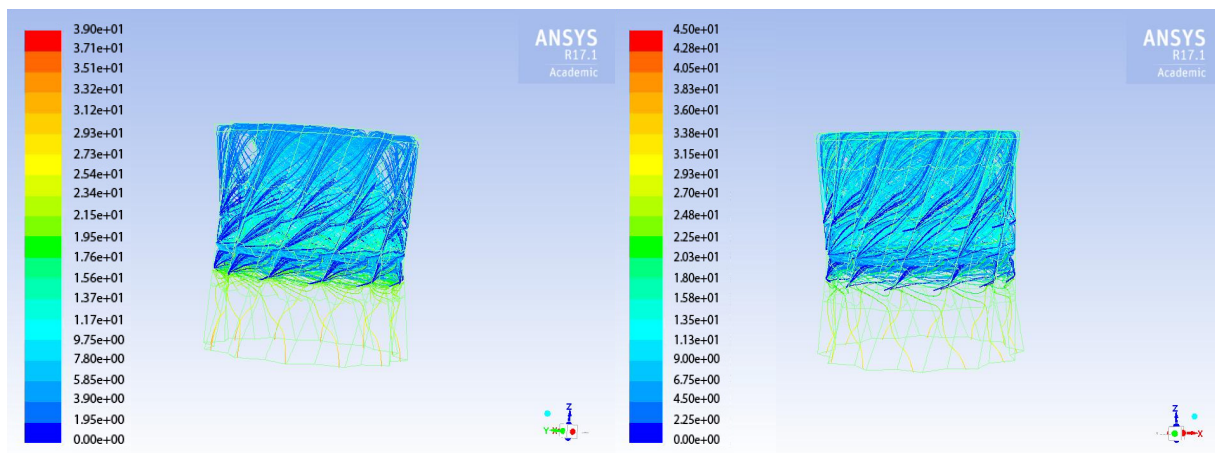
Figure 6.16: Pathlines coloured by residence time conic (left) and cylindrical (right)

Figure 6.16 shows pathlines, calculated until the first air particle tracks leave the actual cloud chamber. The conic model gives a minimum residence time of 39 s, while the cylindrical model shows a value of 45 s. These values need to be evaluated and a measurement of crystal growth during that time period is necessary for a rating of the calculated residence time.

6.2 Case II – comparison of turbulence models

6.2.1 Convergence

Table 6.1: Convergence judging - turbulence models
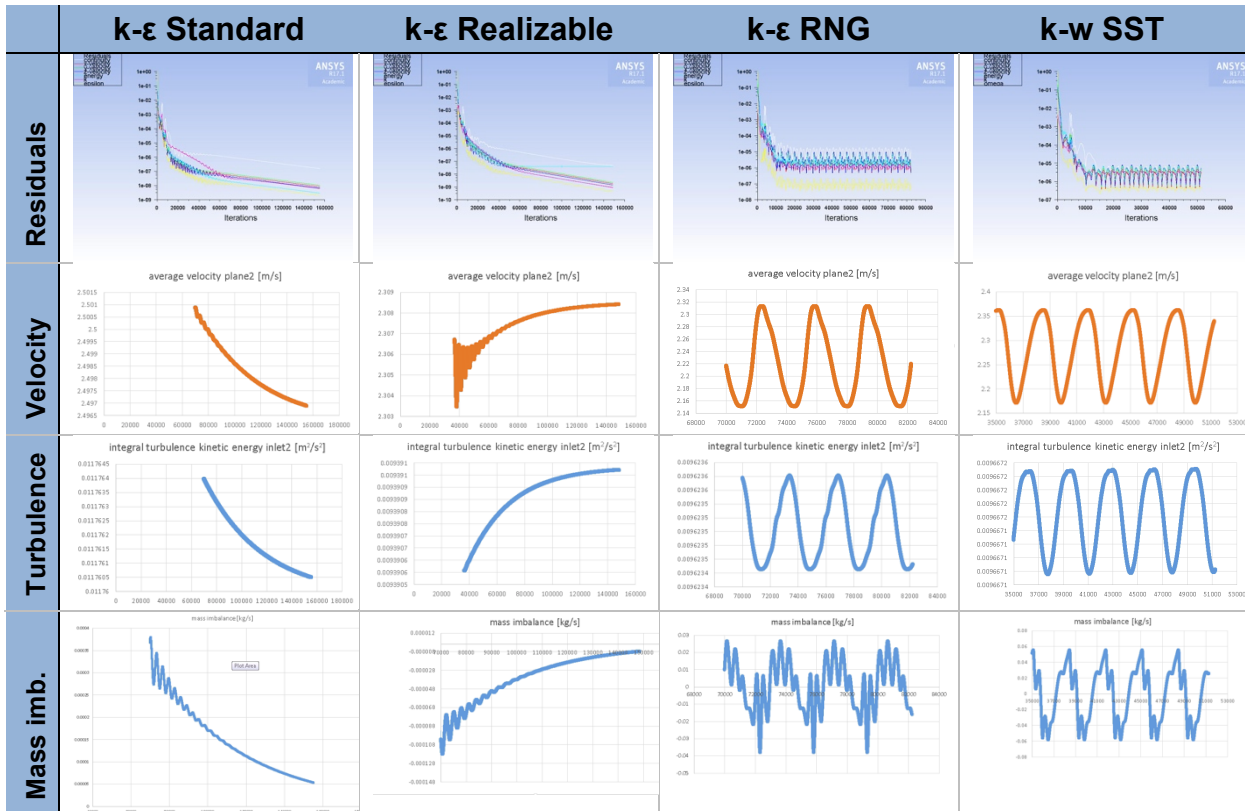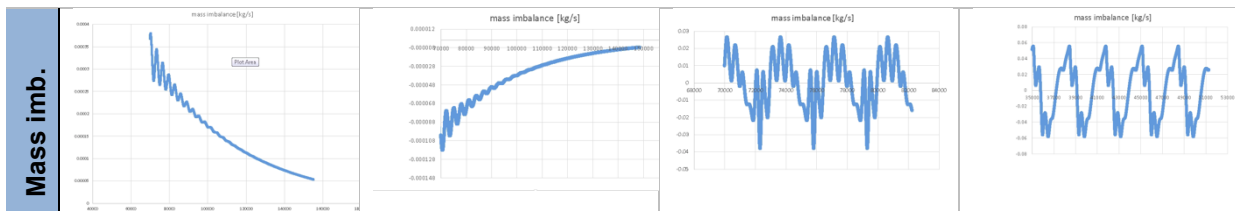
Table 6.1 shows an exemplary selection of velocity, turbulence and massflow monitors that helped judge convergence. k- ε standard and realizable turbulence models, respectively show clear tendencies of a non-alternating solution. Residuals for both cases are situated in a range between 10^{-6} and 10^{-8} after 150 thousand iterations. Mass imbalance with k-ε standard model is at $5*10^{-5}$ kg/s which is around 0,5 % of the total inflow value. With k-ε realizable it is at $8*10^{-6}$ kg/s, which corresponds to less than 0,1 % of the total inlet mass flow. For a closer understanding of the case's solutions, further monitored values can be reviewed in Appendix D.

Using kω-SST and kε-RNG turbulence models, residuals diminish to values of 10^{-4} to 10^{-5} after 15 000 iterations. Although residual levels are sufficiently low, significant fluctuations are present. This behaviour also reflects in monitored values. Further iterations do not cause changes in convergence behaviour, as the fluctuations are still present. While integral turbulence values alternate in a 0,01% range of the absolute value, average velocities vary in a 10 % range for both, the kw-SST and k-ε RNG model, respectively. Furthermore, mass imbalance alternates about a value, ten times bigger then the entire inlet massflow. Velocity contours that monitor one periodic sequence are present in Appendix D. A pulsation of the vertical velocity spreading can be observed here in both, the k-w SST and the k-ε RNG cases.

Due to the non-converging solutions of the two latter cases, only outcomes of k-ε standard and k- ε realizable models will be discussed further.

6.2.2 Flow field
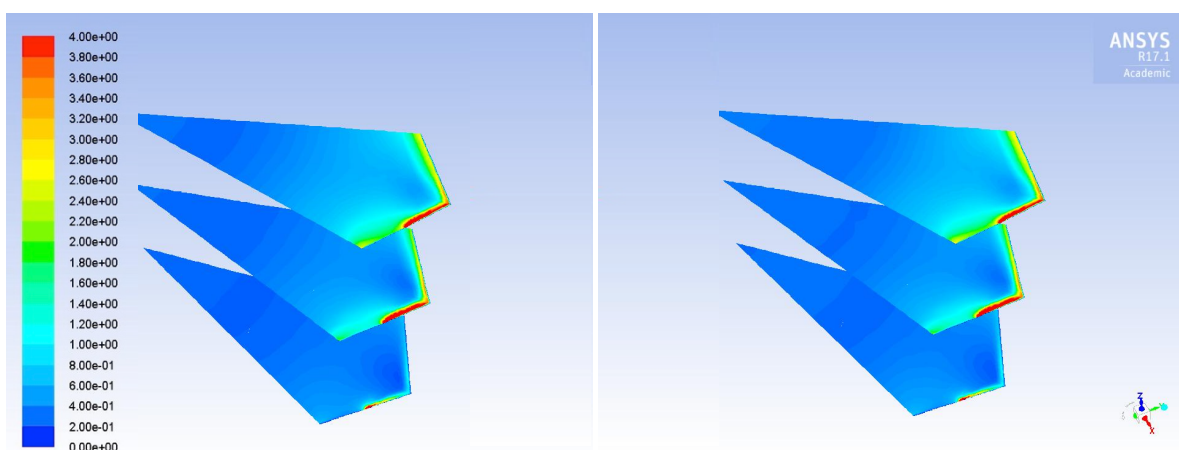
Figure 6.17: Velocity contours veloplanes 1-3 standard k- ε (left)/realizable k-ε (right)

In **Figure 6.17** velocity contours of 0 to 4 m/s are illustrated. Higher velocities, which would occur at the nozzle locations, are also coloured in red, as it helps the illustration of the velocity contour. Standard k-ε and Realizable k-ε turbulence models show a very similar solution of the flow field. Broader and narrower strips in the 0 to 0.7 m/s range near the centre of the periodic computation domain mark the biggest differences in this picture.
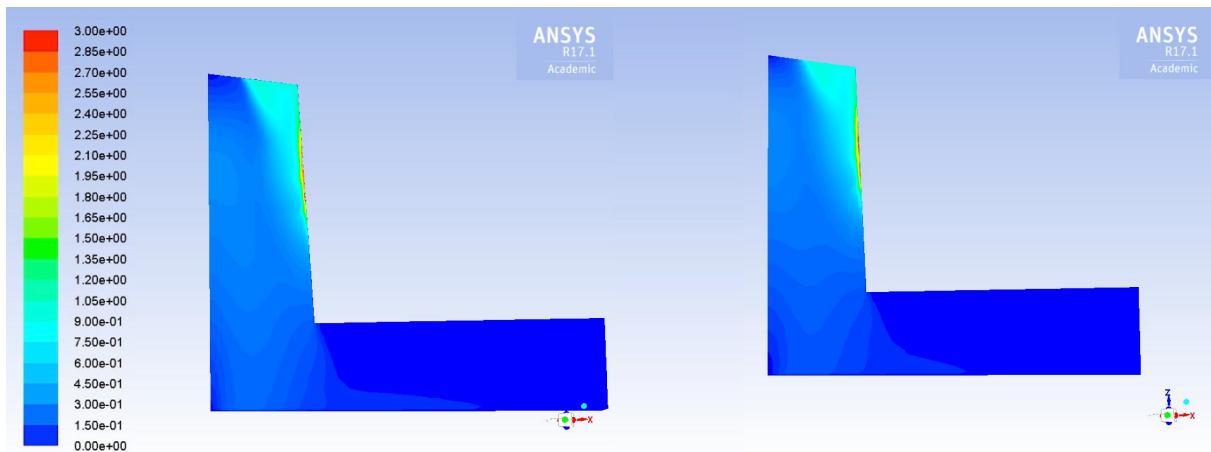

Figure 6.18: Velocity contours standard k- ε (left)/realizable k-ε (right)

Velocity magnitude contours with maximum values of 3 m/s are confronted in **Figure 6.18**. Contours in the upper half of the domain look very similar. The velocity spreading in the lower part is further pronounced with the standard k- ε model.
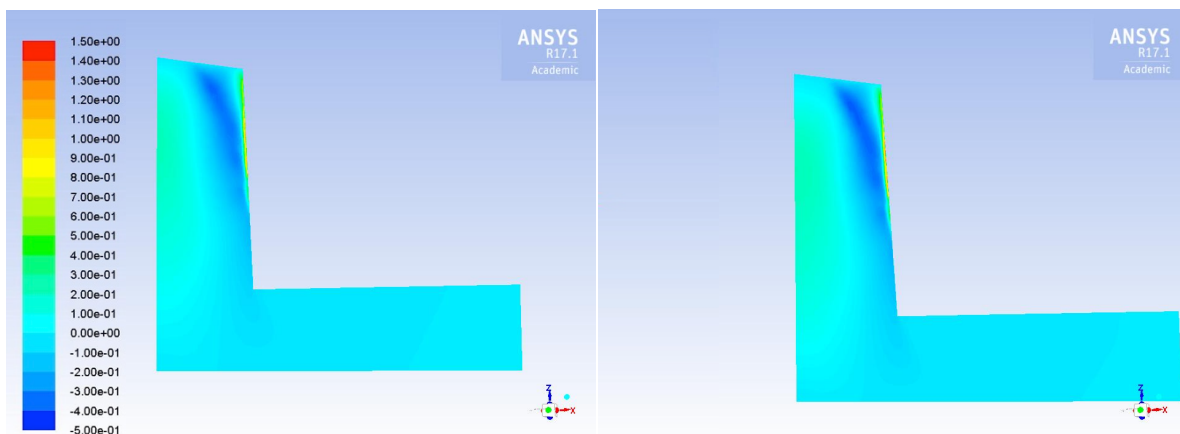
Figure 6.19: Axial contours periodic plane standard k- ε (left)/realizable k-ε (right)

Figure 6.19 shows axial velocities of -0,5 m/s at the outside region of the domain and 0,3 m/s in the centre region for both models. Maximum values are present in the wall boundary region due to the presence of the inlets.
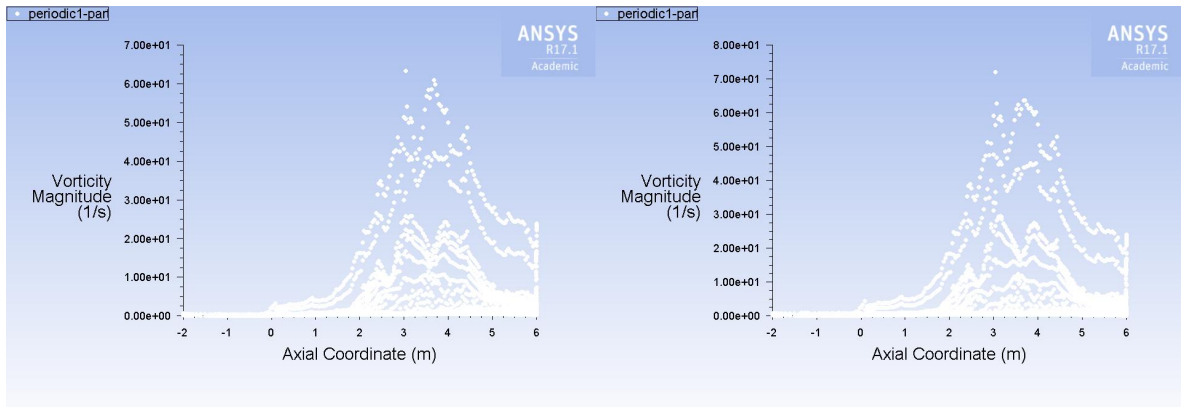
Figure 6.20: Vorticity plot standard k- ε (left)/realizable k-ε (right)

Vorticity magnitudes of the Standard k-ε model have their maximum at 6 s^{-1}, those of the realizable k-ε model at 7 s^{-1}, at a height of 3 m, respectively. Patterns of the value look similar, so the drive of rotation is displayed similar with the distinct turbulence models.
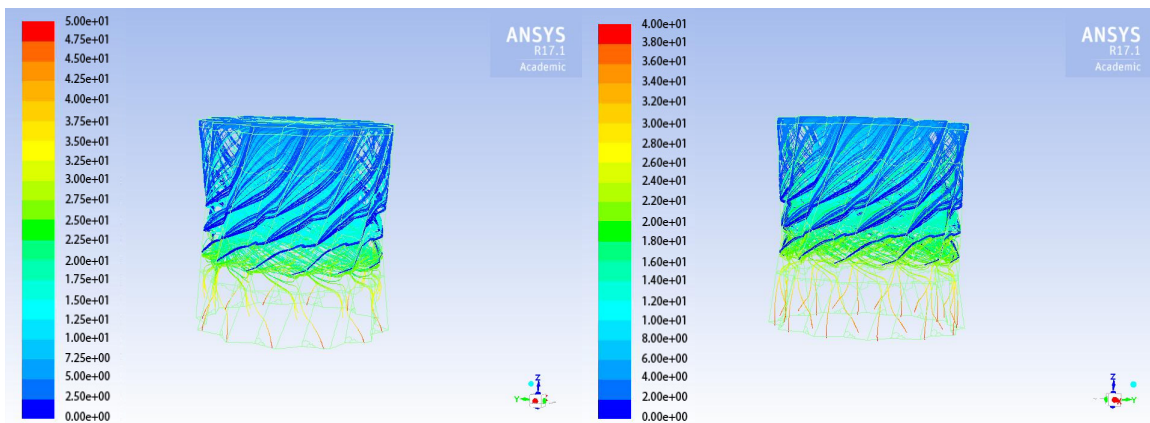
Figure 6.21: Pathlines coloured by residence time standard k- ε (left)/realizable k-ε (right)

Pathlines, displayed in **Figure 6.21** are coloured by their time of residence in the domain. Again the calculation was run, until the first particle tracks exit the domain resulting in the minimum residence time. This results in 50 s for the standard k- ε model and 40 s for the realizable k- ε model. Pathlines have very similar patterns.
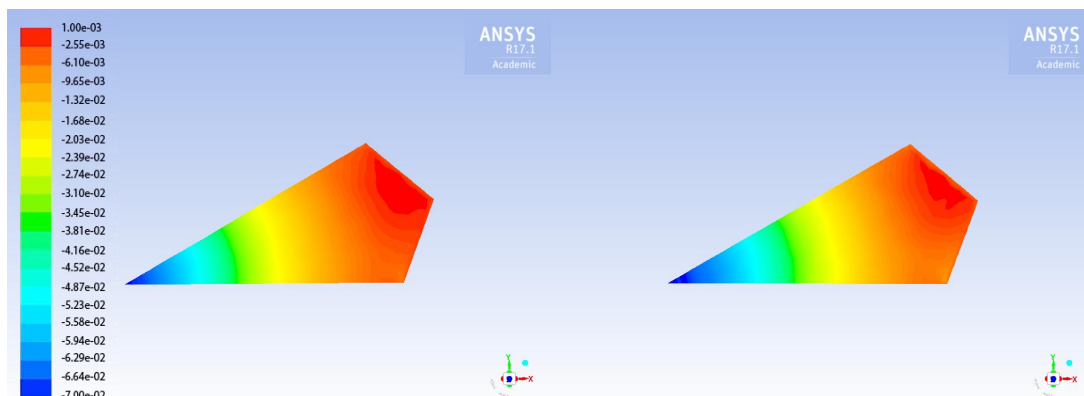
Figure 6.22: Static pressure contours outlet standard k- ε (left)/realizable k-ε (right) plane

A linear pressure drop into the centre of the domain is observable on the horizontal outlet plane. This indicates a flow in z-axis from which negative pressure in the suction region (coloured blue to green), and positive pressure values in the downstream region (coloured yellow and red) of the flow is created. Static pressure contours have a maximum at $9,34*10^{-4}$ Pa and a minimum value of $-3,3*10^{-2}$ Pa. Static pressure is a value, which is "relative to the operating pressure" of the case [46]. What is noticeable is the development of a larger region of high-pressure contour on the right upper end of the plot with the realizable turbulence model.

6.2.3 Turbulence
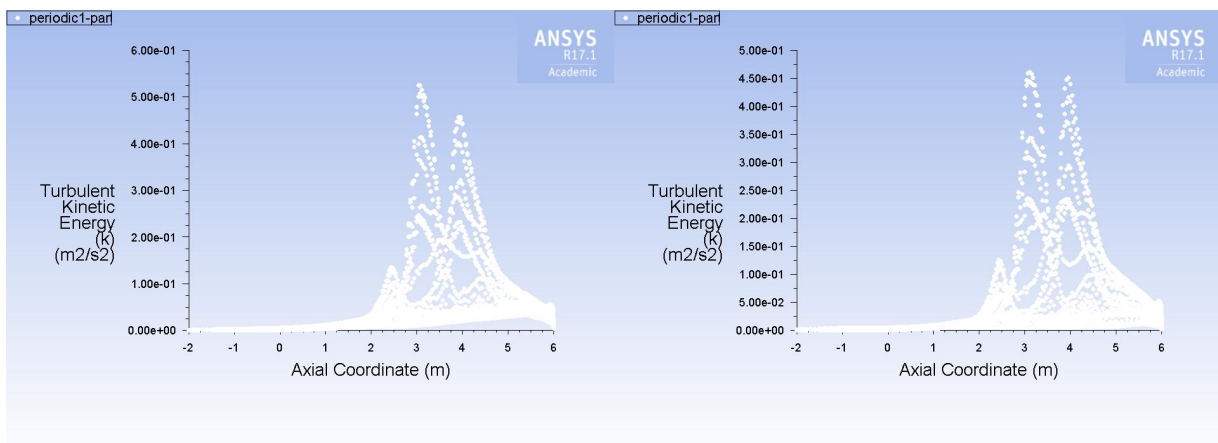
Figure 6.23: Turbulent kinetic energy standard k- ε (left)/realizable k-ε (right)

The turbulent parameter, illustrated in **Figure 6.23** presents turbulent kinetic energy along the axial coordinate of the periodic boundary. While with the standard k-ε turbulence model turbulent kinetic energy augments to a maximum of 6 m^2/s^2, the maximum value for the realizable k-ε turbulence model lies at 4,5 m^2/s^2. Three peaks of turbulent kinetic energy, as well as turbulent intensity occur respectively. Those peaks can be related to the inlets, where high velocities and compressed fluid flow are present, as the z-coordinates correlate with the z-coordinates of the inlets. Furthermore, turbulence creation at the very top of the domain is of higher consideration with the realizable k-ε turbulence model.

Turbulence and pressure levels are marginally higher with the realizable k-ε model and more solid convergence results can be reached with a certain number of iterations. Therefore it will be used for further development of the model.

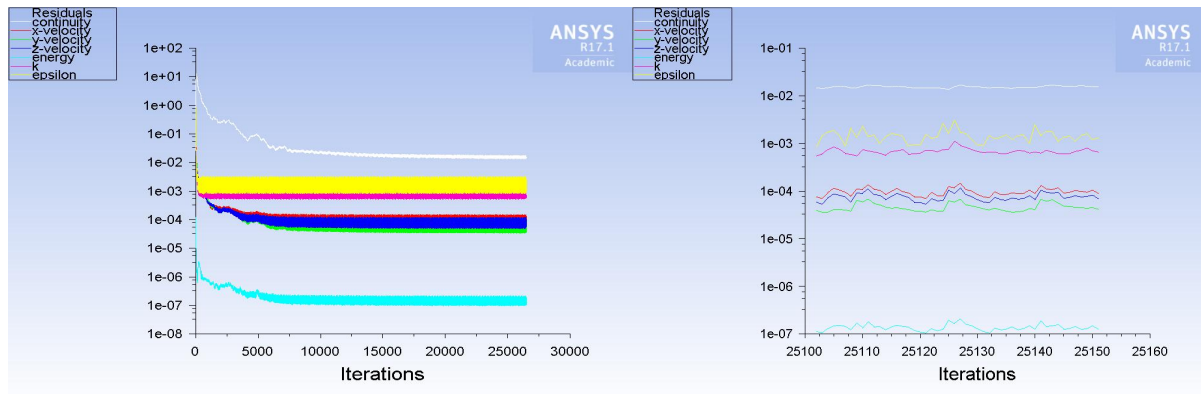# 6.3 Case III – solver comparison

6.3.1 Convergence

Figure 6.24: Residuals pressure based

Looking at **Figure 6.24**, the residuals of this case have settled to a steady value after 15 000 iterations, although they are wide spread. Energy is well under a value of 10^{-6}, while continuity has settled in a range of 10^{-2}. Values of k and ε vary around 10^{-3} and residuals of velocities vary around 10^{-4}. The right half of the figure gives a closer look on the residuals. Although there is no periodic pattern present, value levels stay in a constant range. **Figure 6.25** again represents an exemplary excerpt of monitored values. Average velocities show periodic fluctuations, but converging behaviour, as they vary around 0,05 % of their absolute value at the iteration finish. Turbulent kinetic energy, mass imbalance and interior mass imbalance also show a periodic behaviour. Still, turbulence kinetic energy varies in a 0,5% range of its absolute value and mass imbalances have their maximum at absolute values of $6*10^{-6}$.
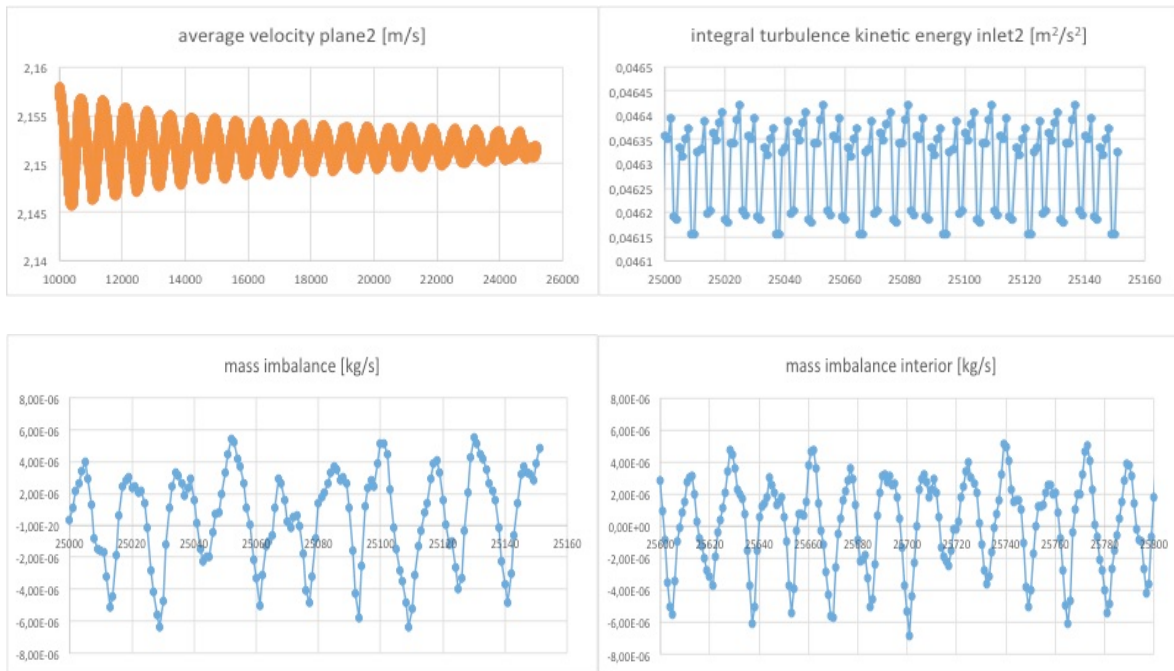
Figure 6.25: Convergence monitors pressure based

6.3.2 Flow field
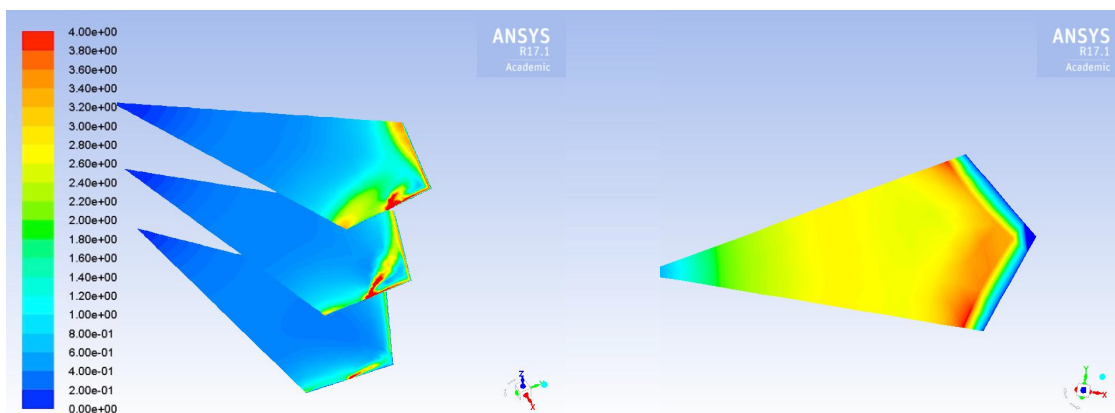
Figure 6.26: Velocity magnitude veloplanes (left) & outletplane (right)

The initiation of the flow happens via the nozzles, where highest velocities occur. **Figure 6.26** shows velocity contours at two areas of interest. The left half illustrates velocity contours of the velocity planes. A striking property is the far spreading of high velocities nearby the jets. Velocities are below 1 m/s in the majority of these fields. The figure's right side shows velocities at the outletplane, where the velocity distribution is more balanced. Maximum values of 0,44 m/s are given in the outer section of the plane, whereby near wall regions are affected by the boundary layer.
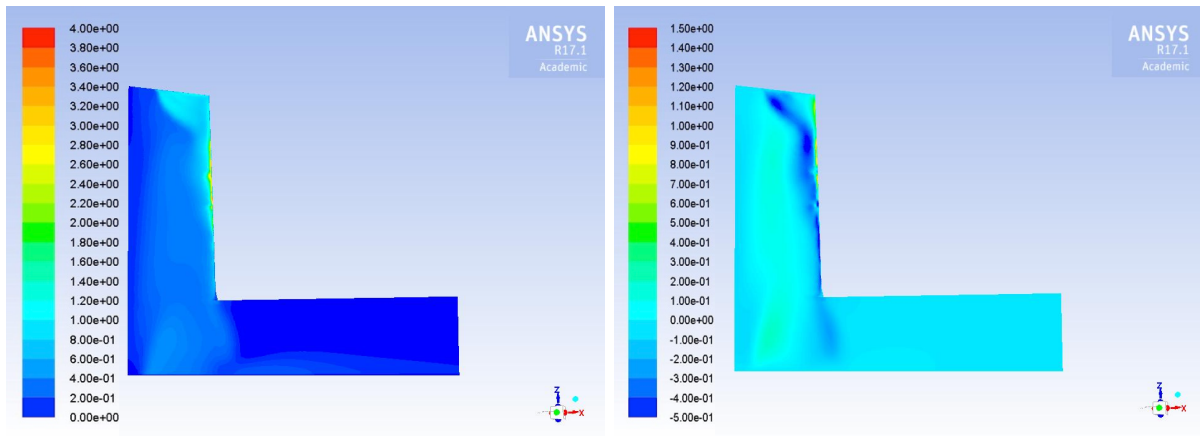
Figure 6.27: Velocity (left) & axial velocity (right) magnitude periodic plane

At the periodic plane, velocity contours show a maximal value of 4,57 m/s, located at near-wall regions. The majority of the velocity contour shows velocities below 1 m/s. Axial velocities show negative values at the outer region and positive values at the inner region of the model. This indicates a circulation in the vertical axis. **Figure 6.28** shows vorticity along the z-axis, including three peaks at 2, 3 and 4 m, at values of, 500, 1000 and 700 1/s. Minimum residence time of air particles are illustrated in **Figure 6.29**. Values are located at around 24 s.
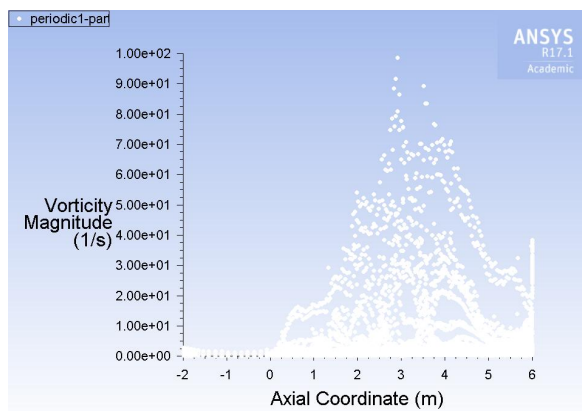
Figure 6.28: Vorticity magnitude periodic plane
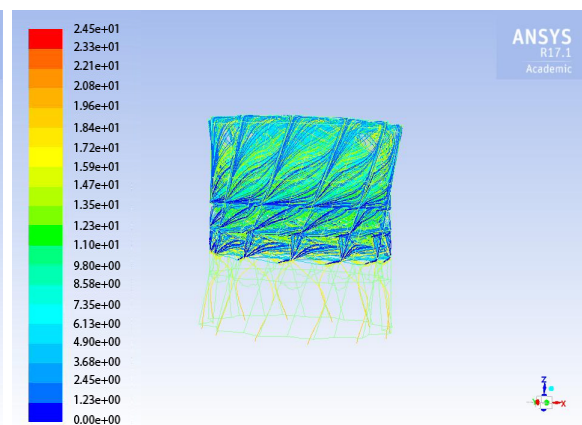
Figure 6.29: Pathlines – residence time

6.3.3 Turbulence
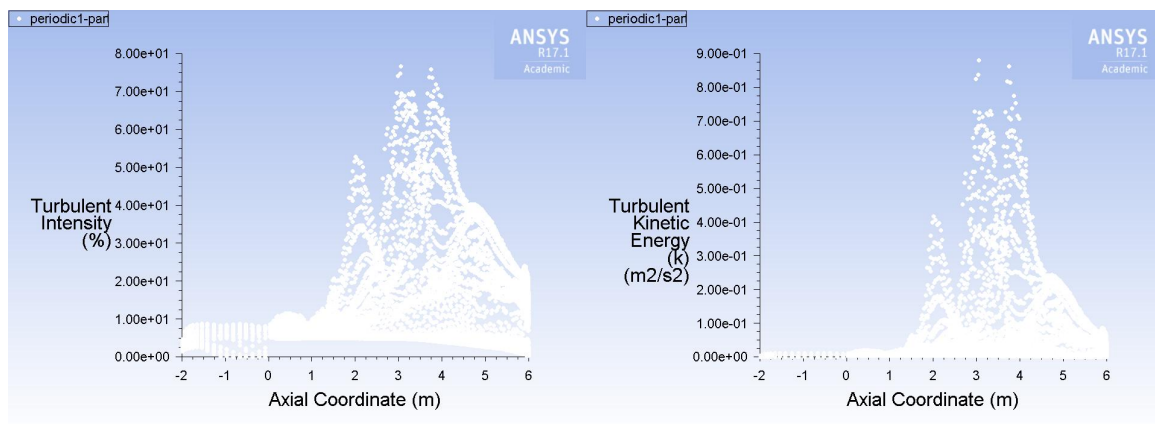
Figure 6.30: Axial turbulence values

As shown in **Figure 6.30**, turbulent intensity and turbulent kinetic energy augment at z-coordinates of inlets. Turbulent kinetic energy has it's maximum at 0,9 m^2/s^2 and turbulent intensity augments up to 80 %.

7 Cooling tower analogy

While airflow simulations could be executed via numerical methods, the inclusion of heat transfer problems could not be executed. Although the generation of heat inside the chamber was an issue that had to be treated, causing problems with the snowmaking process from the beginning, because it has a very limiting influence on the entire process.

As described in Chapter 2.2.1, constant energy generation is given with the process of snow production. Heat is produced and a temperature rise in the plant is the consequence. **Figure 3.6** and **Figure 3.7** show measurements during a test period, including temperatures inside and the outside of the cloud chamber. What can be observed is the development of a temperature gradient between the cloud chamber and the surrounding atmosphere during the test run, which happens due to the heat production inside the cloud chamber.

Searching for a way to optimize the heat transfer outward of the cloud chamber and therefore thinking through various concepts on how to accomplish this, the concept of a cooling tower seemed favourable for the conditions, which are present in the cloud chamber. An analytical comparison of a cooling tower and the cloud chamber will be presented in this chapter.

Baker et al [32] basically bring together validated information on evaporative cooling in order to develop a design guide for cooling towers. Fundamental element of the approach is the Merkel-equation [51]. The concept is defined as follows: "The analysis combines the sensible and latent heat transfer into an over-all process based on enthalpy potential as the driving force." [32]
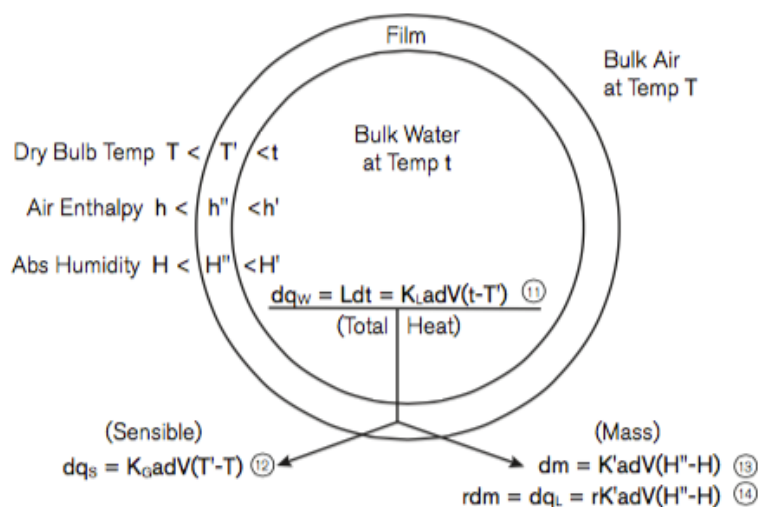

Figure 7.1: Bulk water surrounded by an interfacial film [32]

Figure 7.1 illustrates the concept, described above. Every water particle of the bulk water is surrounded by an interfacial film. This film presents the barrier to the air in the system. Heat transfer happens between the droplet and the film and between the film and the air. Both, transfer of sensible and latent heat is being taken into account, while the latter equals the evaporation of the bulk water. Integrating the equation

$$L dt = KaV(h' - h) = G dh \qquad (7\text{-}1)$$

leads to

$$\frac{KaV}{L} = \int_{t_1}^{t_2} \frac{dt}{h' - h} \qquad (7\text{-}2)$$

$$\frac{KaV}{G} = \int_{h_1}^{h_2} \frac{dt}{h' - h} \qquad (7\text{-}3)$$

in which K represents the overall unit conductance, mass transfer between saturated air at mass water temperature and main air stream, , a is the water interface area, L the mass flow rate of water, G the air mass flow rate, V is the active cooling tower volume, t is the bulk water temperature, h is the enthalpy of moist air and h' the enthalpy of moist air at bulk water temperature.

This approach can be made by ignoring any resistance to mass transfer from bulk water to interface, by ignoring the temperature difference between the bulk water and interface and by ignoring the effect of evaporation.

Figure 7.2 is a schematic sketch of how the cooling process could be achieved. In analogy to a counter flow cooling tower, warm, humid air is sucked out on the top of the cloud chamber while cold, dry air is sucked into the cloud chamber in the same amount. This should be achieved by the installation of a fan on top of the construction. **Figure 7.2** was created in analogy to the drawn graph in Baker et al [32], in which the counter flow cooling tower process is visualized. While in the cooling tower "water is entering the top of the cooling tower", which is "surrounded by an interfacial film that is assumed to be saturated with water vapour at the bulk water temperature", in analogy water nozzles introduce fine water droplets from the top of the cloud chamber and get surrounded by a film of saturated air, immediately.
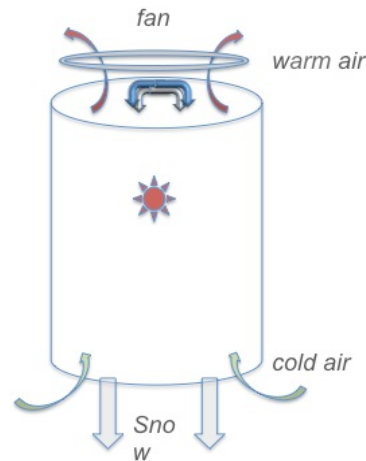
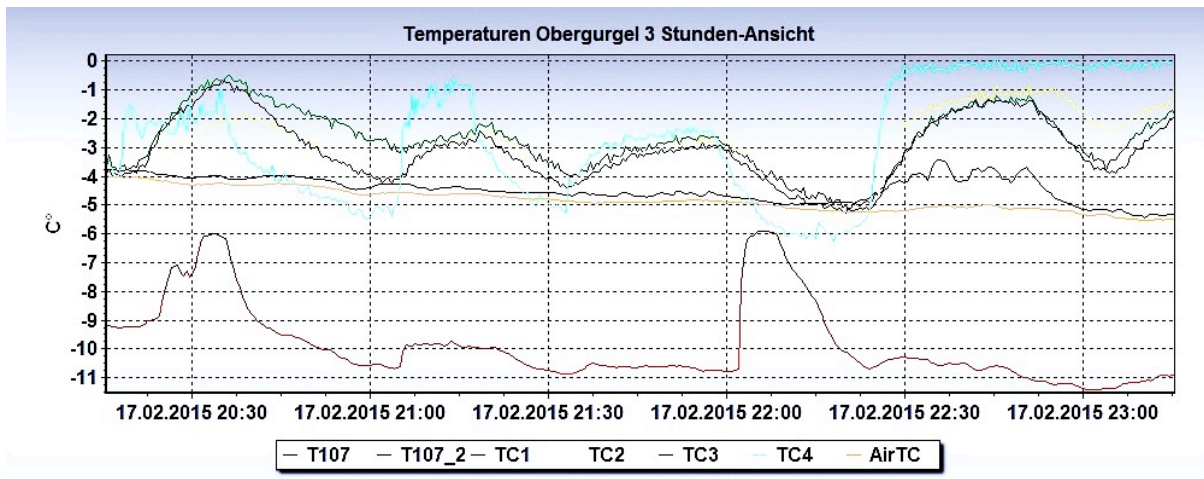**Figure 7.2:** Cooling process principle

Figure 7.3: Temperature levels during the operation of the dendrite generator © Neuschnee GmbH

During the trials of the outdoor pilot plant in winter 2014/15, air temperatures inside and outside the cloud chamber were measured. **Figure 7.3** shows temperature values during a three-hour time period before and during a test timespan. What is striking is that after the initial stage of the process, a constant temperature inside the cloud is setting in. For shown conditions a temperature difference ΔT of 6 °C between the inside and the outside temperature is a common value. At lower temperatures more water can be introduced to the cloud chamber and a higher temperature difference will therefore be achieved. For the discussed model, the case of maximal considered temperature difference is being applied in order to see the potential of the effect. These maximum values are an outside temperature of 253 K and an inside temperature of 273 K.
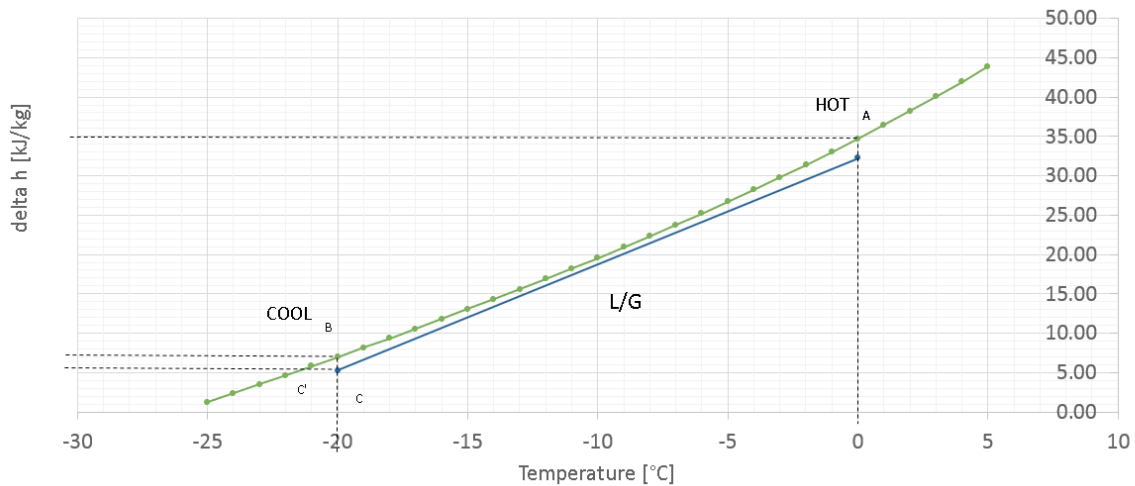
Figure 7.4: Cloud chamber enthalpies

Water is entering through the nozzles from the top, which is relating to point A on the saturation curve. As the water is cooled to t_2, the film enthalpy follows the saturation curve to point B. Air entering the base of the cooling tower at wet-bulb temperature T_{WB} has an enthalpy corresponding to C' on the saturation curve. The driving force at the base is represented by the vertical distance BC. Heat removed from the water is added to the air so its enthalpy increases along the straight line CD, having a slope equaling the L/G ratio and terminating at a point vertically below point A.

The slope of L/G represents the ratio of water and gas introduced to the plant. It is different for every cooling tower and limited by constructive restrictions. For the design of this cooling concept, the introduced mass of water was already defined by the requirements of snow processing. By choosing the amount of air, the curve gets the required gradient.

Table 7.1: Reference properties air   **Table 7.2:** Isobar specific heat of vapour [34]

Tref	-25	°C
p_2000m	101325	Pa
Rair	287,058	J/(kgK)
standard_rho	1,225	kg/m³
L	5000	kg/h
G	40816	kg/h
L/G	0,1225	

T [K]	cp,v [kJ/kgK]
175	1,85
200	1,851
225	1,852
250	1,855
275	1,859
300	1,864
325	1,871

Table 7.1 and **Table 7.2** show reference properties of air and calculations of specific heat for water vapour.

Enthalpy values were calculated according to the formulae for humid air:

$$dh = c_{pa}dT + Hc_{pv}dT + \left[r + c_{pv} * (T - T_0)\right]dH \qquad (7\text{-}4)$$

Using $\varphi_{in}=30$ and $\varphi_{out}=90\%$, this gives the following values:

$$h_{in} = 5{,}7 \frac{kJ}{kg} \qquad (7\text{-}5)$$

$$h_{out} = 34{,}4 \frac{kJ}{kg} \qquad (7\text{-}6)$$

While the amount of water is given with L = 5000 kg/h, an air mass of G = 40800 kg/h is needed to achieve required cooling curves. Calculations of humid air enthalpy and absolute water humidity are present in Appendix G. For calculations of enthalpy, a reference temperature T_0 = 248 K was used. As the enthalpy difference dh is the value of interest, this doesn't affect the calculations. Still, it is not common in above-zero calculations, and needs to be mentioned.

Besides the conditions, resulting from cooling tower analogy, another limiting aspect is the drag of a snow flake inside the dendrite generator. If the drag force, generated by the main flow velocity during the process, is too high, the water particles get dragged out by the air flow at the top before a snow crystal formation can happen. This condition is defined by the following drag formula [52]:

$$F_D = \frac{1}{2}\rho_F v_F{}^2 C_D A \qquad (7\text{-}7)$$

,where ρ_F represents the fluid density, v Is the fluid velocity, C_D the drag coefficient and A the projected area of the particle. The condition for the particle not to get sucked out on top of the cloud chamber is related to gravity force:

$$F_G = m \cdot g \qquad (7\text{-}8)$$

and is defined as:

$$F_D \leq F_G \qquad (7\text{-}9)$$

Table 7.3 shows used values for the calculated case in which fluid density is the one of air. The projected area is the one of a sphere particle of the size given by nozzle manufacturers. [7]

Table 7.3: Applied properties for drag calculations

ρ_F	1,225	[kg/m³]
A	$7 \ast 10^{-6}$	[m²]
m	$1{,}796 \ast 10^{-13}$	[kg]
C_D	0,47	[1]
g	9,81	[m/s²]

As a result of the physical condition, described in (7-7) and (7-9), a maximum flow velocity can be achieved:

$$v \le \sqrt{\frac{2 \cdot F_G}{\rho_F A C_D}}$$
(7-10)

The condition for the water droplets not getting soaked out the cloud chamber before the phase change into vapour is situated at a fluid velocity of $v_F = 0{,}47$ m/s. This condition represents another restriction for the redesign of the cloud chamber in terms of the use of evaporative cooling.

If the size of the cloud chamber is sufficiently large and therefore, the flow path of the air is long enough, so vaporization and heat transfer can take place and the air can be saturated, is not clear yet. Furthermore the flow velocity should be considered for a redesign of the prototype. A validation of the approach is planned for the next testing period.

8 Discussion

After the presentation of the CFD results, some questions will be discussed. The stability of the calculated CFD cases was highly dependent on the grid used. Also the numerical solver showed big differences on iterations. While the pressure-based solver provided a steady solution after only 15 000 iterations, the density-based solver did provide satisfying results after 130 000 iterations and more, which is an argument for a further development of the model, using the pressure-based solver. Nevertheless convergence monitoring gave the most satisfying results with the realizable k-ε model, as values converged to certain numbers, showing no fluctuations. Due to the computational effort, which is significantly lower, applying the pressure based solver, I would recommend this solver for the further development of the model. **Table 8.1** shows an overview of convergence numbers.

Table 8.1: Iteration steps and convergence numbers

	Case I	Case II	Case III				
	conic	cylin-drical	k-e Standard	k-e Realizable	k-w RSST	k-e RNG	Pressure-Based
Iteration steps (in 1 000)	131	242	150	150	150	150	15
Residuals	10^{-7}-10^{-9}	10^{-6}-10^{-9}	10^{-6}-10^{-8}	10^{-6}-10^{-8}	10^{-6}-10^{-8}	10^{-6}-10^{-8}	10^{-2}-10^{-6}
Max mass imbalance (in % of inlet mass flow)	1 %	500 %	0,5 %	<0,1 %	1000 %	1000 %	0,01 %
Max fluctuations integral turbulent kinetic energy	<0,01 %	0,0012 %	-	-	0,01 %	0,01 %	0,5%
Max fluctuations average velocity	<0,01 %	3 %	-	-	10 %	10 %	0,05 %

Another observation was that the coarse boundary layer in the near-wall region, using Scalable Wall Function, interfered with a proper spreading of the spray, using the density-based solver. The high-resolution grid, used for Enhanced Wall

Treatment, made it impossible to generate a grid of high quality. Orthogonal quality and skewness thresholds, defined by Fluent, could not be achieved. The pressure-based solver, on the other hand, permitted the use of SWF while a spreading of the jet spray was reached. A quantification of spray width deviations was not possible due to lack of jet measurement instruments and manufacturer data. **Table 8.2** gives an overview on applied methods.

Table 8.2: Solver, turbulence and near-wall treatment overview

	Case I	Case II	Case III
Pressure-based (PB) / Density-based (DB)	DB	DB	PB
Scalable Wall Functions (SWF)/ Enhanced Wall Treatment (EWT)	EWT	SWF	SWF

Table 8.3 shows characteristic variables that illustrate differences in the outcomes of the executed cases. Vorticity values of Case I show differences, compared to the other two cases, as they vary by a factor of 10^2 at their maximum, while vorticity structures show similarities for all three cases with peaks at axial positions of the jets. An explanation for this high difference of the cases is the cell size closest to the wall as it is very small with applied EWT for Case I and significantly bigger for Case II and Case III. Values of high velocity mean values of high vorticity, which is shown in (2-18). Those are captured in boundary regions, where grid points are present with EWT, while the coarse boundary layer does not gather these near-wall values. Static pressure values are in similar ranges for all cases, so is the turbulent intensity. The minimum residence time for the air particles gives values between 24,5 s in Case III and 50 s in Case II. Those values are similar, which indicates that the boundary layer treatment has no major influence on general flow structures in the cloud chamber. Also, contour plots of velocity magnitude showed similar values and structures for all models. What could be judged from observation, but not be quantified yet is the development of two major swirl structures, one in vertical axis where, flow velocities at the peripherals of the cloud chamber show negative axial values and positive values in the centre region. This is i.e. shown in **Figure 6.27**. The other rotational structure happens around the z-axis, which is i.e. illustrated in **Figure 6.21**.

However, it needs to be evaluated, how long the residence time of a snow crystal, built in the cloud chamber, is in reality. Residence time and vorticity magnitude are related closely, because the momentum of the rotational flow is responsible for keeping the ice crystals in the air. Since no cases were run applying gravity on one hand and discrete phase was neglected on the other hand, the built up model needs

to be evaluated by measurements. The momentum of an air particle is different to that of a water particle. In the cloud chamber, water particles, air, vapour and ice crystals are present. So mean flow field values in reality will be somewhere in-between an air-jet-driven and a water-jet-driven rotational flow.

Table 8.3: Characteristic flow and turbulence parameters

		Case I – cylindrical	Case II Standard k-ε	Case II Realizable k-ε	Case III
Max axial vorticity	[s^{-1}]	$1,4*10^4$	60	70	100
Av Velocity	[m/s]	3,4	2,6		0,9
Static pressure @outlet	[Pa]	$-8,5*10^{-2}$ - $4,26*10^{-3}$	$-7*10^{-2}$ - 10^{-3}		$-2*10^{-2}$ – $2*10^{-2}$
Min residence time	[s]	45	40	50	24,5

The complexity of the flow problem already exceeded prescribed efforts in the framework of a master thesis, mainly because of the components that should be represented in the grid. High aspect ratios were inevitable and the building of a grid adhering to quality thresholds while achieving an accurate grid at points of interest was coupled with a lot of effort. The implementation of heat transfer calculations, including ice nuclei generation and therefore phase change, was not possible under given conditions. Additionally, I do question the capability of the solver to cover the problem due to its high computational requirement and extent of the grid.

As during the empirical research, the poor heat transfer through the walls was observed, a further investigation of this issue was required. This could be executed by using the analogy to a cooling tower process where evaporative cooling is used. This process represents a really strong instrument for cooling activities, as latent heat energy is used for cooling as well. Analytical calculations could estimate required airflows in order to apply evaporative cooling. Conventional cooling towers operate in temperature ranges up to 80 K higher as the dendrite generator. This results in a disadvantage for the process of evaporative cooling in the cloud chamber as enthalpy curves of humid air flatten out in the negative temperature region, which means that for lower temperatures, a higher amount of air is required to transport the same amount of heat, compared to higher temperature levels. As cold air is available in almost infinite amounts at ambient conditions, the problem can be overcome easily.

9 Summary and outlook

The aim of this work was to build a 3D numerical model, picturing flow patterns and crystal spreading. The numerical model should be compared to the real-process picture. Within this work, an airflow model that estimates flow velocities in the cloud chamber, being introduced to it at transonic conditions could be achieved. The obtained solution is not verified by a comparison to real-life conditions yet. However, various solvers and turbulence models have been compared and an estimation of residence time, turbulence generation, and flow behaviour can be given.

Clearly, the influence of gravity, a discrete phase model via Lagrangian particle tracking [32], and phase changes up to crystal growth are of high interest. Within the expense of a master thesis, this was not doable yet. Nevertheless, the base for the development of such a model could be built.

In the next steps, an evaluation of the analytical heat transfer model will be made by air humidity and temperature measurements. Furthermore the airflow model will be adapted to the newly built geometry. As several water states are present in the cloud chamber and the influence of phase change and heat production to flow patterns and turbulence is not known yet, medium-independent velocity measurements will be applied in order to verify the airflow simulations. If results are far apart from what can be measured, a further development of the model including buoyancy and discrete phase modelling is necessary; or rather a different approach to a numerical model is needed.

However, field research will constantly be forwarded, different atomization techniques, cooling technique approaches and process geometries will be tested. The development of the numerical model was started, cooperating with CERN, where an enormous level of knowledge and computational power is on offer. For this work I could spend a time period of two months, working at the CERN institute. By investing more time, working in these surroundings, it is likely, that more outcomes will result from this cooperation. As framework conditions and technical possibilities are being developed constantly they might soon fit the requirements in a more favourable way, as numerical solvers and applied programs faced borders of their capacities with this model.

List of references

[1]   Worm, B.; Tourismus in Österreich. Trends und Herausforderungen in sechs Bausteinen für den Unterricht, Arbeitsgemeinschaft Wirtschaft und Schule (AWS) im Rahmen des Instituts für Bildungsforschung der Wirtschaft (ibw), 2014

[2]   Hahn, F.; Künstliche Beschneiung im Alpenraum – ein Hintergrundbericht. CIPRA Internationale Alpenschutzkommission, Schaan, 2004

[3]   Bacher, M., Burkart, J., Sokratov, S., Breiling, M.; Best, F., Harasek, M., Siegmann,T.; Schneekristallbildung in einer künstlichen Wolke zum Einsatz als Schneeerzeuger, Technische Universität Wien, Universität für Bodenkultur Wien, Wien, 2013

[4]   Breiling, M;, Bacher, M., Soktratov, S., Best,G.; Technische Universität Wien, Universität für Bodenkultur Wien, Verfahren und Vorrichtung zur Herstellung von künstlichem Schnee, 2015

[5]   ANSYS Inc. 2017; ://www.ansys.com/Products/Fluids/ANSYS-Fluent, 3.4. 2017

[6]   Trimble Inc; http://www.sketchup.com, 3.4.2017

[7]   Spraying Systems Co.; Catalogue 75-M-AA-Auto, Spraying Systems Co. Wheaton, IL, USA, 2013

[8]   Eisenberg, D., Kauzmann, W.; The structure and properties of water, Oxford University Press, 1969

[9]   Häußler, W.; Lufttechnische Berechnungen im Mollier-i,x-Diagramm, Verlag Theodor Steinkopff, Dresden, 1969

[10]   Lamb, D., Verlinde, J.; Physics and Chemistry of Clouds, Cambridge University Press, 2011

[11]   Wallace, J. M., Hobbs, P. V.; Atmospheric Science. Academic Press, 2 edition, 2006

[12]   Krauss, R.; Properties of Air. In VDI Heat Atlas, VDI-Verlag GmbH, Düsseldorf, 2010

[13]   Speedy, R. J.; Thermodynamic Properties of Supercooled Water at 1atm, Journal of Phys- ical Chemistry, 91:3354–3358, 1987

[14]   Tombari, E., Ferrari, C., Salvetti, G.; Heat capacity anomaly in a large sample of supercooled water. Chemical Physics Letters, 300:749–751, 1999

[15] Draxler, D.; Formation of ice nuclei from microscopic water droplets, Universität für Bodenkultur Wien, Wien, 2010

[16] Pruppacher, H., Klett, J.; Microphysics of Clouds and Precipitation, Springer, 1997

[17] Radhakrishnan, R., Trout, B.L.; Nucleation of Hexagonal Ice (I_h) in Liquid Water, J. Am. Chem.Soc., Vol 125, No 25, 7743-7747, 2003

[18] Koop,T., Beiping,L., Athanasios,T., Thomas,P.; Water activity as the determinant for homogeneous ice nucleation in aqueous solutions, Swiss Federal Institute of Technology, Letters to nature, Germany, 2000

[19] Mullin, J. W.; Crystallization, Elsevier Butterworth-Heinemann, Oxford, 2001

[20] Federer, B.; Über den Einfluss der Oberflächeneigenschaften von Halbleitern auf ihre Eiskeimfähigkeit, Z. Angew. Math. Phys., (1968)

[21] Welti, A., Zamin,A.K.; Exploring the Mechanisms of Ice Nucleation on Kaolinite: From Nucleation to Condensation Freezing, Journal of the Atmospheric Sciences, Volume 71, 2013

[22] Ansmann, A. and Coauthors; Influence of Saharan dust on cloud glaciation in southern Morocco during the Saharan Mineral Dust Experiment. J. Geophys. Res., 2008

[23] Fukuta, N.; A study of the mechanisms of contact ice nucleation, J. Atmos. Sci., 1975

[24] Cooper, W.; A possible mechanism for contact nucleation, J. Atmos. Sci., 1974

[25] Pant, A., Parsons, M. T., Bertram, A. K.; J. Phys. Chem. A, 2006, 110, 8701–8709

[26] Parsons, M. T., Riffell, J. L., Bertram, A. K.; J. Phys. Chem. A, 2006, 110, 8108–8115

[27] Bayvel, L., Orzechowski, Z.; Liquid Atomization, CRC Press, 1993

[28]]Movahednejad, E., Ommi, F., Hosseinalipour, M.; Prediction of Droplet Size and Velocity Distribution in Droplet Formation Region of Liquid Spray, Entropy, 12, 1484-1498, 2010

[29] Rayleigh, J. W. S.; On the Instability of Jets, Proc. London Math. Soc., 10, 4,1878

[30] Dongqing Li Prof.; Encyclopedia of Microfluidics and Nanofluidics, 2185, Springer, 2008

[31] Kuhlmann, H. C.; Strömungsmechanik, Pearson Studium, München, Germany, 2007

[32] Baker, D.; Shryock, H.; A comprehensive approach to the analysis of cooling tower performance, Thermal Science, 2012

[33] Menter R.; Two-Equation Eddy-Viscosity Turbulence Models for Engineering Applications, AIAA Journal, 32(8), 1598–1605, 1994

[34] Szymczyk, J.A.; Zielke, P.; Vorlesungsskript zur Strömungstechnik, Stralsund, 2008

[35] Cengel, Y.; Boles, M.; Thermodynamics: An Engineering Approach, Mcgraw-Hill College, 4th edition, 2001

[36] Wu,J.-Z., Xiong,A.-K., Yang,Y.-T.; Axial stretching and vortex definition, Physics of Fluids, 2005

[37] Acheson, D.J.; Elementary Fluid Dynamics, Oxford Applied Mathematics and Computer Science Series, Clarendon Press, 1990

[38] Shawn C., Shadden, F., Lekien, J., Marsden, E.; Definition and properties of Lagrangian coherent structures from finite-time Lyapunov exponents in two-dimensional aperiodic flows, Physica D 212, 2005

[39] K. C. Young. Microphysical Processes in Clouds. Oxford University Press, 1993.

[40] Fluent Inc.; ANSYS FLUENT Theory Guide, Lebanon, 2013/11

[41] MIT; Marine Hydrodynamics, MIT - Department of Hydrodynamics, 2011

[42] McCormack, P.; Vortex, Molecular Spin and Nanovorticity – An Introduction, Springer, 2012

[43] Gupta, A. K., Lilley, D. G., Syred, N.; Swirl flows, Abacus Press, 1984

[44] Holmén, V.; Methods for Vortex Identification, PhD Thesis, Lund University, Sweden, 2012

[45] Haller, J.; An objective definition of a vortex, J. Fluid Mech. vol. 525, 2005

[46] Hunt, J.C.R., Wray, A.A., Moin P.; Eddies, stream, and convergence zones in turbulent flows, Center for Turbulence Research Report CTR-S88, 1988

[47] Chong, M. S., Perry, A. E., Cantwell, B. J.; A general classification of three-dimensional flow fields, Phys. Fluids, A 1, 1990

[48] Ferziger, J. H., Peric, M.; Numerische Strömungsmechanik, Springer-Verlag, Berlin, 2008

[49] Chorin, A. J.; Numerical solution of navier-stokes equations, Mathematics of Computation, 22:745–762, 1968

[50] Fluent Inc.; ANSYS FLUENT User's Guide, Fluent Inc., Lebanon, 2006/09

[51] Merkel, F.; Verdunstungskühlung, VDI Forschungsarbeiten No. 275, Berlin, 1925

[52] Batchelor, G.K.; An Introduction to Fluid Dynamics Cambridge, University Press, 1967

Appendix

A   Construction drawings
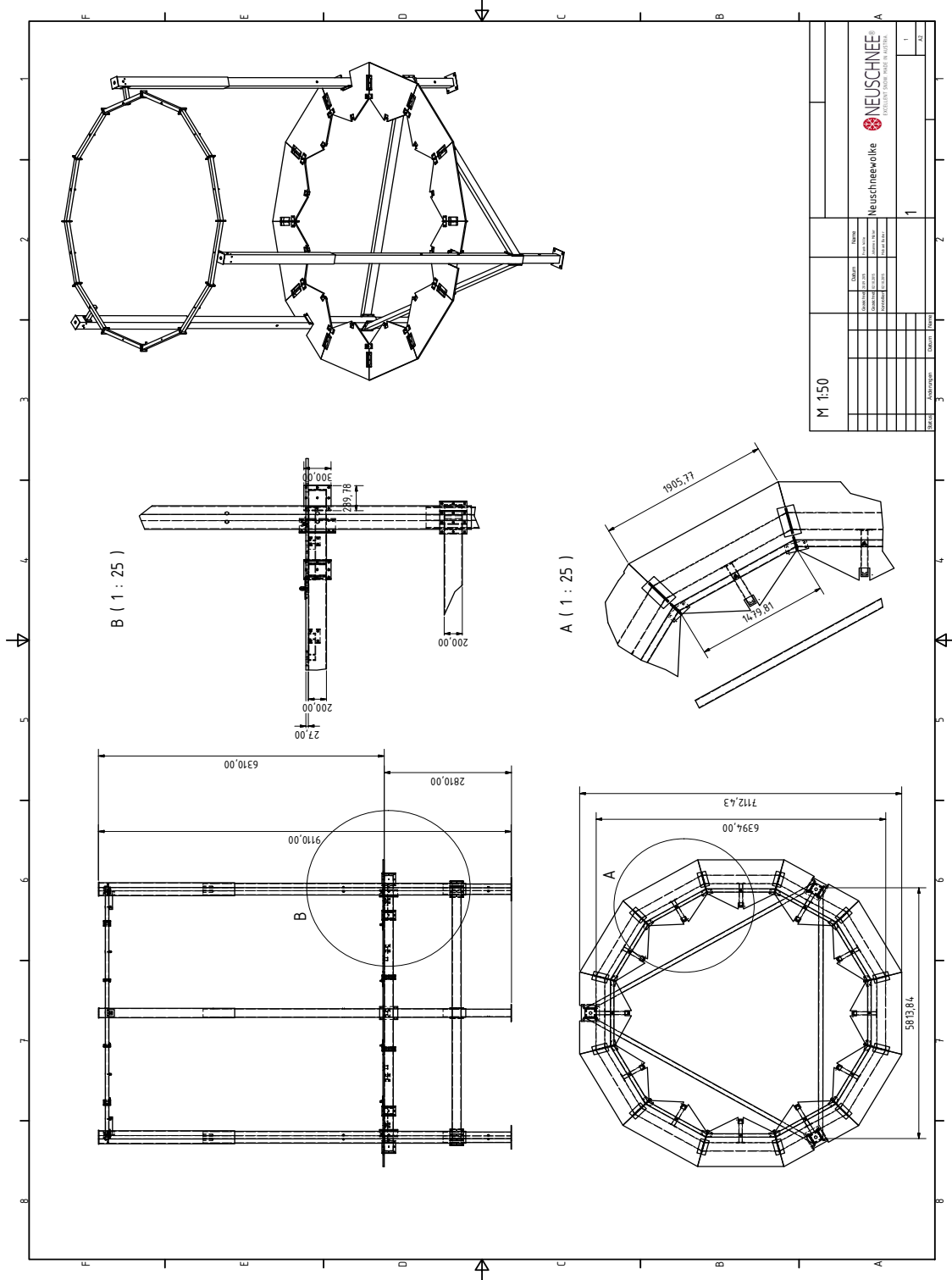
Figure A.1 Construction drawings © Neuschnee GmbH

B Nozzle representation

Jet properties – manufacturer data

For the introduction of water and air into the cloud chamber nozzles are used, which are provided by Spraying Systems Co. [7]
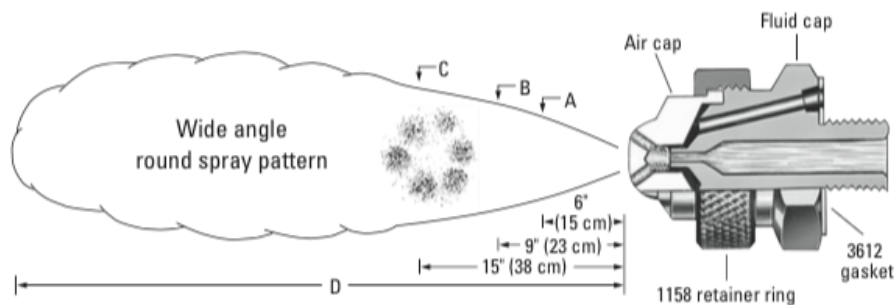
Figure B.1: Jet and spray cross section [7]

The nozzles, used in this application, are so called atomizing nozzles, applying an internal mixture process. As illustrated in **Figure B.1**, the nozzles consist of an air cap and a fluid cap, which are screwed to the main body of the nozzle. Water and air can therefore be introduced to the nozzle separately. Inlets are realized via pressure ports. Atomization of water happens inside the cavity between the air cap and the fluid cap, wherefrom water particles and air are pouring out of the nozzle. Ejection of the mixture happens through the orifices of the air cap. **Figure B.2** shows the shape of the so-called wide angle round spray air caps. The six orifices are arranged around a half-sphere symmetrically. Orifices are orientated within an angle of 35° with respect to the overlapping symmetry line of the sphere and the orifice orientation. This generates the flow pattern, shown in **Figure B.1.**

Figure B.2: "Wide angle round spray" air cap [7]

By varying water and air pressure, mass flows, spray dimensions but also droplet sizes are being changed. For the application in the cloud chamber, three different sizes of this jet composition are used. The following table exemplarily shows applied operating points and varying spray dimensions for the jets:

Table B.1: Operating Points of applied nozzles [7]

Jet label	Water pressure [bar]	Air pressure [bar]	Water [l/h]	Air [l/min]	A [cm]	B [cm]	C [cm]	D [m]
SU16	4	3,9	7,8	36	19	23	30	4
	3	3	6,4	30	16	20	26	2,7
SU26B	4	4,1	23	122	21	28	37	5,9
	3	3,2	15,1	109	20	26	34	4,1
	2	2,1	15,1	76	19	25	33	3,2
SU26	4	3,9	52	101	20	28	39	6,8
	3	3,2	33	99	20	28	38	5
	2	2,4	18,9	89	20	27	37	4,1

The given data gives an idea about spray characteristics. In order to achieve more detailed information on flow characteristics and in reference to the approach of this work, there is little information, which can be used, unfortunately. Nozzle geometry and mass flow amounts are, however, useful and purchase fundamental information for the application of the analytical tools. Manufacturer data of the applied nozzles is shown in **Table B.1**.

Turbulence

Different nozzle geometries and outpouring conditions also imply different conditions of turbulence. The Reynolds number will be used as a dimensionless index for turbulence. Its calculation is inevitable, evaluating turbulence treatment of a flow condition. It measures the ratio between inertial and viscous forces. The Reynolds number is defined as follows [29]:

$$Re = \frac{\rho v d_0}{\nu} = \frac{inertial\ force\ per\ mass}{viscous\ force\ per\ mass} \qquad (\text{B-1})$$

Executed calculations apply geometries and conditions at the nozzle exit.

Table B.2: Reynolds-number estimation nozzle exit

SU26/SU26B		
Calculated velocity @ nozzle exit	308,26	m/s
Characteristic length	0,0008	m
kinematic viscosity of air	$1,71*10^{-5}$	Pa*s
Reynolds number	14400	

SU16		
Calculated velocity @ nozzle exit	308,26	m/s
Characteristic length	0,0004	m
Kinematic viscosity of air	$1,711^{-5}$	Pa*s
Reynolds number	7210	

Measurements

This part of the present work is addressed to the empirical measurements, which should give evaluable results, in order to be compared with outcomes of theoretical calculations.

Declared aim of those measurements is to find out, whether flow can be treated as compressible or incompressible. This fact can be determined by relating it to the phenomenon of choked flow (See Chapter 2.2.3), which can be determined analytically. This involves the flattening of the curve, shown in Figure 2.10 at a certain point, according to formulae for compressible flow (2-21) - (2-24).
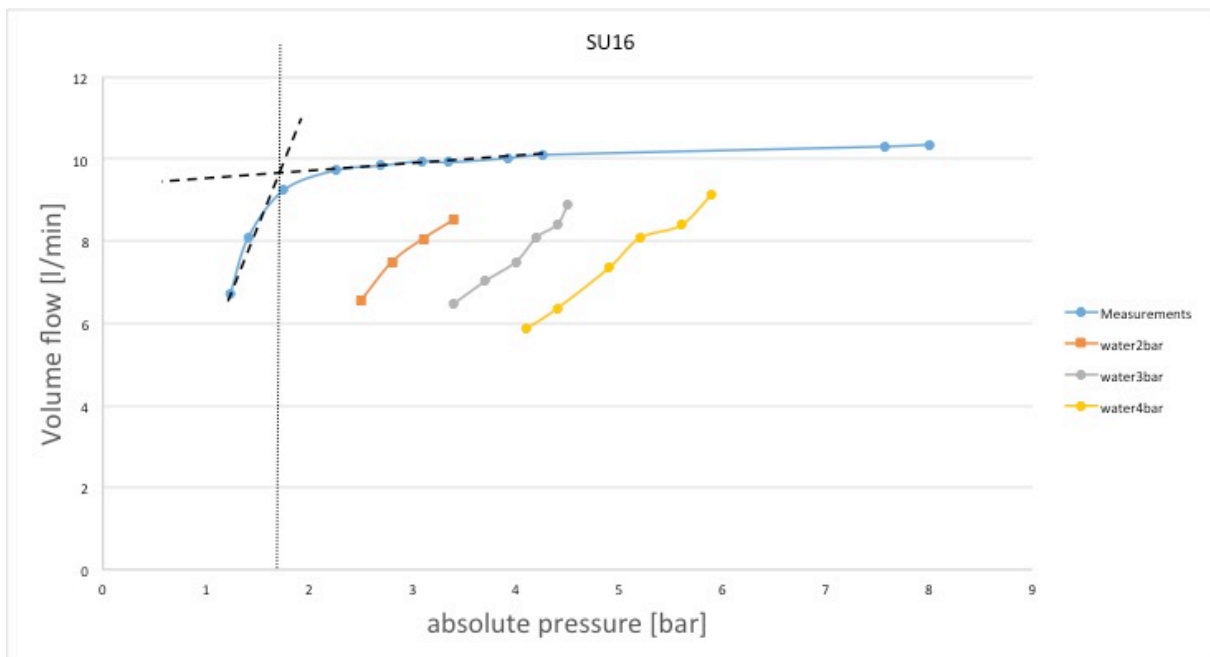
Figure B.3: SU16 Measurements
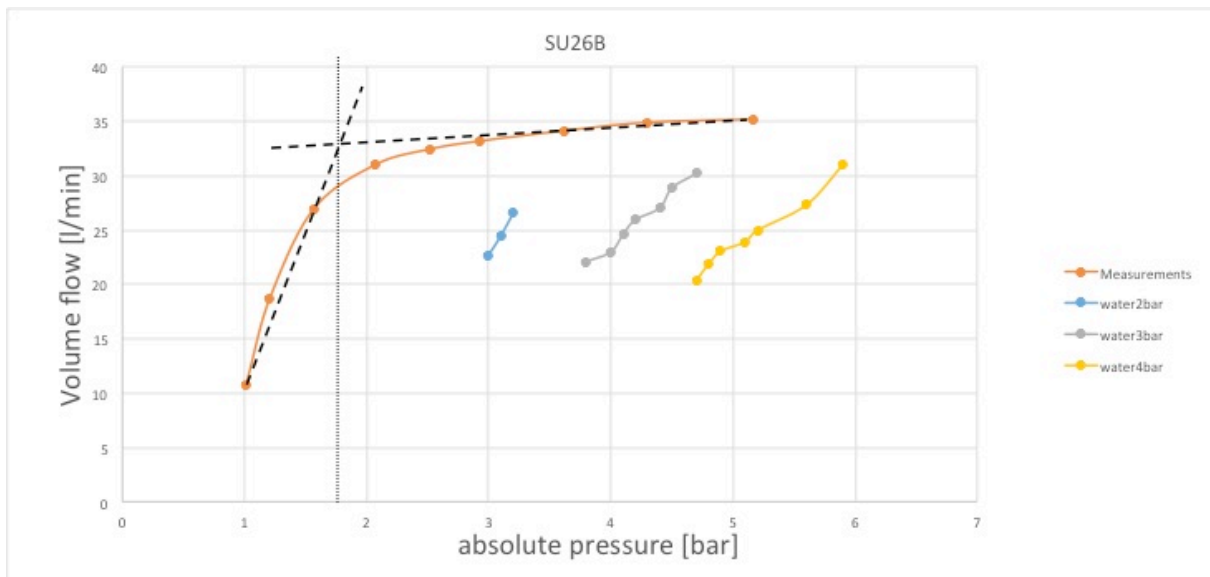
Figure B.4: SU26B Measurement graph and manufacturer data [7]

As the aperture of the nozzle outlet, representing the smallest cross section and therefore a relevant value for calculations of comparison, is exactly the same for models SU26 and SU26B, only the latter is being measured.

Curves of measurement do show the expected behaviour for choking flow condition, although theoretical correlations and measurement results differentiate by losses, which occur within real conditions. In order to define an approximate point, which can be compared with choked flow condition, linear slopes of approximation are implemented. An estimated pressure drop of Δp=1,8 is a good correlation to critical values, mentioned in **Table B.2**.

Operating conditions are between 2 bar and 4 bar air pressure. Those values are above critical pressure values for choked flow, which leads to the conclusion that choked flow and therefore sonic velocity occurs at the jet outlets.

Standard litres are corrected to litres, applying a reference temperature of 21 °C. Used data sheets refer to two-phase flows of constant water pressure, so water – air volume relations vary for applied operating points, and explain linear behaviour of the curves. In order to illustrate this fact, **Figure B.5**, is used :
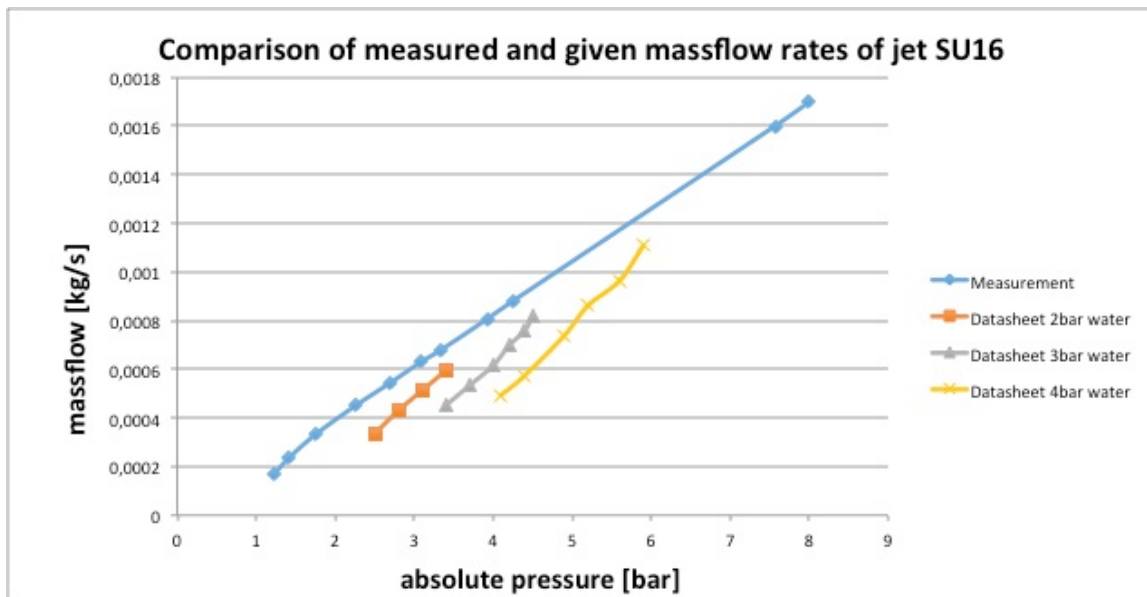
Figure B.5 massflow vs. pressure measurement graph and manufacturer data [7]

Looking at the continuity equation (B-2), one can see, that density and the area, through which the fluid is passing, are related to the mass flow. This could explain the higher gradient of manufacturer data curves compared to the measurement curves. On the other hand **Figure B.5** illustrates, that volume flow cannot increase as fast in two-phase conditions as it does in the single-phase flow case. Using

$$\dot{Q} = \frac{\dot{m}}{\rho} = A \cdot u = const \qquad \text{(B-2)}$$

shows the reasonability.

Conclusion

It has been shown that at applied operation points, conditions for airflow through the jets are transonic to supersonic**. Figure B.3** and **Figure B.4** show transition from subsonic to sonic flow at pressure ratio values of approximately 1,8, which corresponds well to critical values for isentropic relations and therefore to compressible ideal gas theory. Knowing this, it is obvious, that in Fluent an adequate solver for compressible conditions needs to be applied. Reynolds number calculations for applied conditions at the nozzle exit show numbers of turbulent flow. This means that a suiting turbulence model needs to be chosen in order to represent turbulence, present at the nozzle exit.

C Convergence monitoring Case I

Conic case
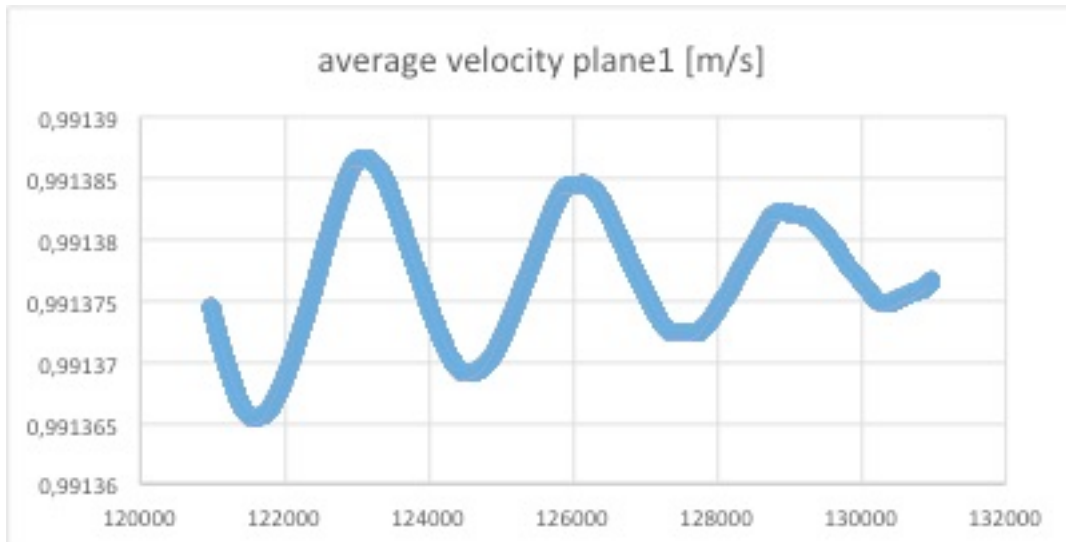
Figure C.1: velocity /iterations velocity plane1
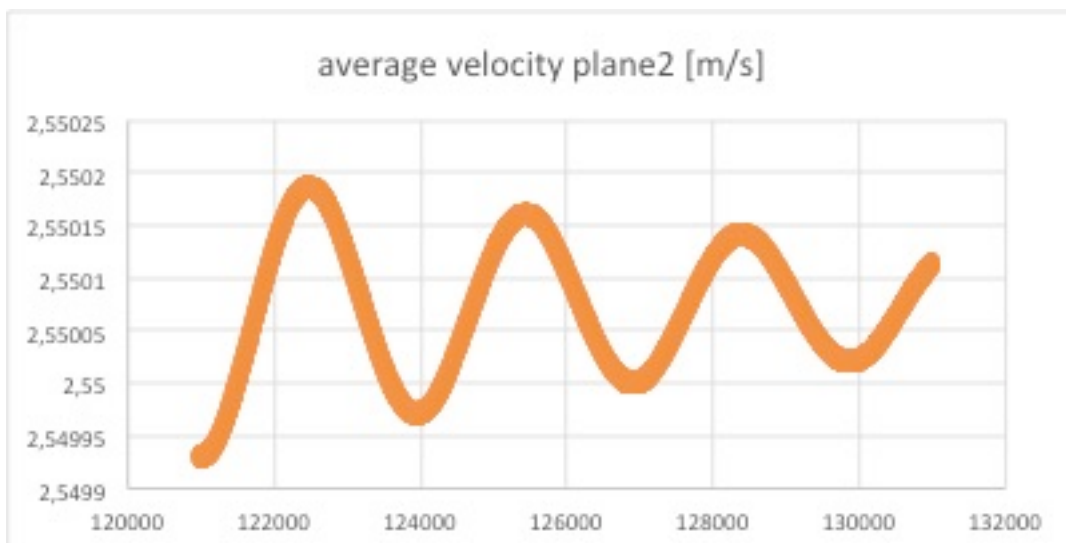
Figure C.2: velocity /iterations velocity plane2
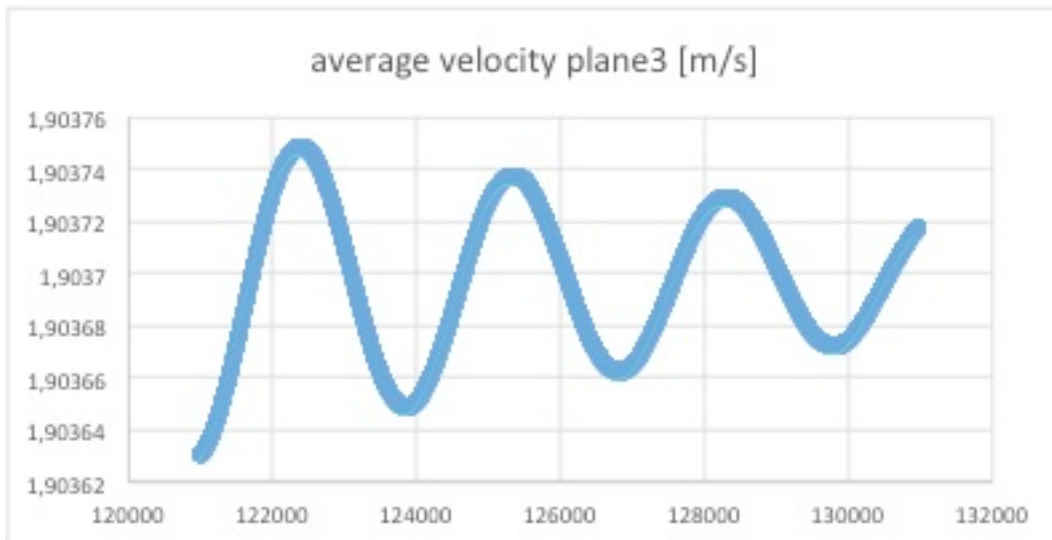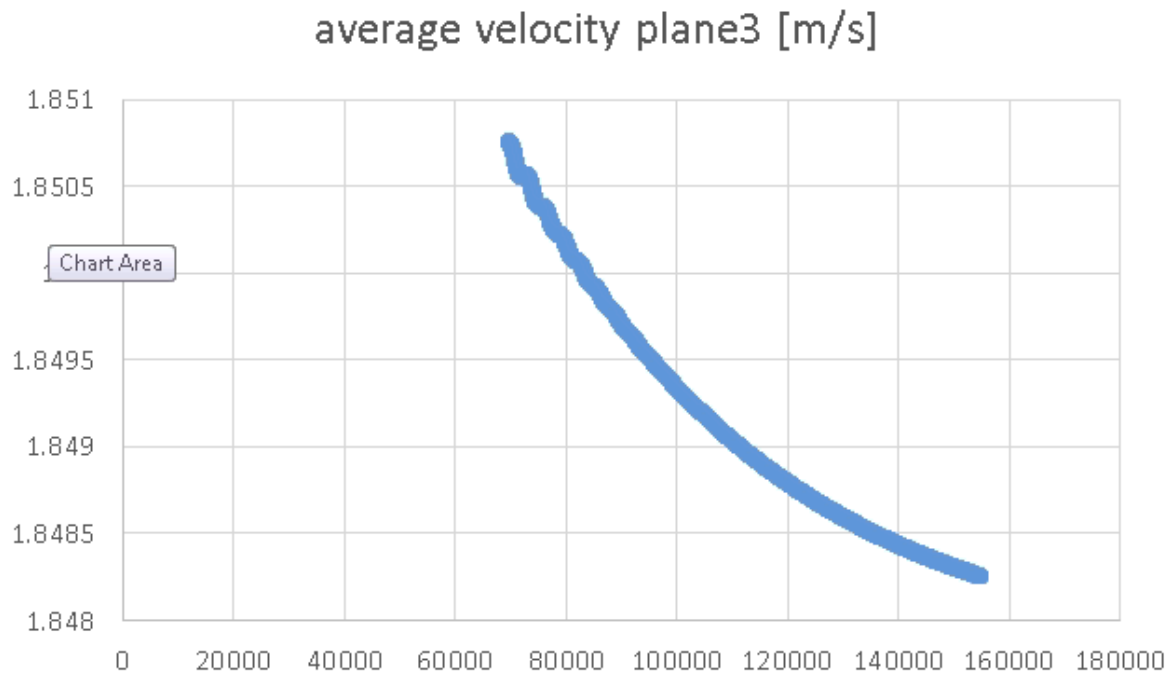
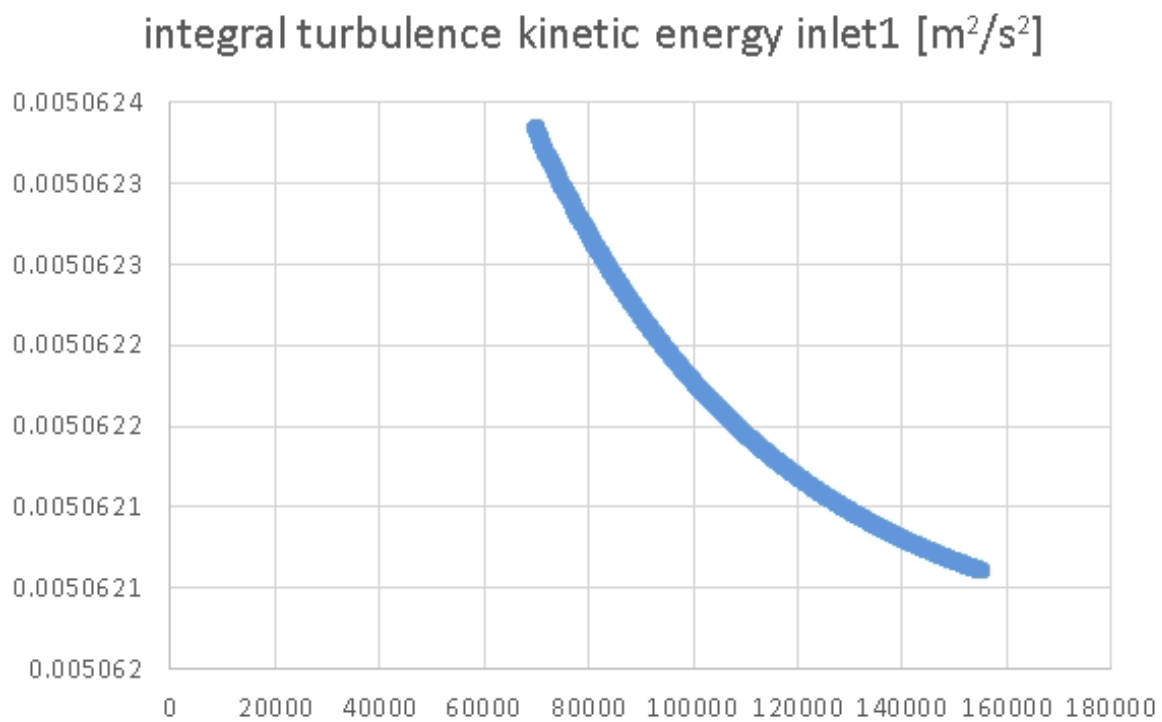**Figure C.3:** velocity /iterations velocity plane3
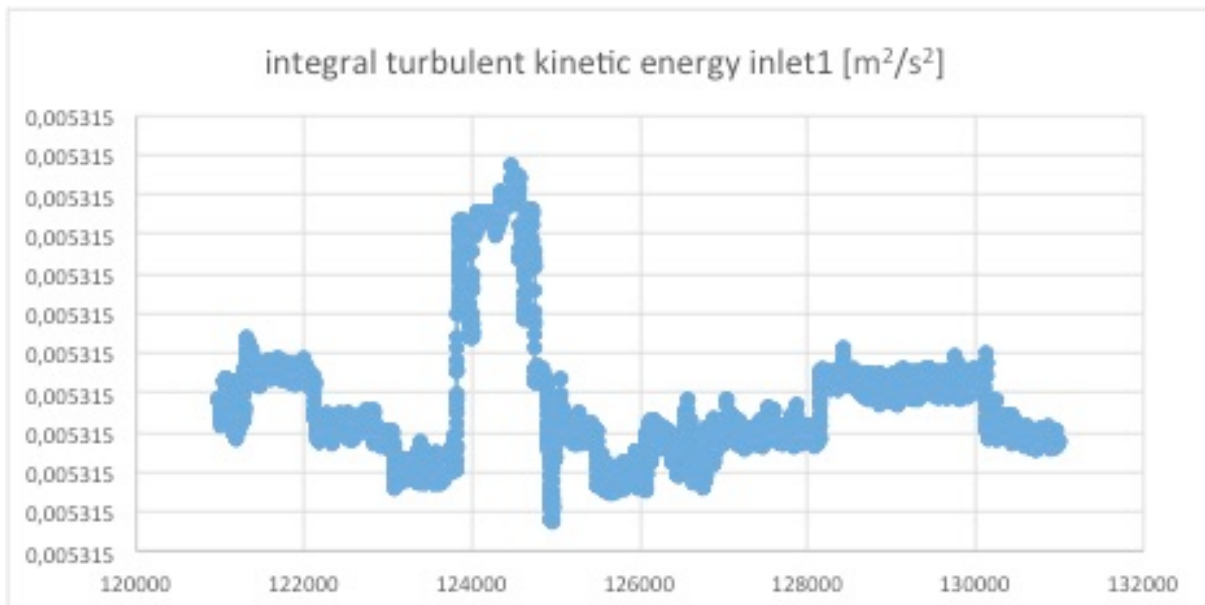
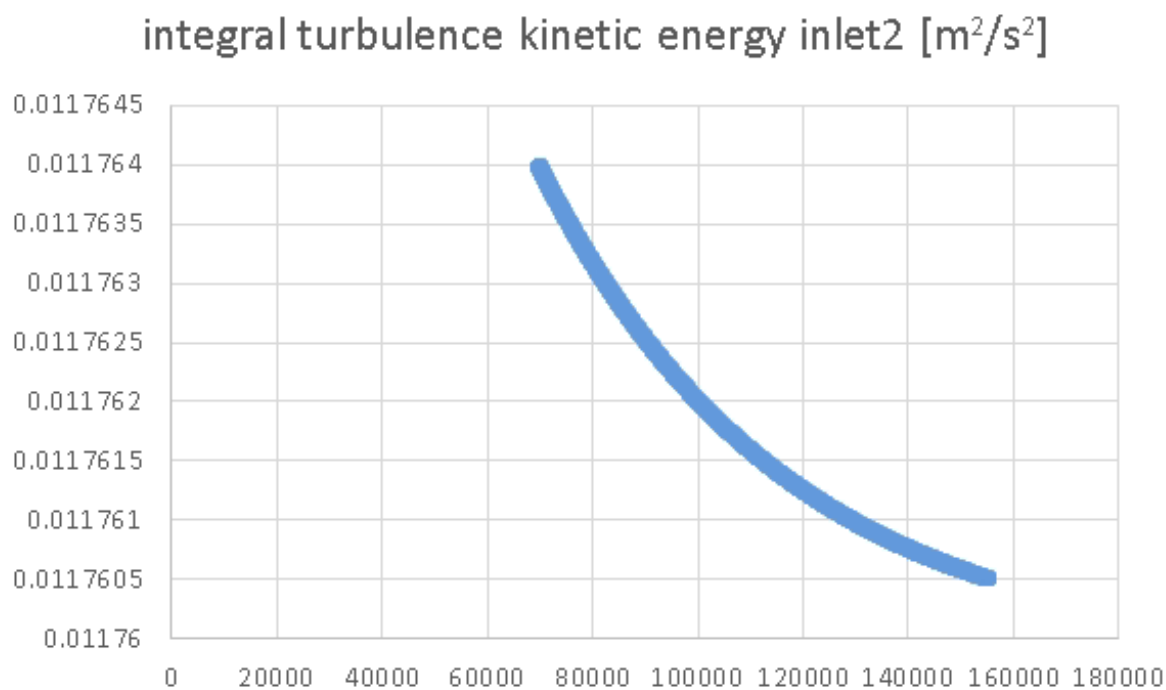**Figure C.4:** integral turbulent kinetic energy /iterations inlet 1
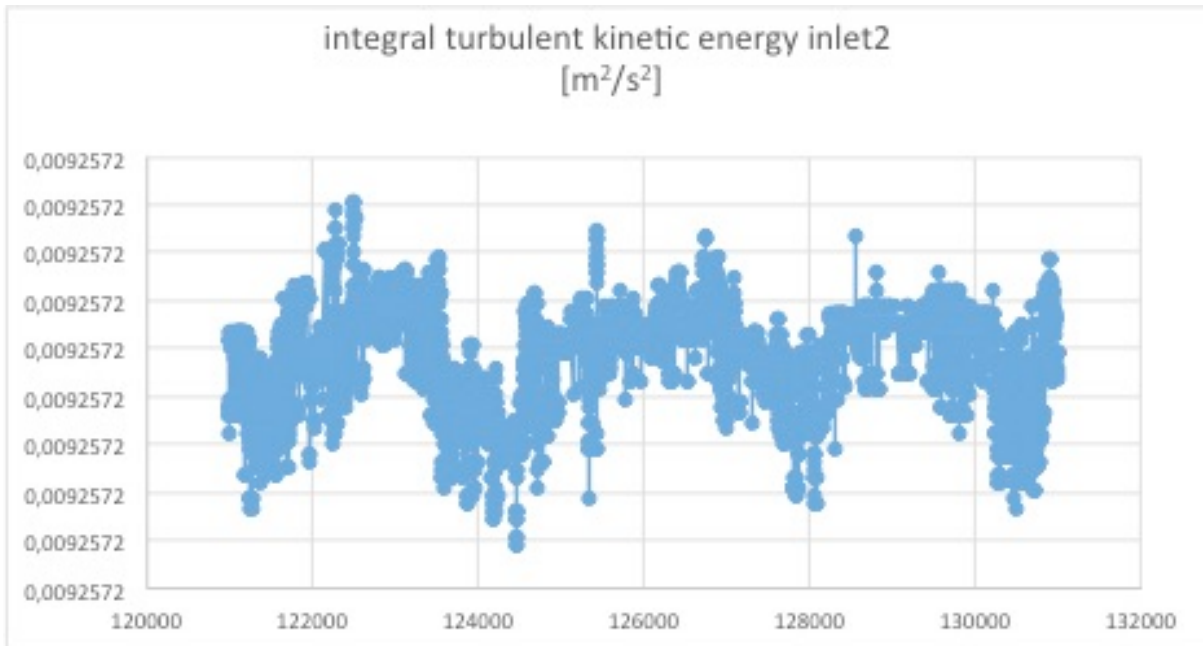
Figure C.5: integral turbulent kinetic energy /iterations inlet 2
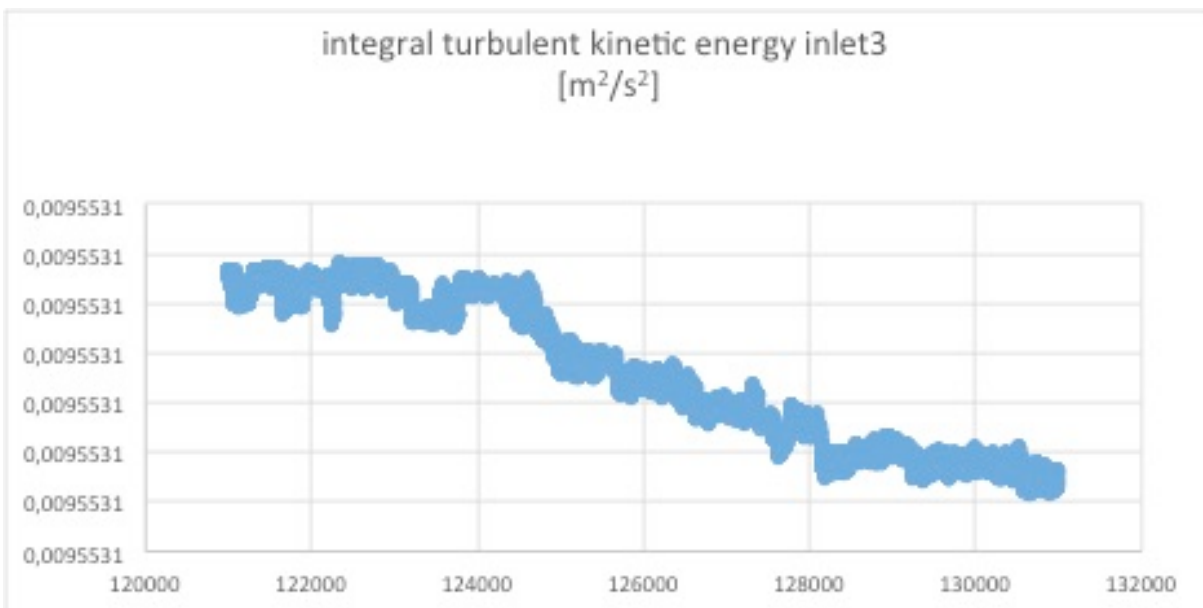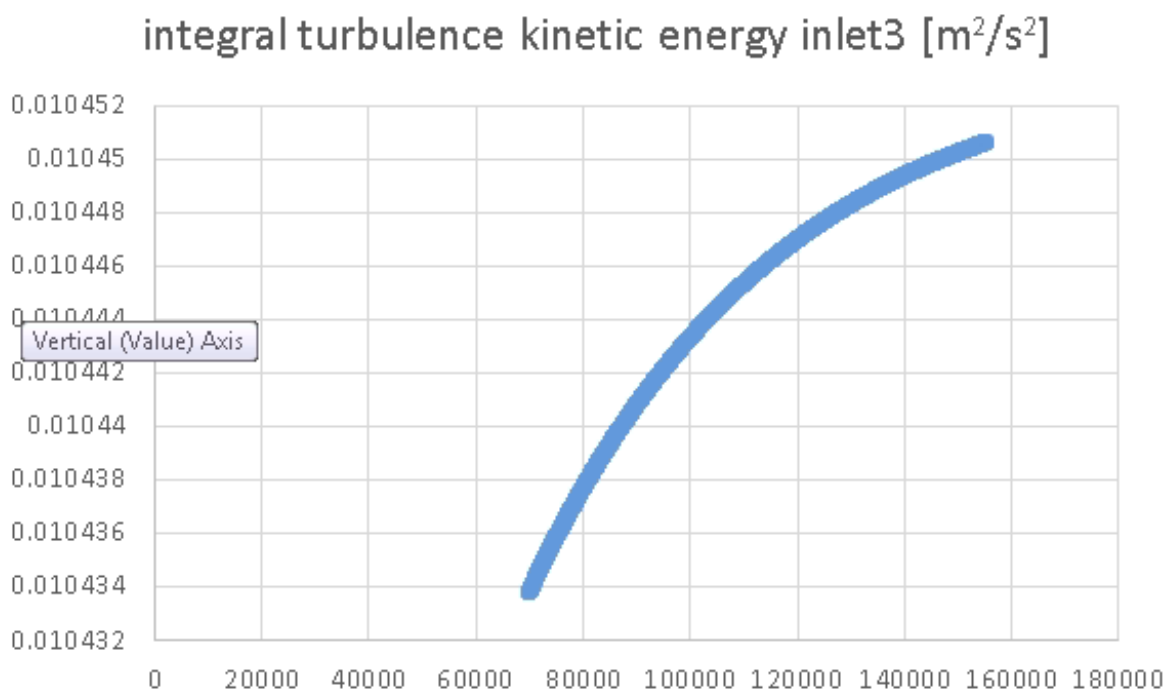

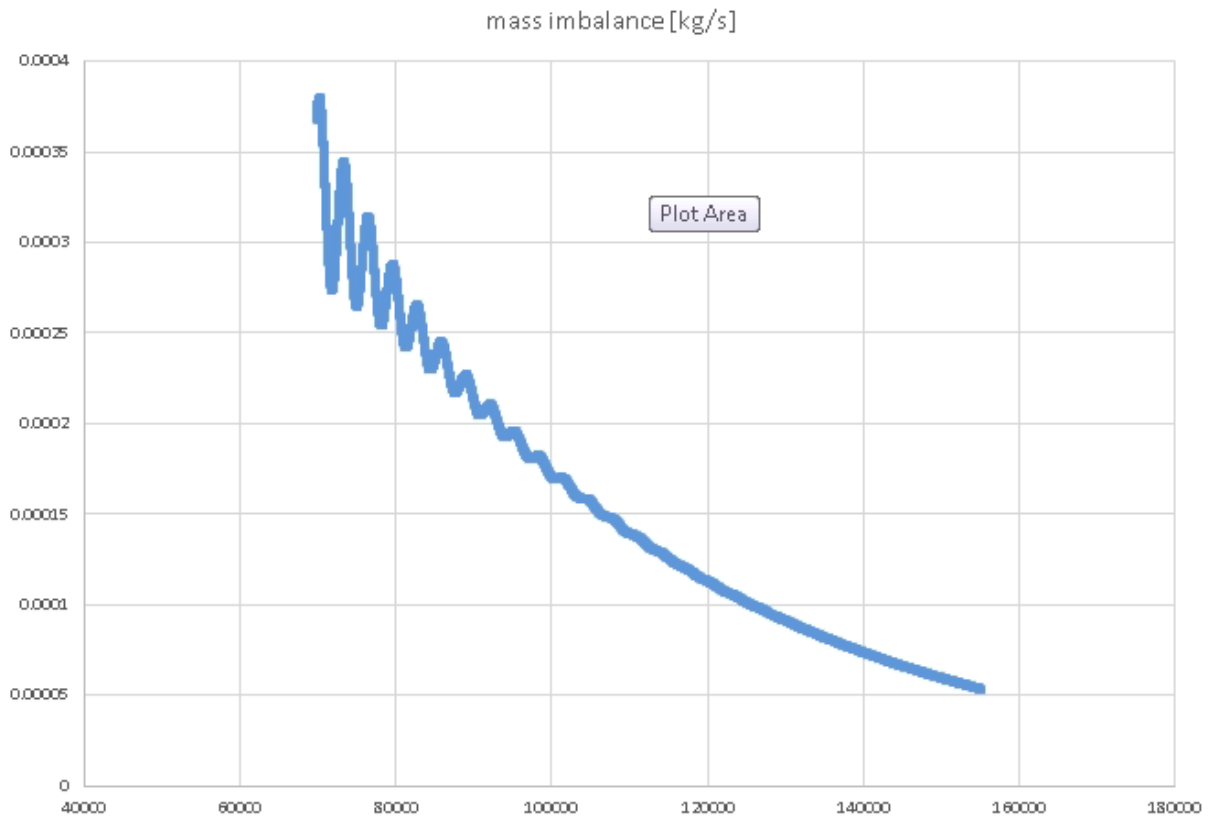**Figure C.6:** integral turbulent kinetic energy /iterations inlet 3
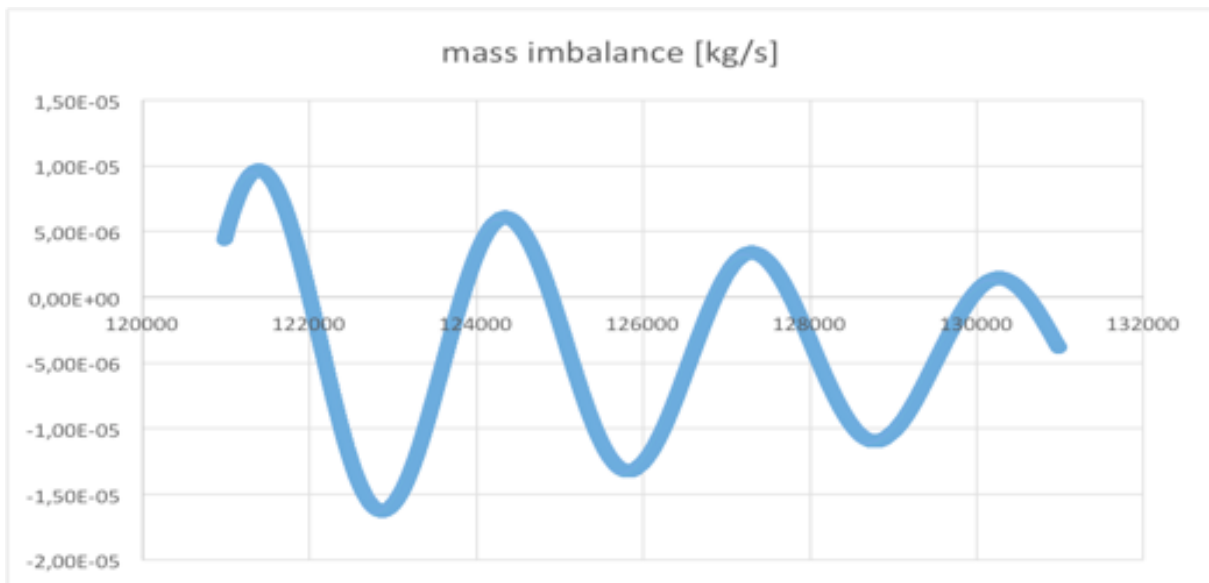
Figure C.7: mass imbalance/iterations

Cylindrical case
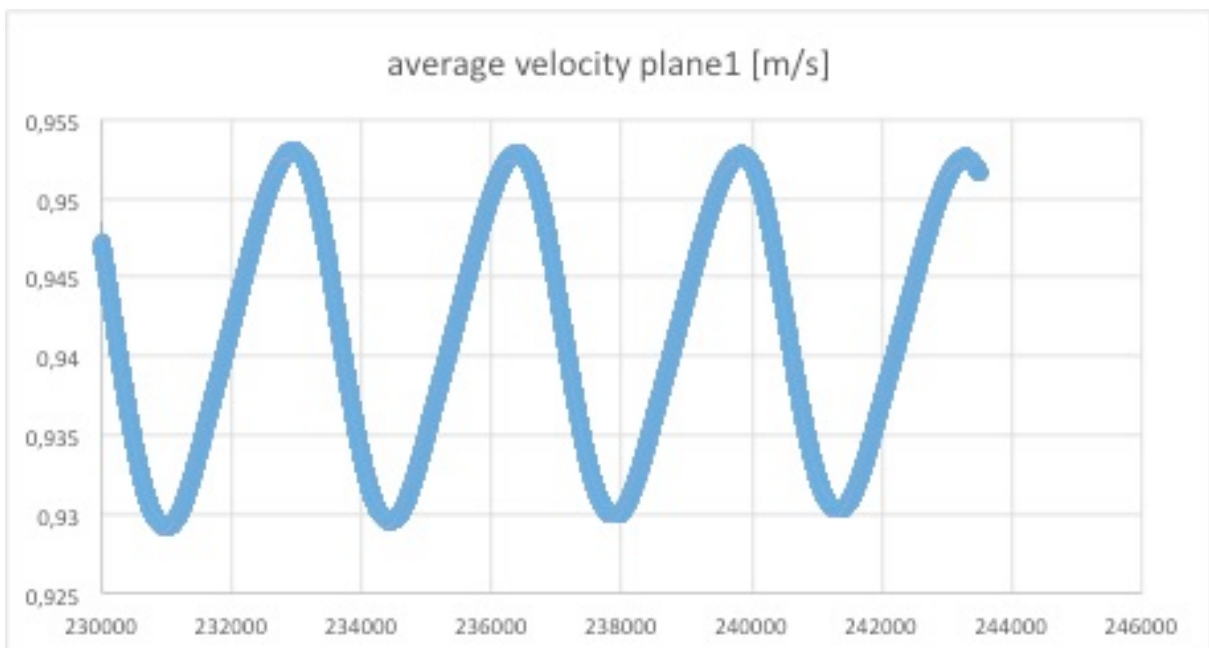
Figure C.8: velocity /iterations velocity plane1
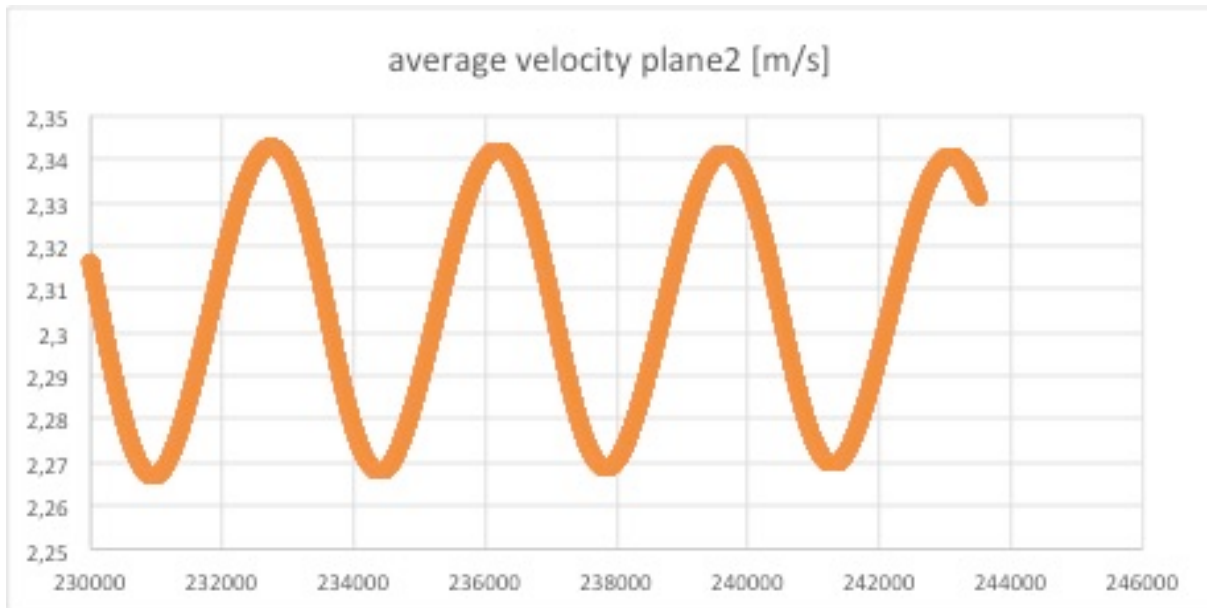
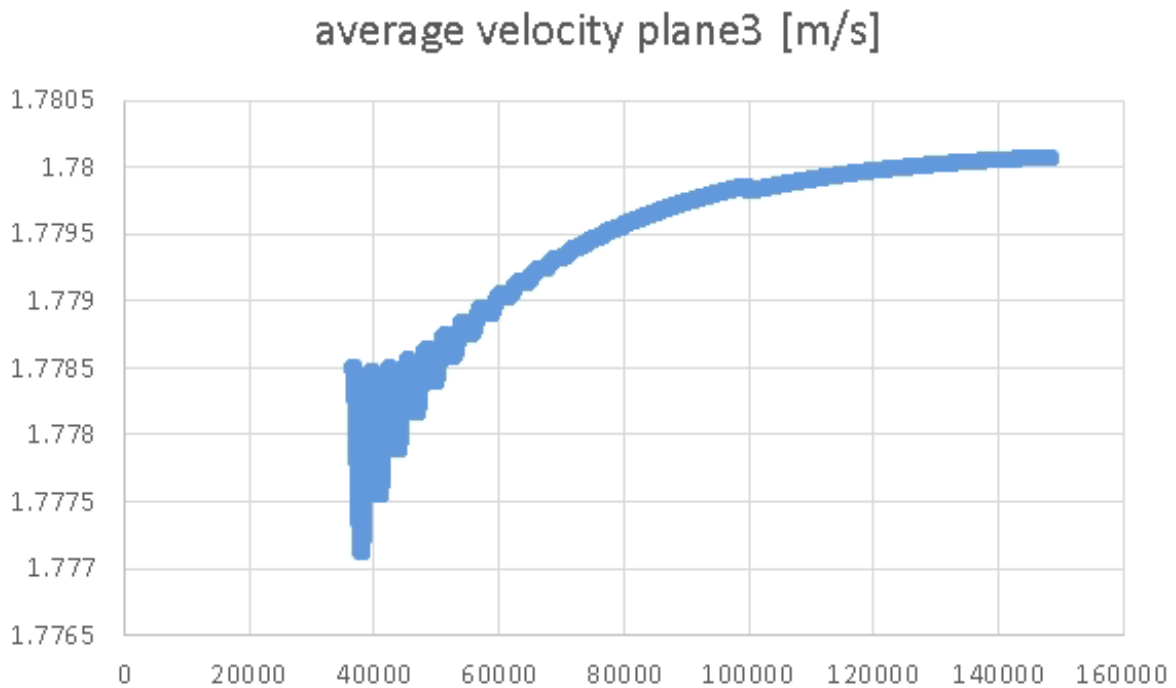**Figure C.9:** velocity /iterations velocity plane 2
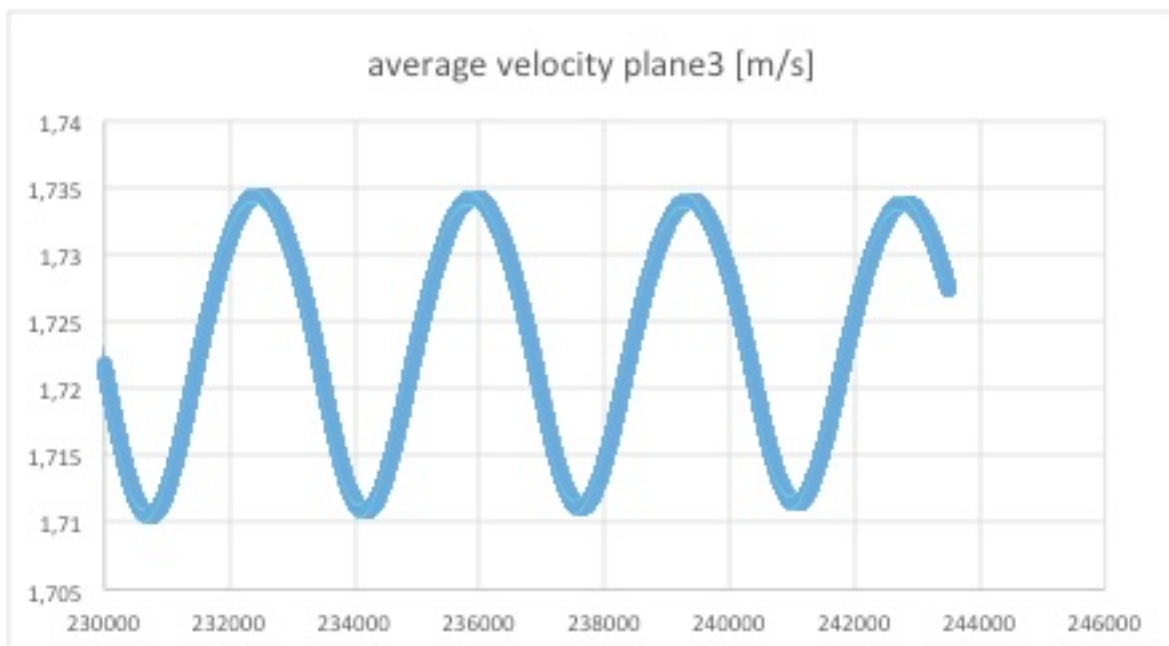
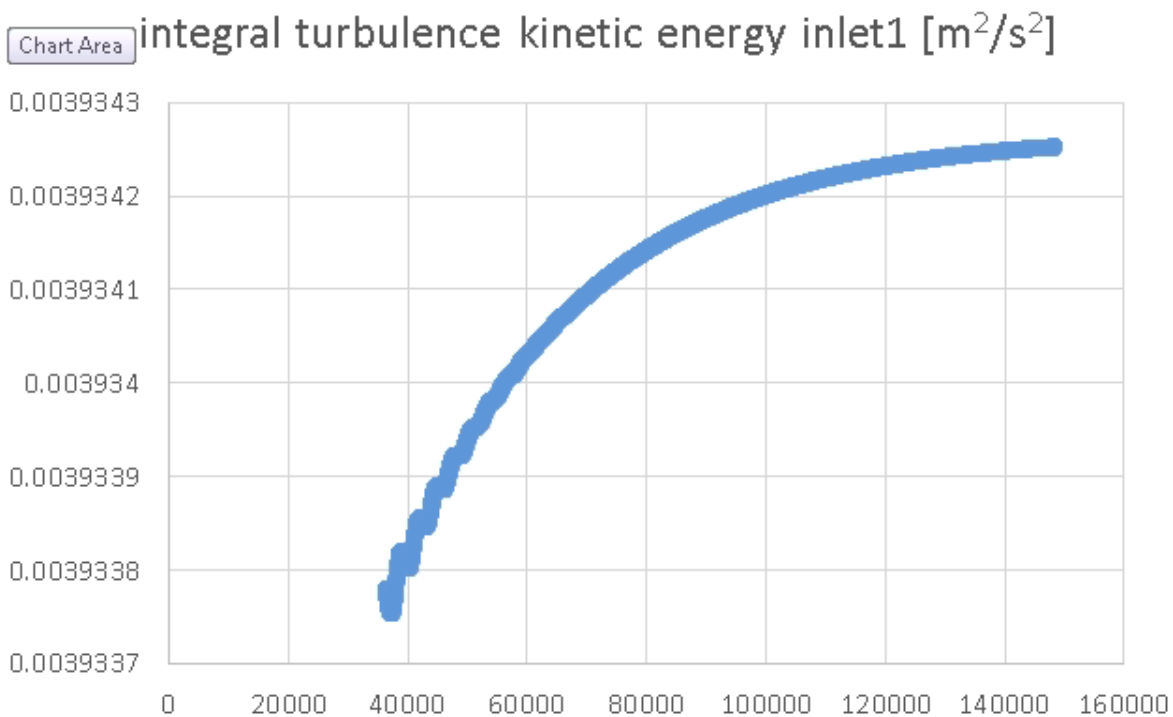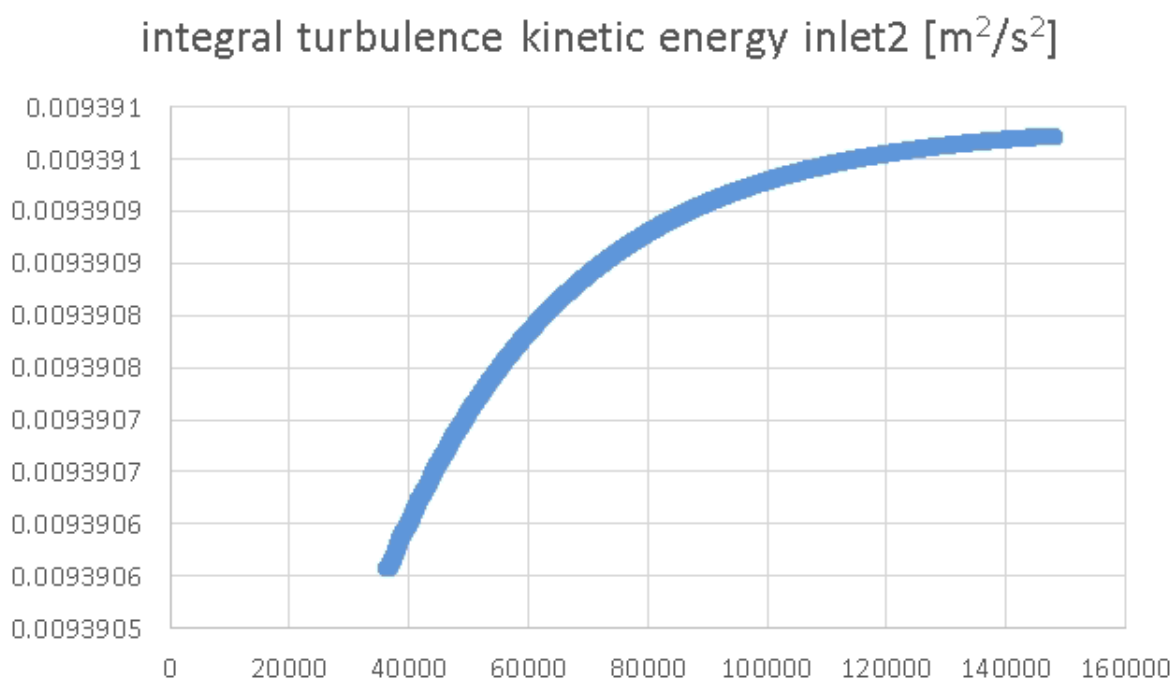**Figure C.10:** velocity /iterations velocity plane 3
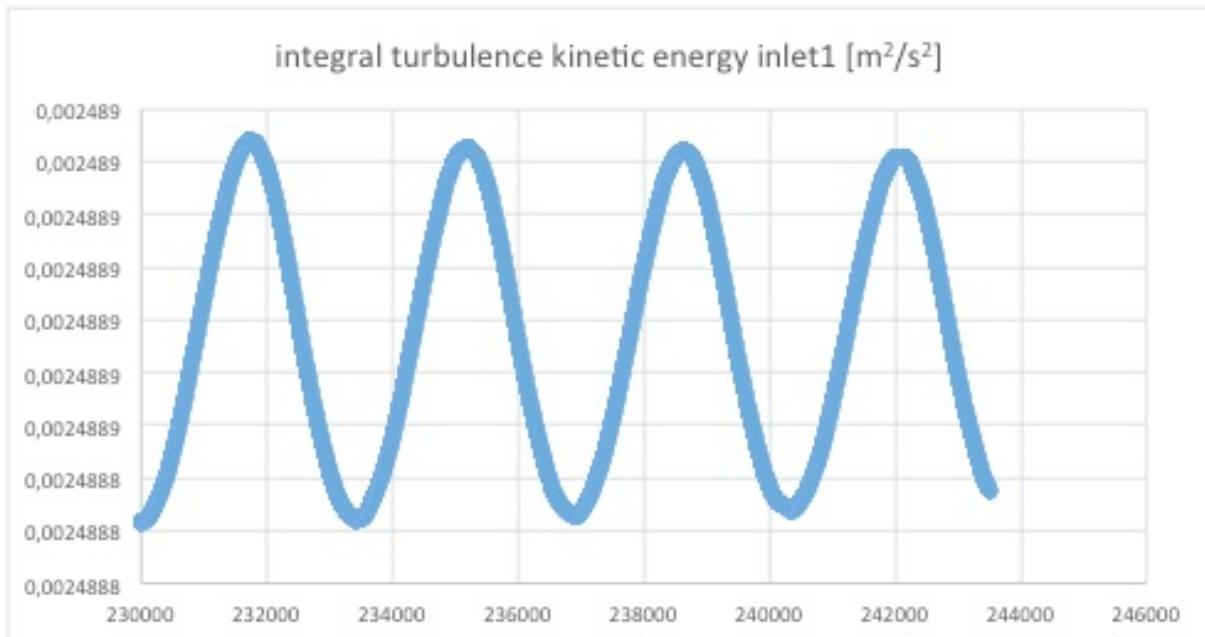
Figure C.11: integral turbulent kinetic energy /iterations inlet 1
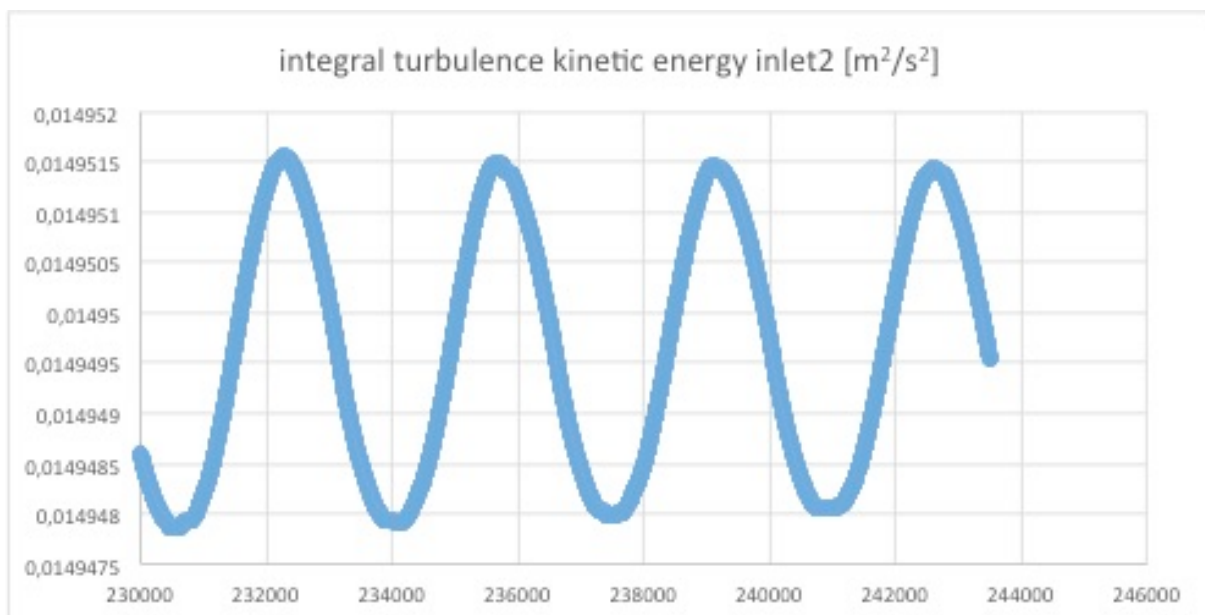
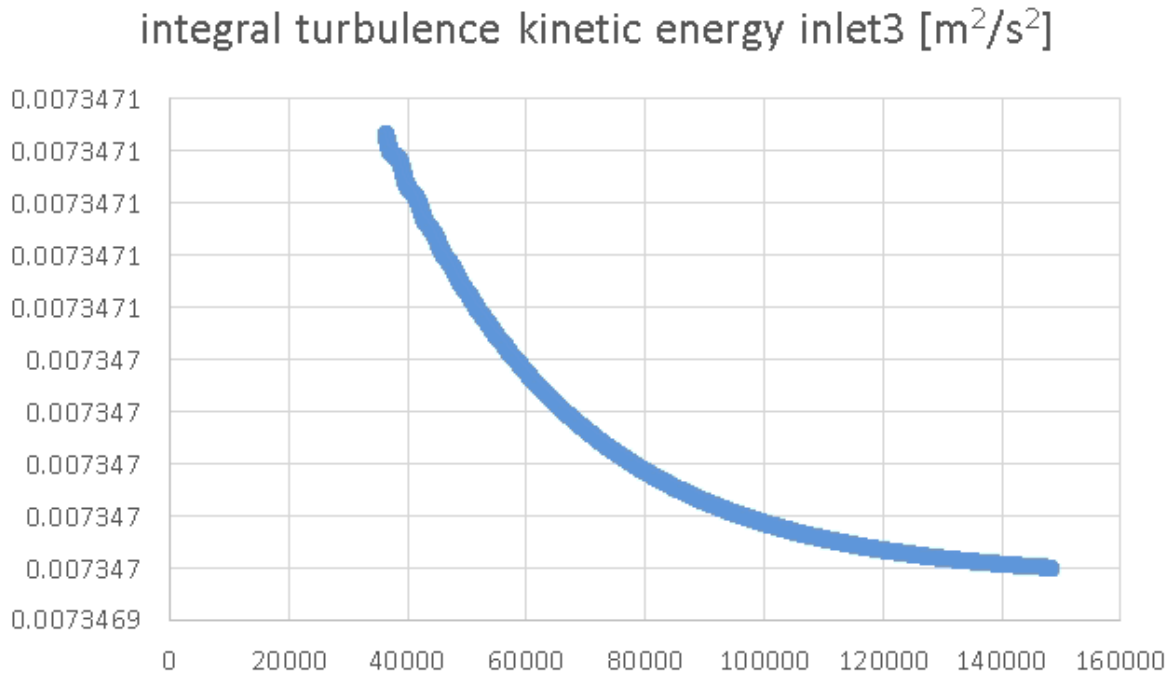**Figure C.12:** integral turbulent kinetic energy /iterations inlet 2
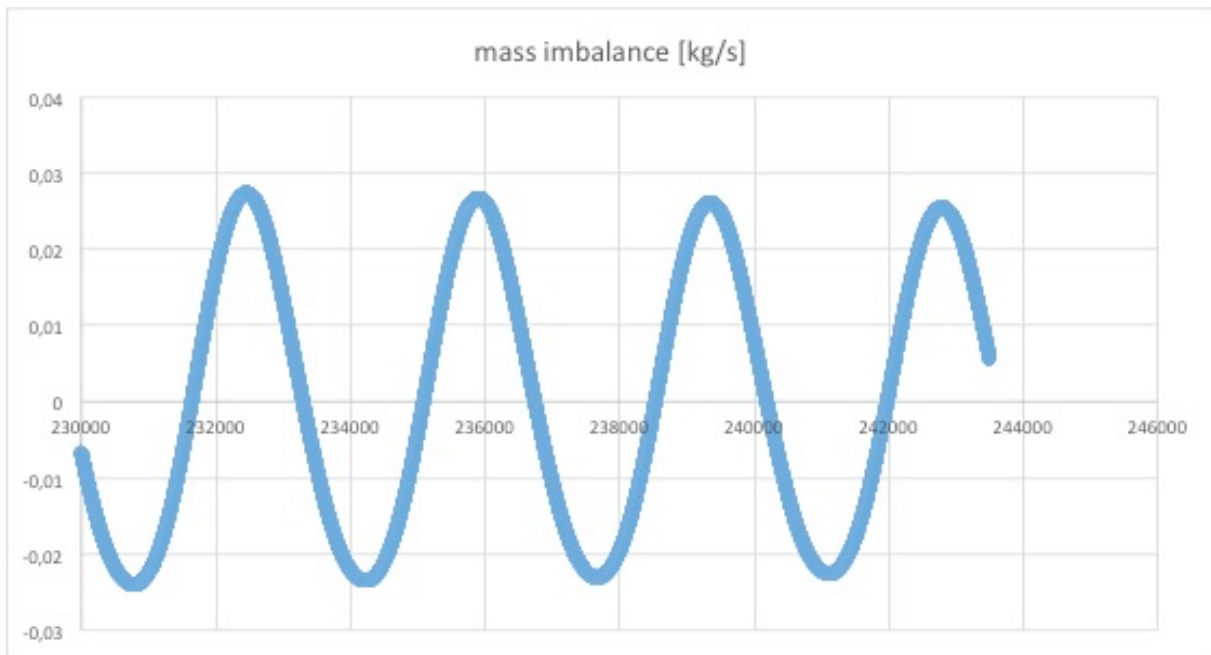
Figure C.13: mass imbalance /iterations

1

4

2

5

3
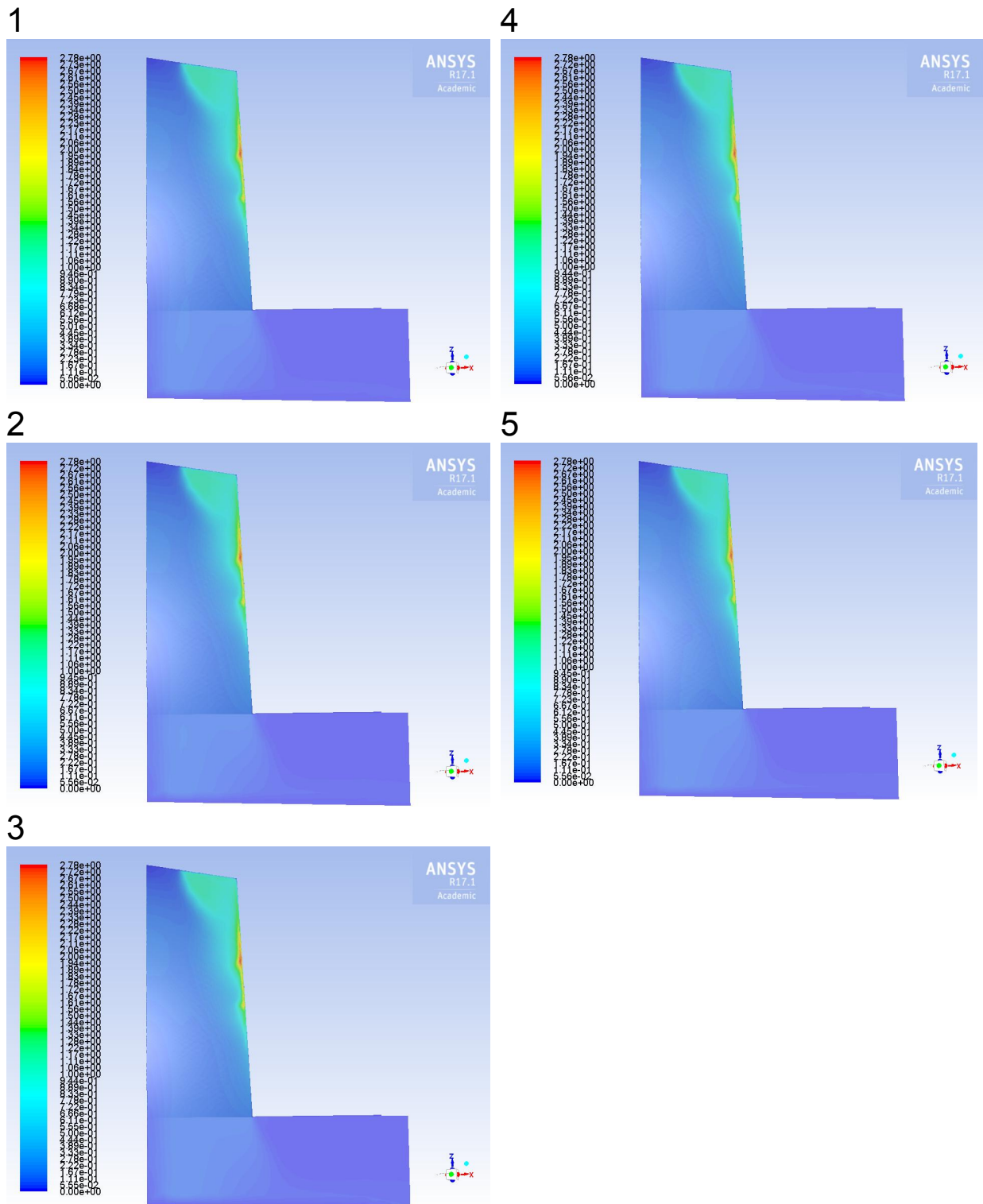
Figure C.14: Velocity magnitude @ periodic plane during one periodic residual fluctuation of 2000 iterations from 1-4 in augmenting iteration steps
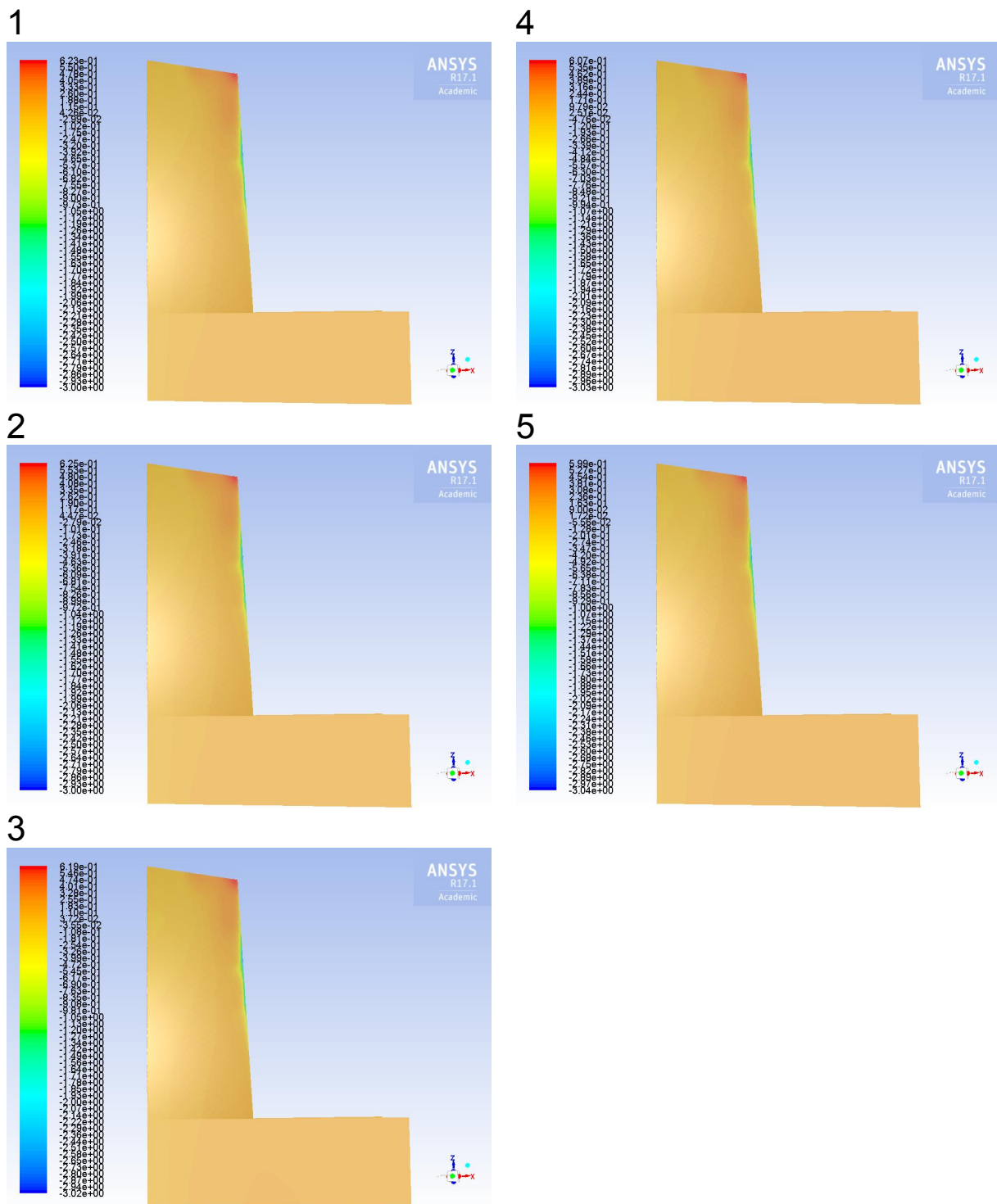
Figure C.15: Axial velocities @ periodic plane during one periodic residual fluctuation of 2000 iterations from 1-4 in augmenting iteration steps
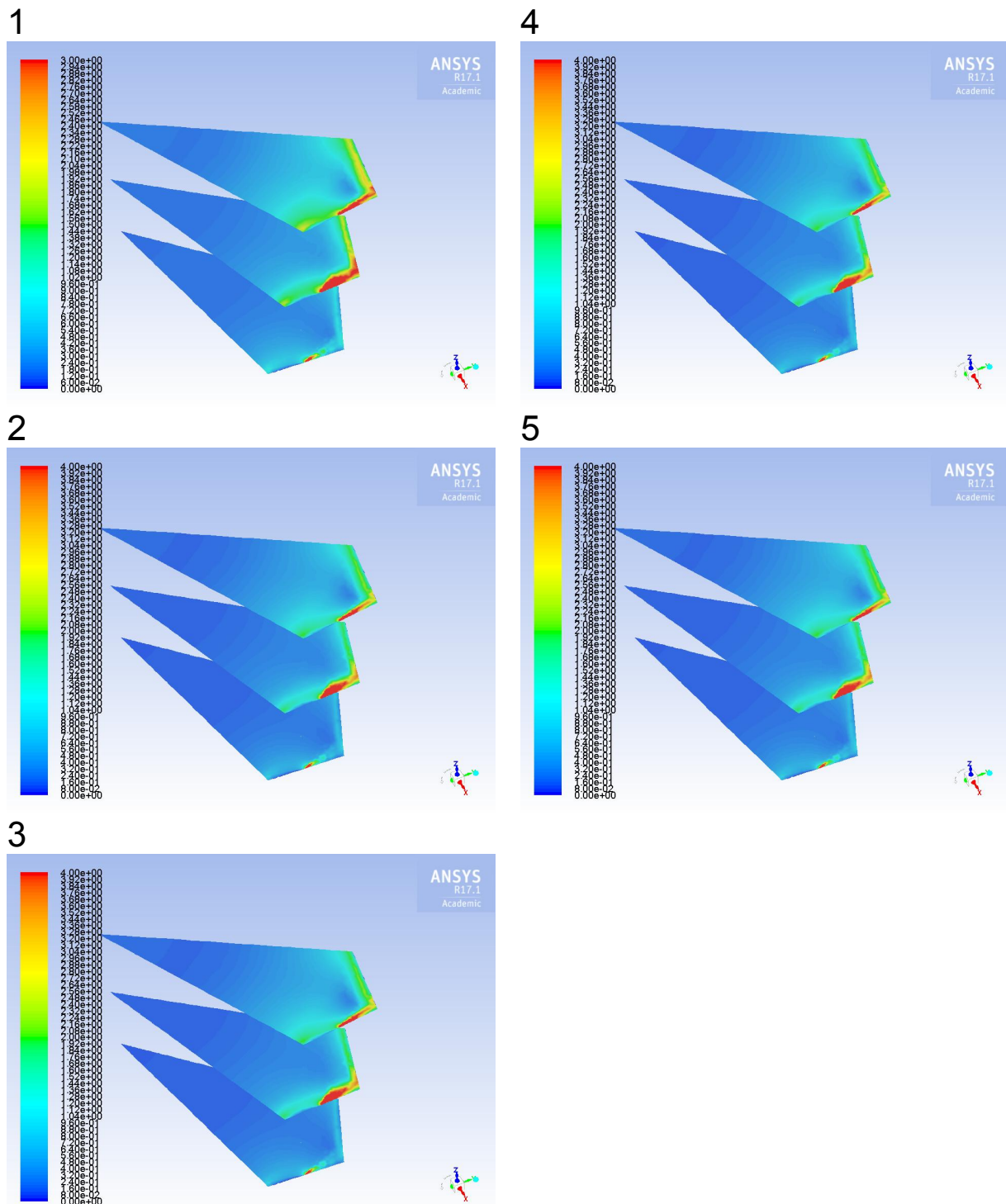
Figure C.16 Velocity magnitude @ veloplanes during one periodic residual fluctuation of 2000 iterations from 1-4 in augmenting iteration steps

D   Convergence monitoring Case II

Standard k- ε turbulence model
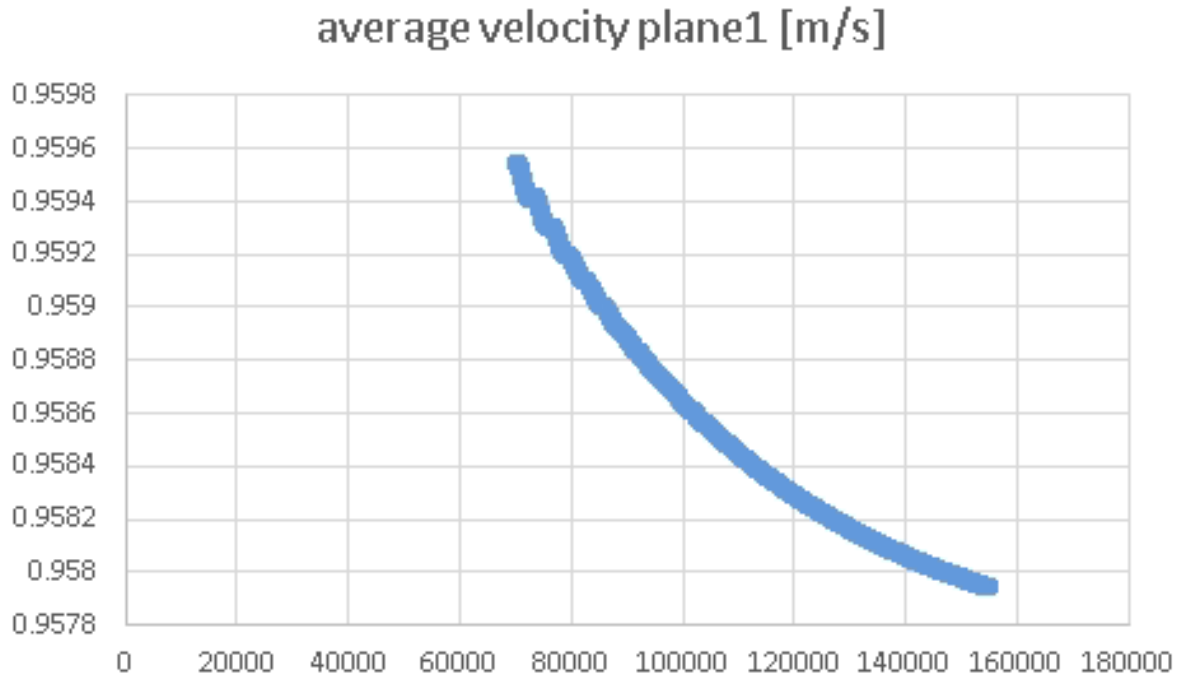
Figure D.1: velocity/iterations veloplane 1
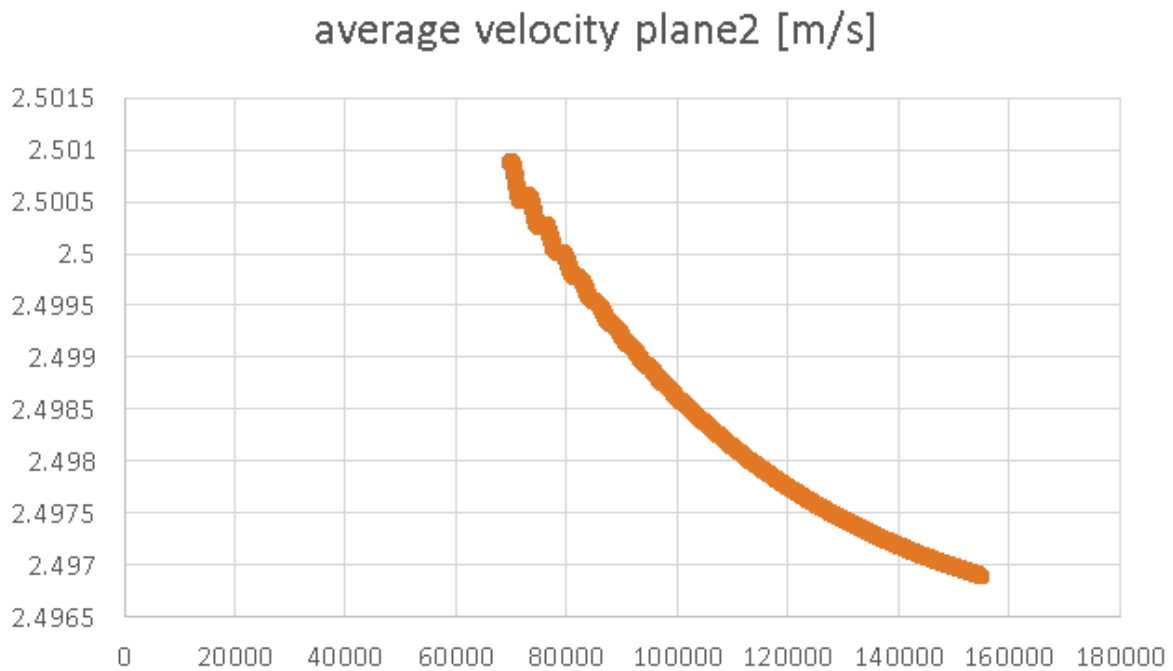
Figure D.2: velocity/iterations veloplane 2

Figure D.3: velocity/iterations veloplane 3

Figure D.4: integral turbulent kinetic energy/iterations inlet 1

integral turbulence kinetic energy inlet2 [m^2/s^2]

Figure D.5: integral turbulent kinetic energy/iterations inlet 2

integral turbulence kinetic energy inlet3 [m^2/s^2]

Figure D.6: integral turbulent kinetic energy/iterations inlet 3

Figure D.7: mass imbalanace/iterations

Realizable k-ε turbulence model
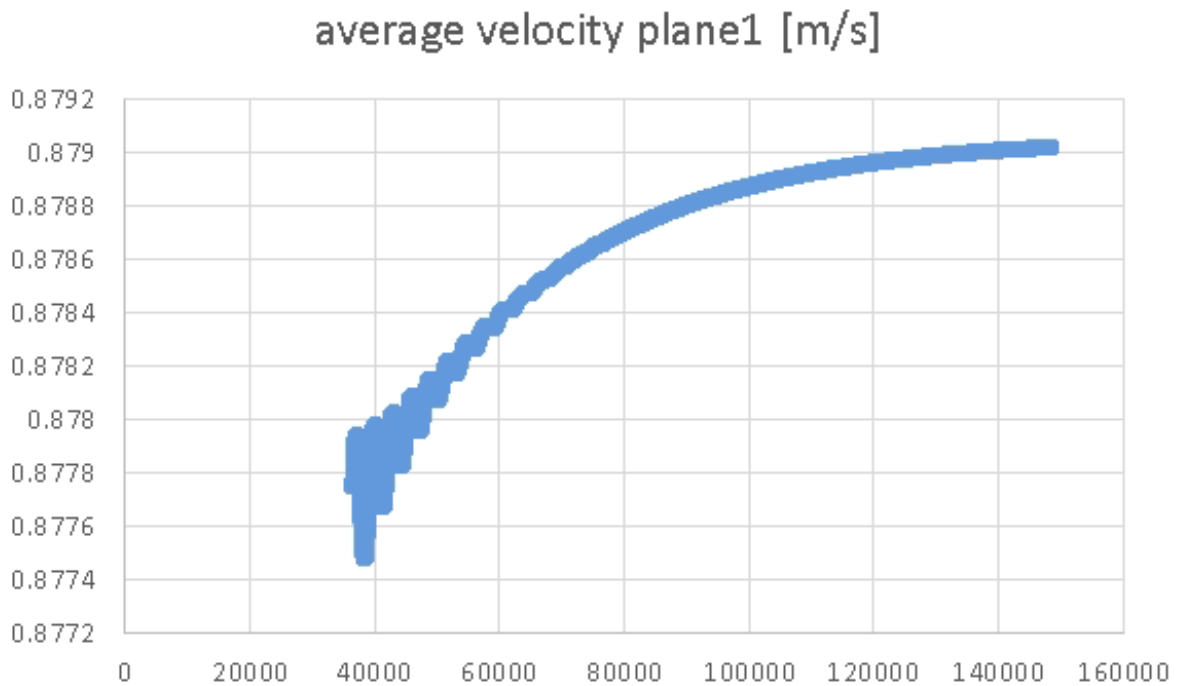
Figure D.8: velocity/iterations veloplane 1
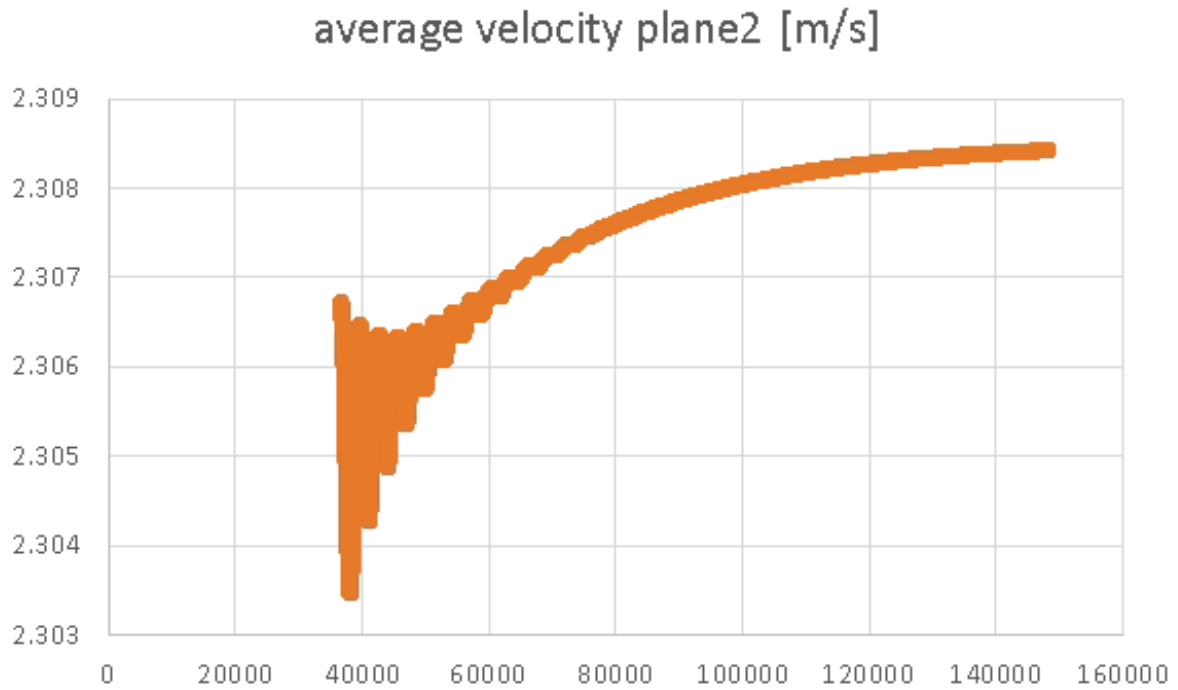
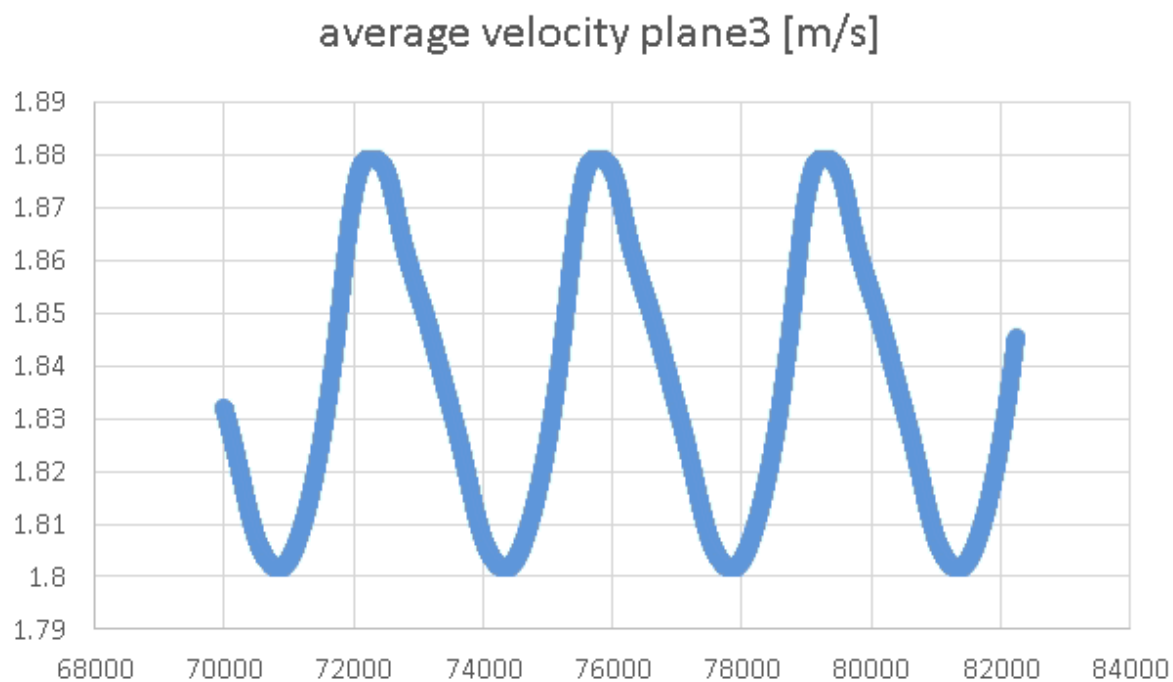**Figure D.9:** velocity/iterations veloplane 2
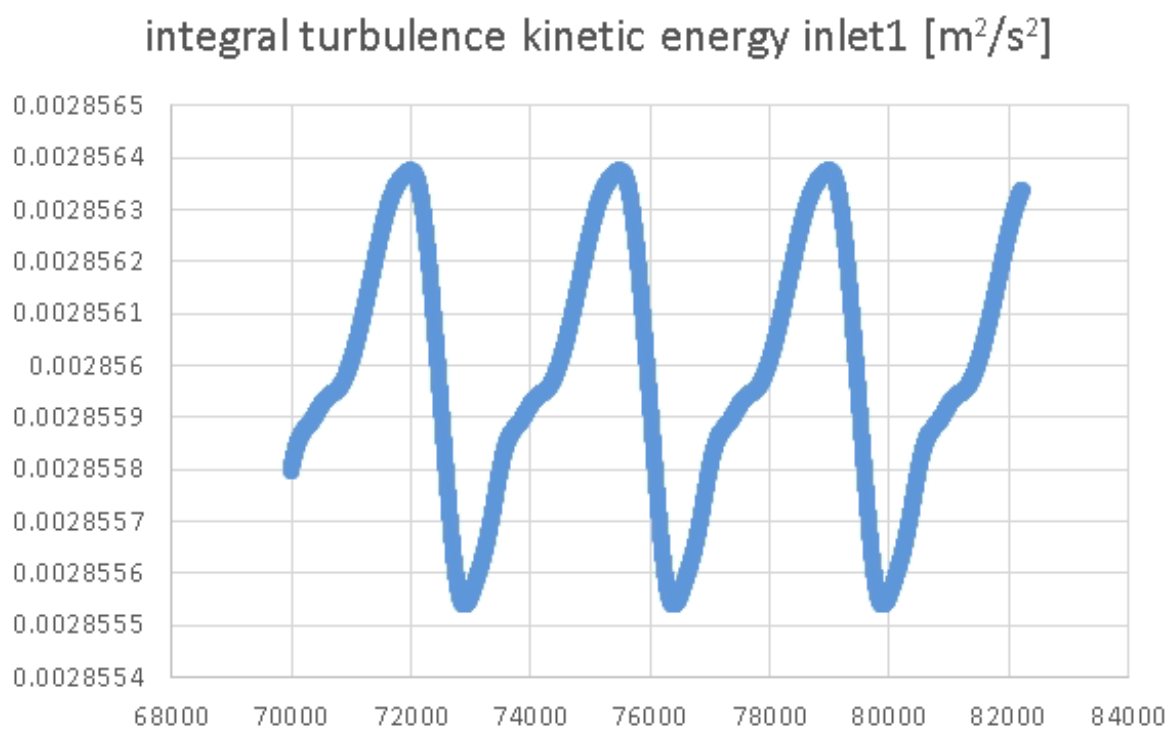

Figure D.10: velocity/iterations veloplane 3

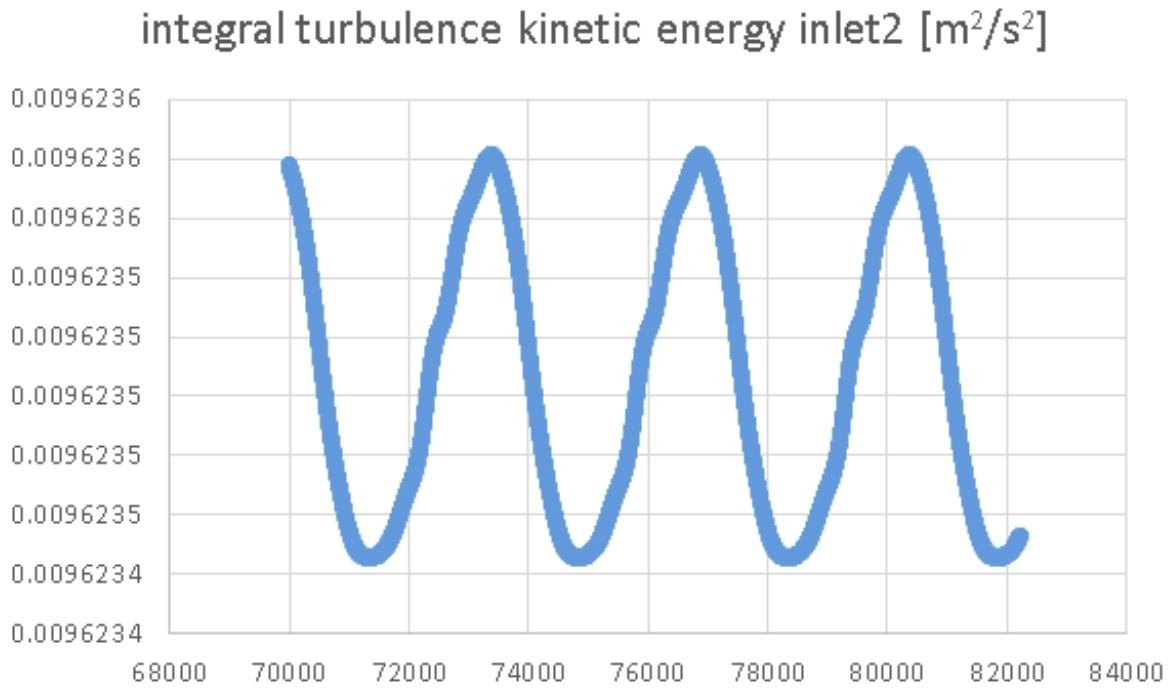**Figure D.11:** integral turbulent kinetic energy/iterations veloplane 1

Figure D.12: integral turbulent kinetic energy /iterations veloplane 2

Figure D.13: integral turbulent kinetic energy /iterations veloplane 3
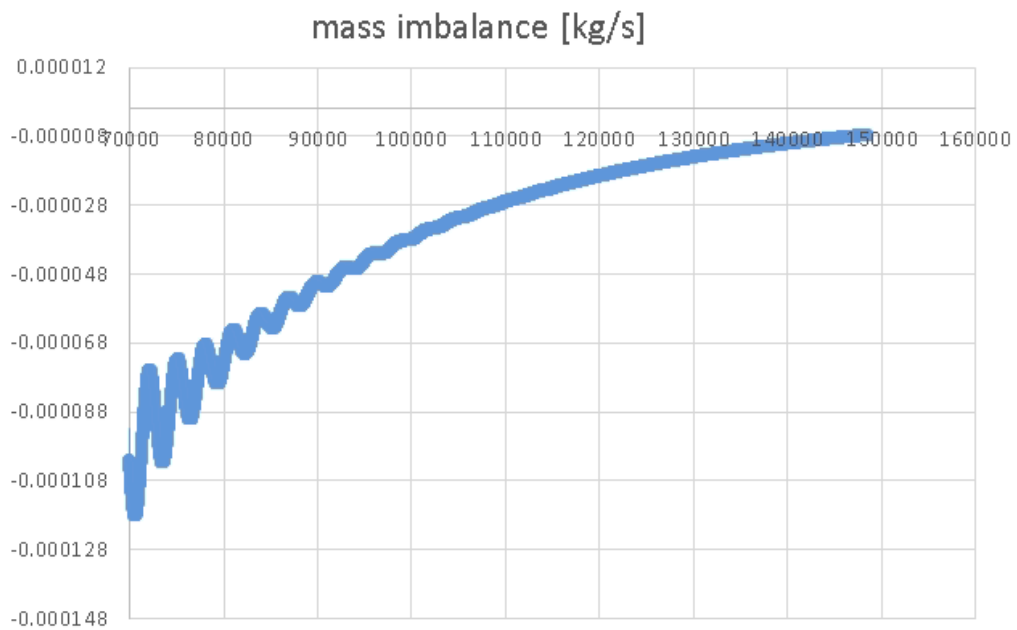
Figure D.14: mass imbalance/iterations

k-ε RNG turbulence model
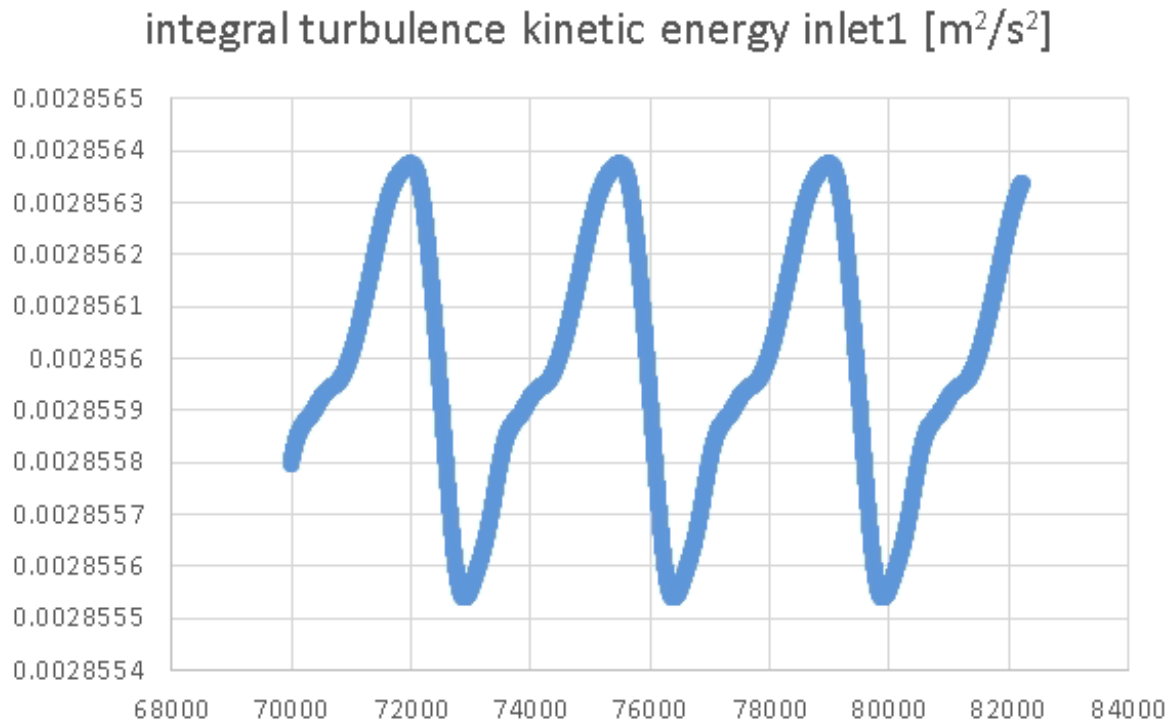
Figure D.15: velocity /iterations veloplane 1
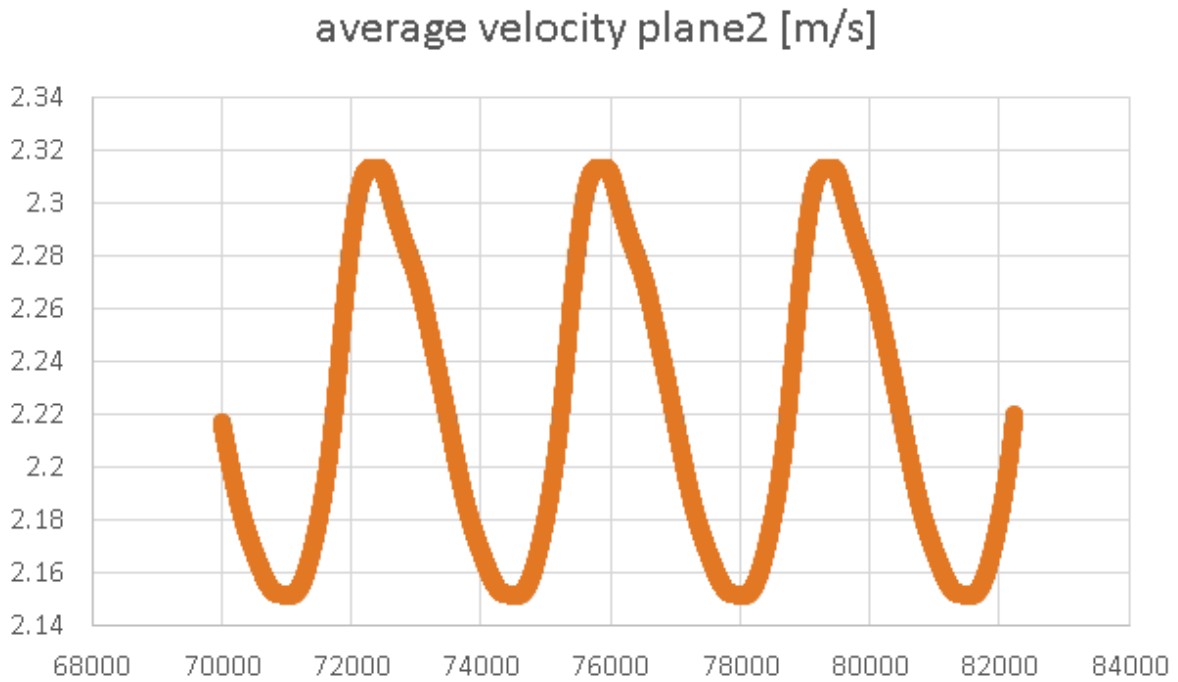
Figure D.16: velocity /iterations veloplane 2

Figure D.17: velocity /iterations veloplane 3

Figure D.18: integral turbulent kinetic energy/iterations veloplane 1

integral turbulence kinetic energy inlet2 [m^2/s^2]

Figure D.19: integral turbulent kinetic energy/iterations veloplane 2

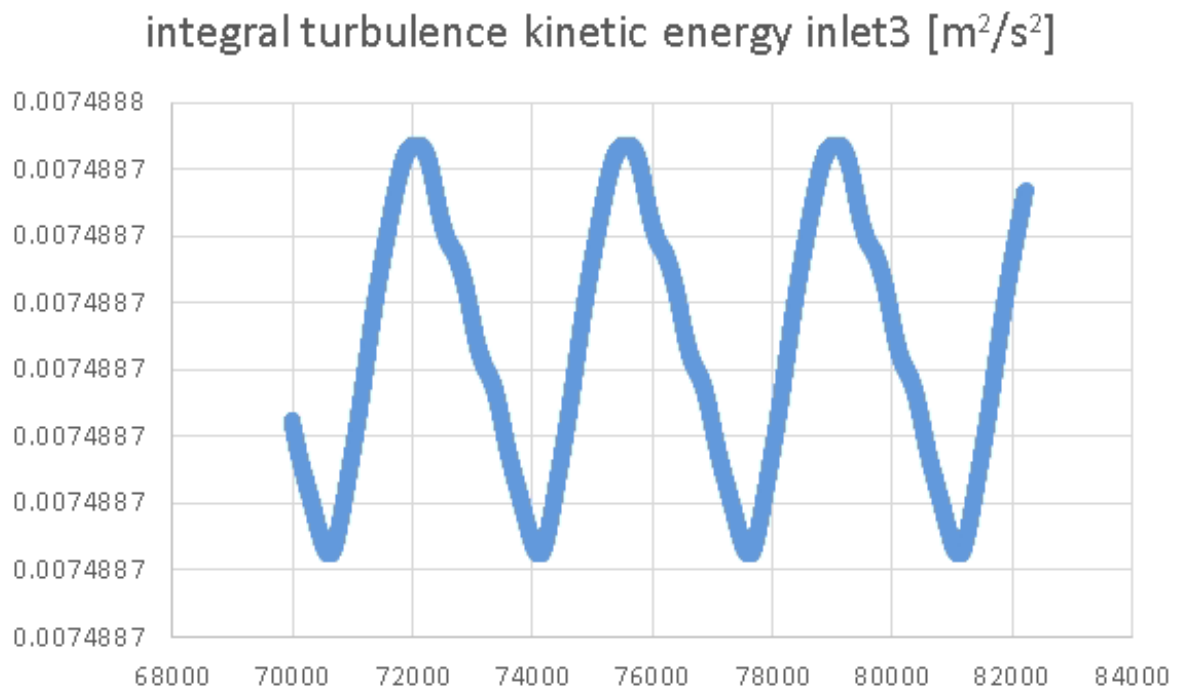integral turbulence kinetic energy inlet3 [m^2/s^2]

Figure D.20: integral turbulent kinetic energy/iterations veloplane 3
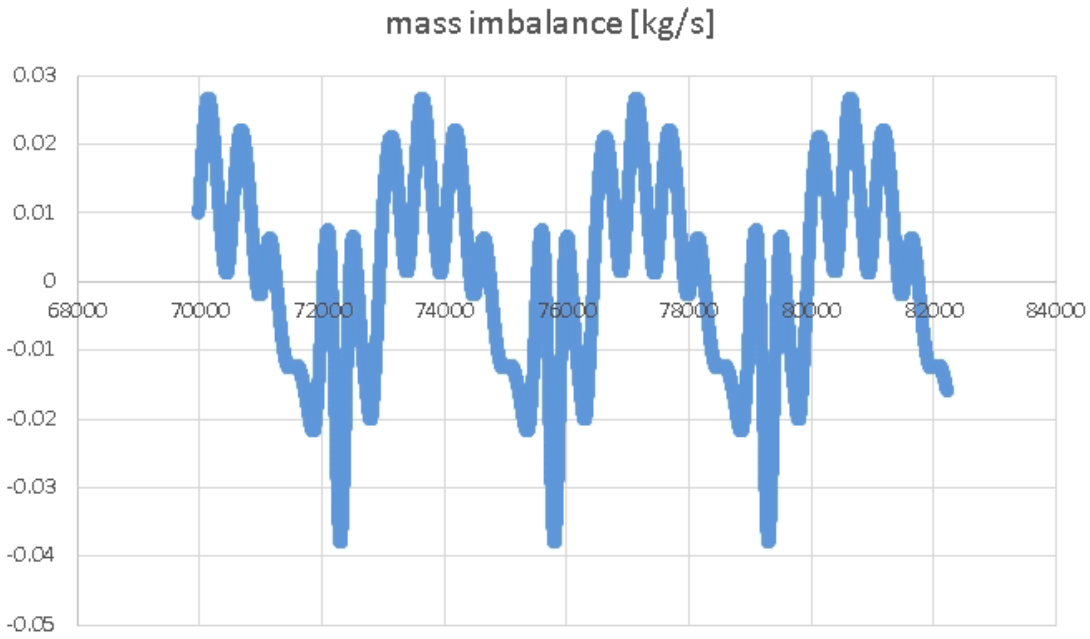
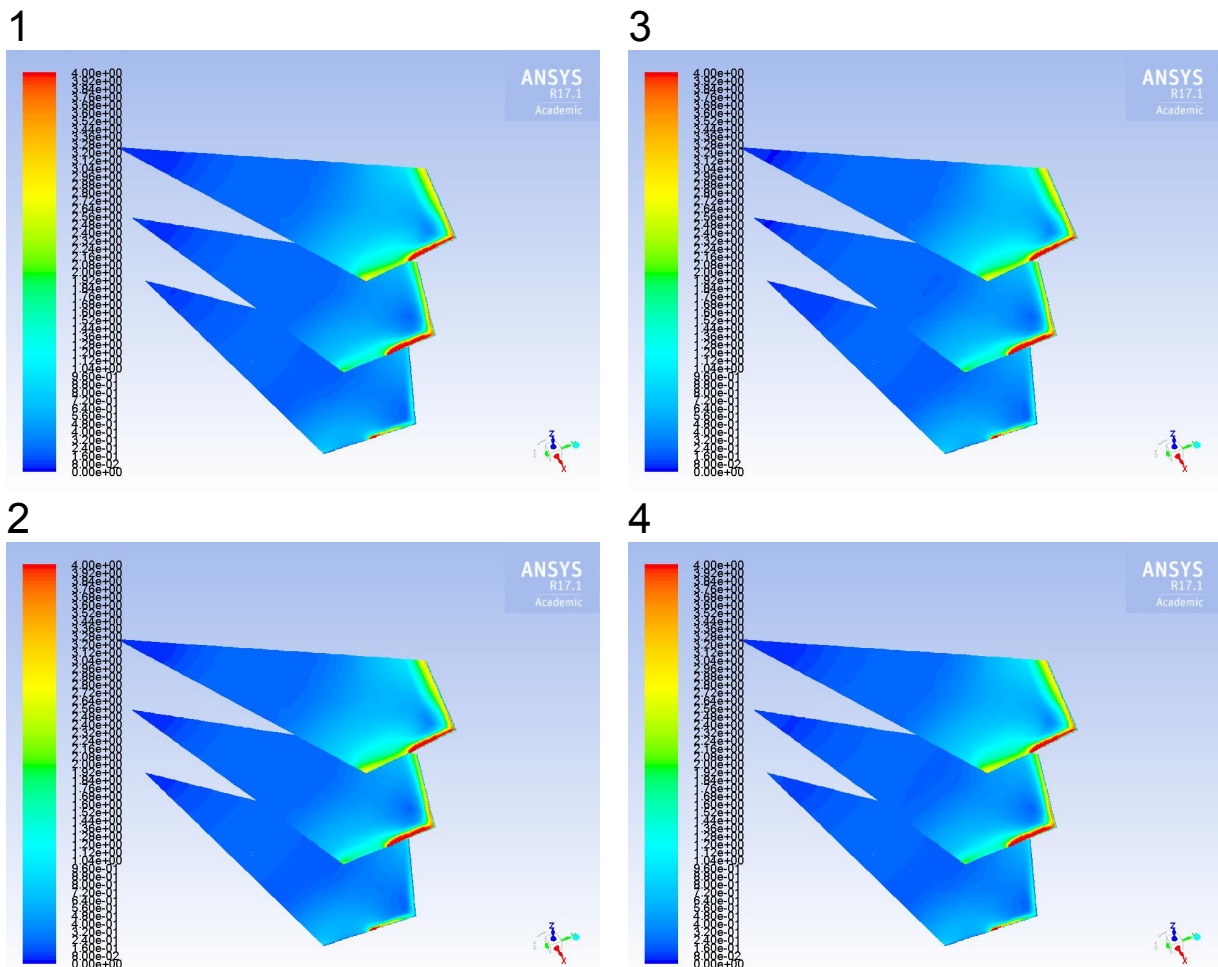**Figure D.21:** mass imbalance/iterations

Figure D.22 Velocity magnitude @ veloplanes during one periodic residual fluctuation of 4000 iterations from 1-4 in augmenting iteration steps
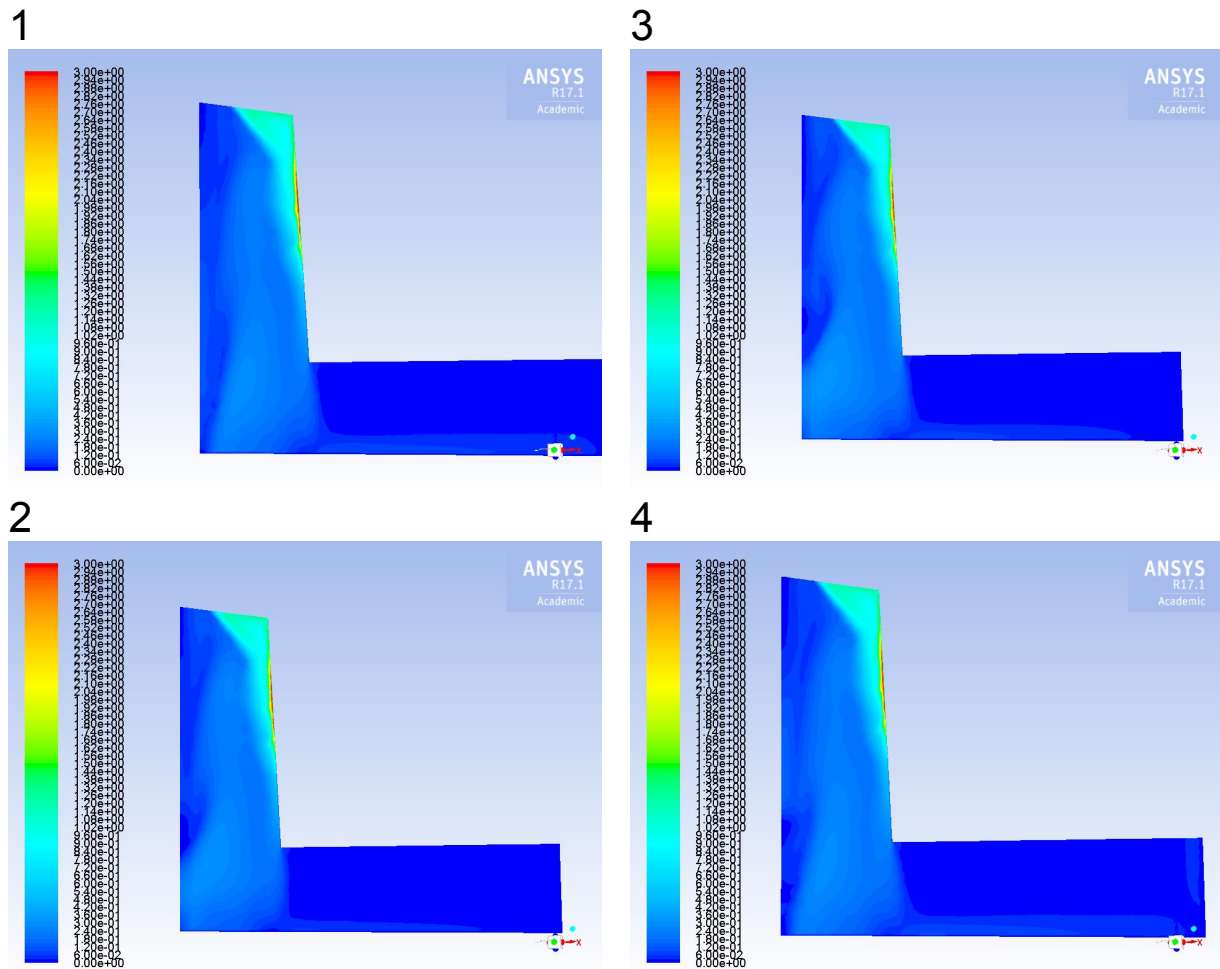
Figure D.23 Velocity magnitude @ veloplanes during one periodic residual fluctuation of 4000 iterations from 1-4 in augmenting iteration steps
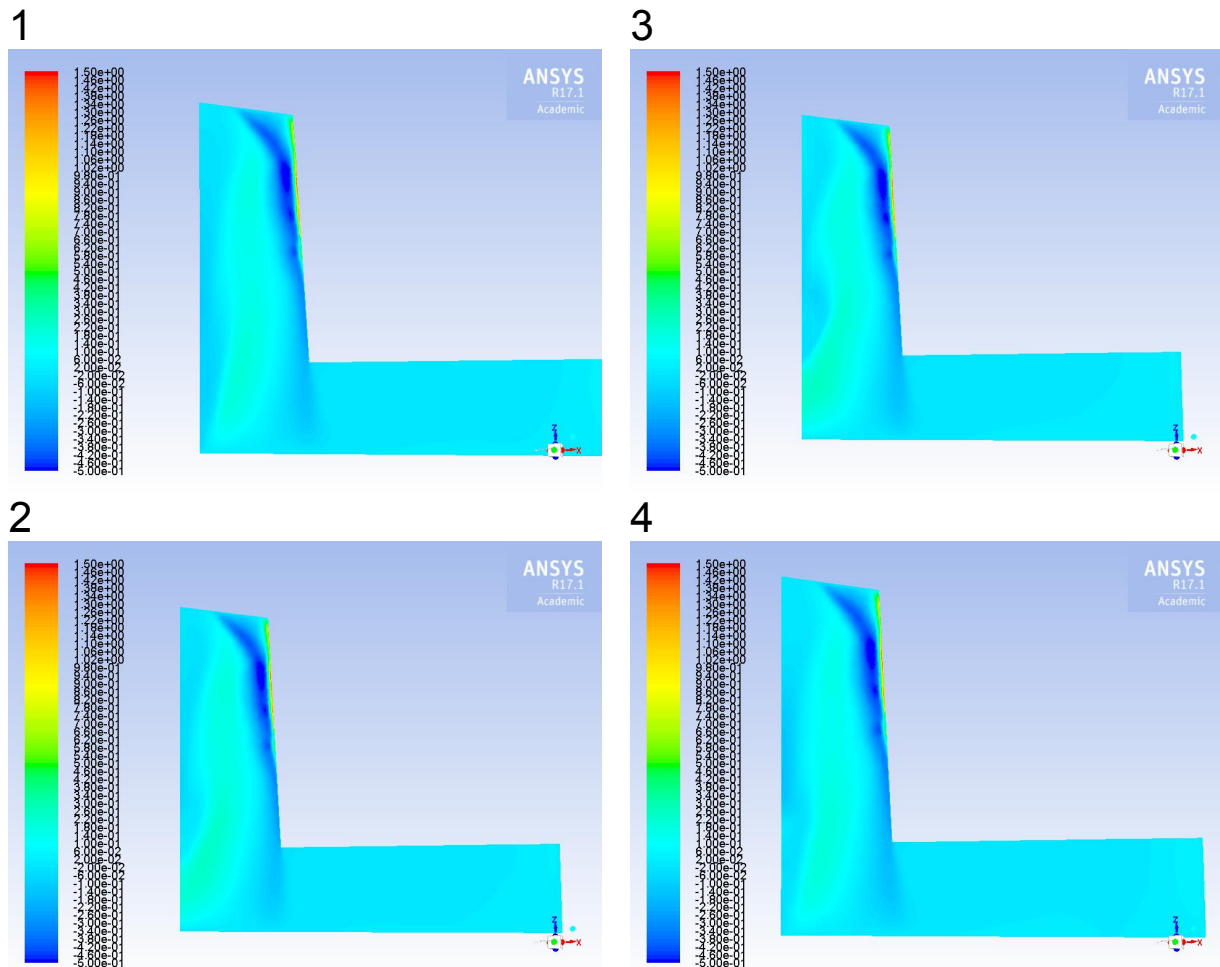
Figure D.24 Axial velocities @ veloplanes during one periodic residual fluctuation of 4000 iterations from 1-4 in augmenting iteration steps
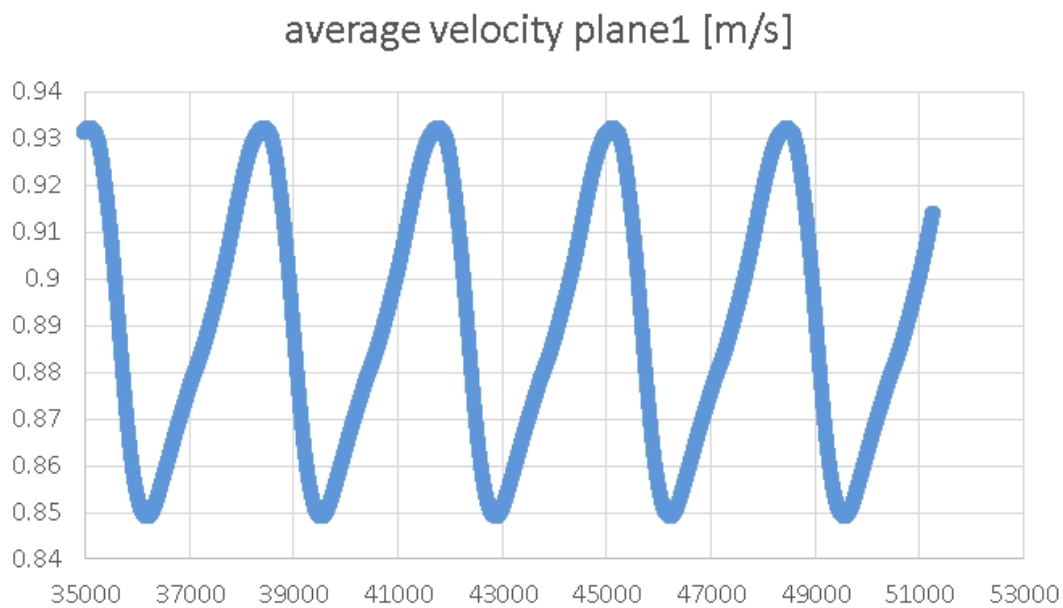
k-w SST turbulence model

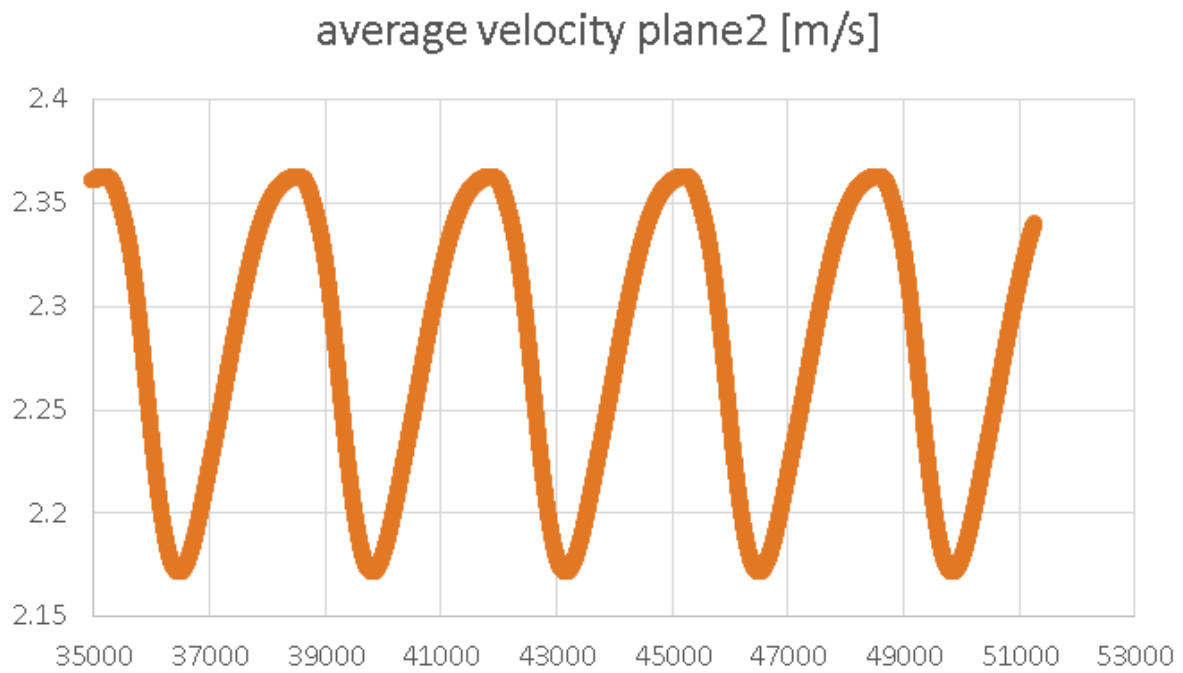

Figure D.25: velocity /iterations veloplane 1

Figure D.26: velocity /iterations veloplane 2

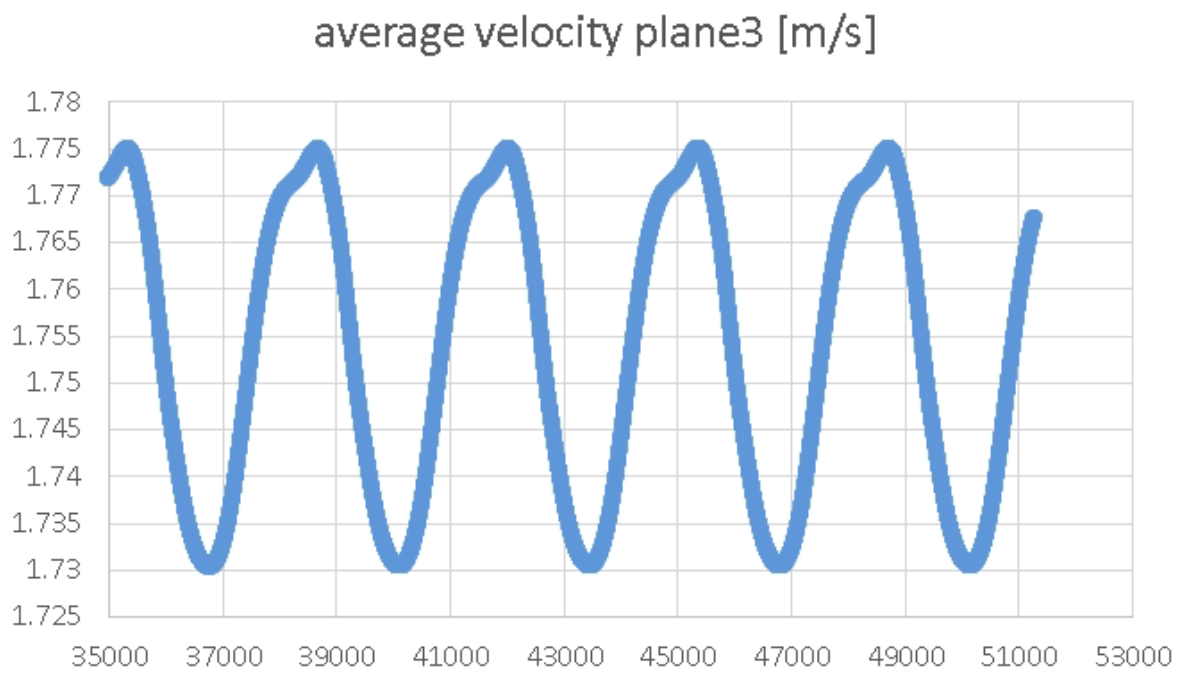

Figure D.27: velocity /iterations veloplane 3

Figure D.28: integral turbulent kinetic energy/iterations veloplane 2

Figure D.29: integral turbulent kinetic energy/iterations veloplane 3
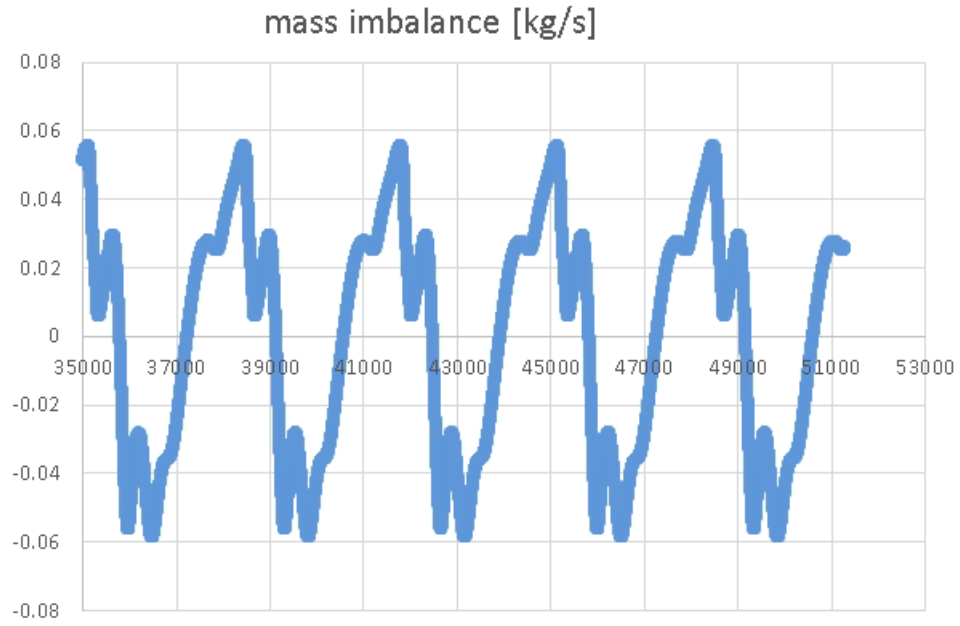
Figure D.30: mass imbalance/iterations
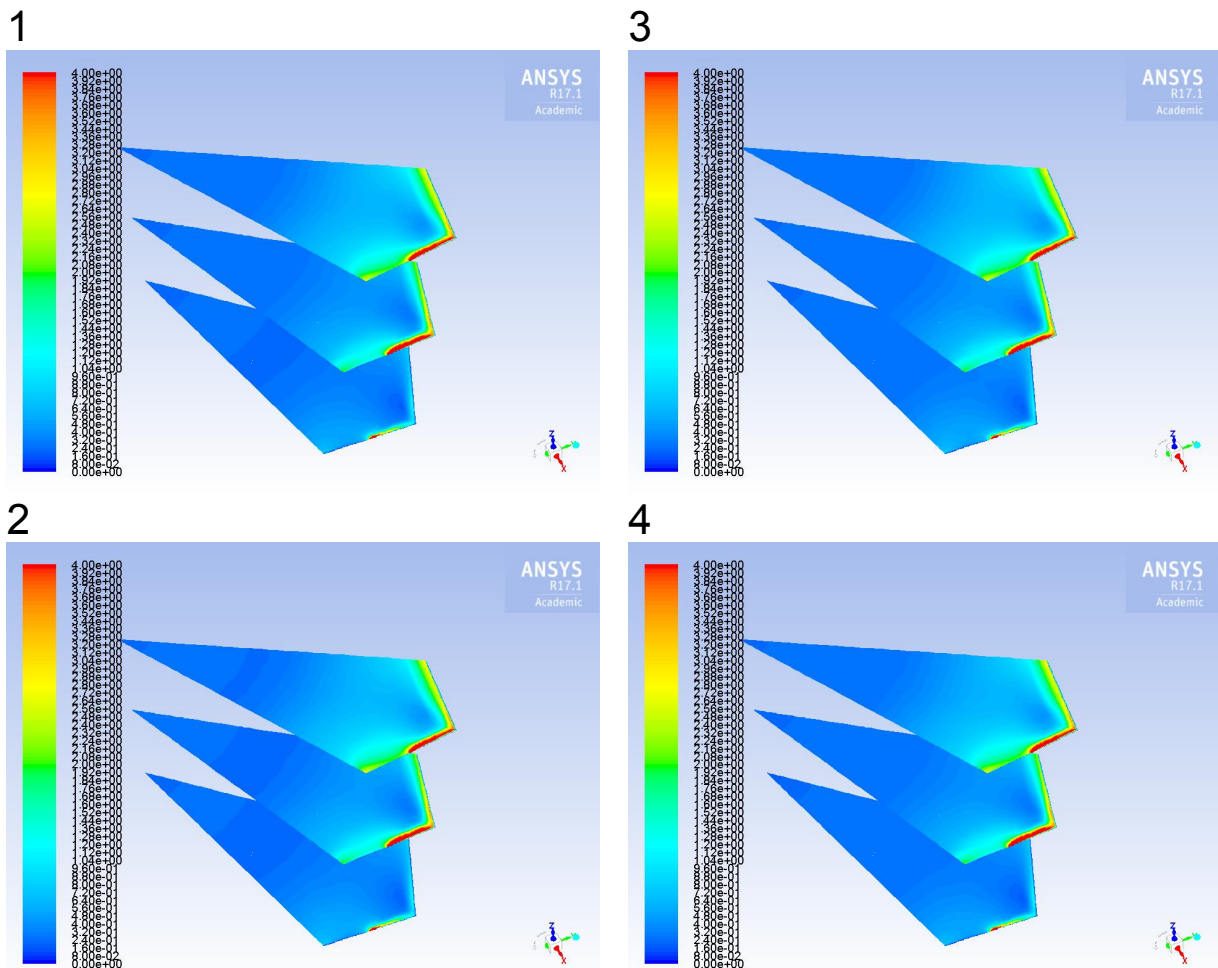
Figure D.31 Velocity magnitude @ veloplanes during one periodic residual fluctuation of 4000 iterations from 1-4 in augmenting iteration steps
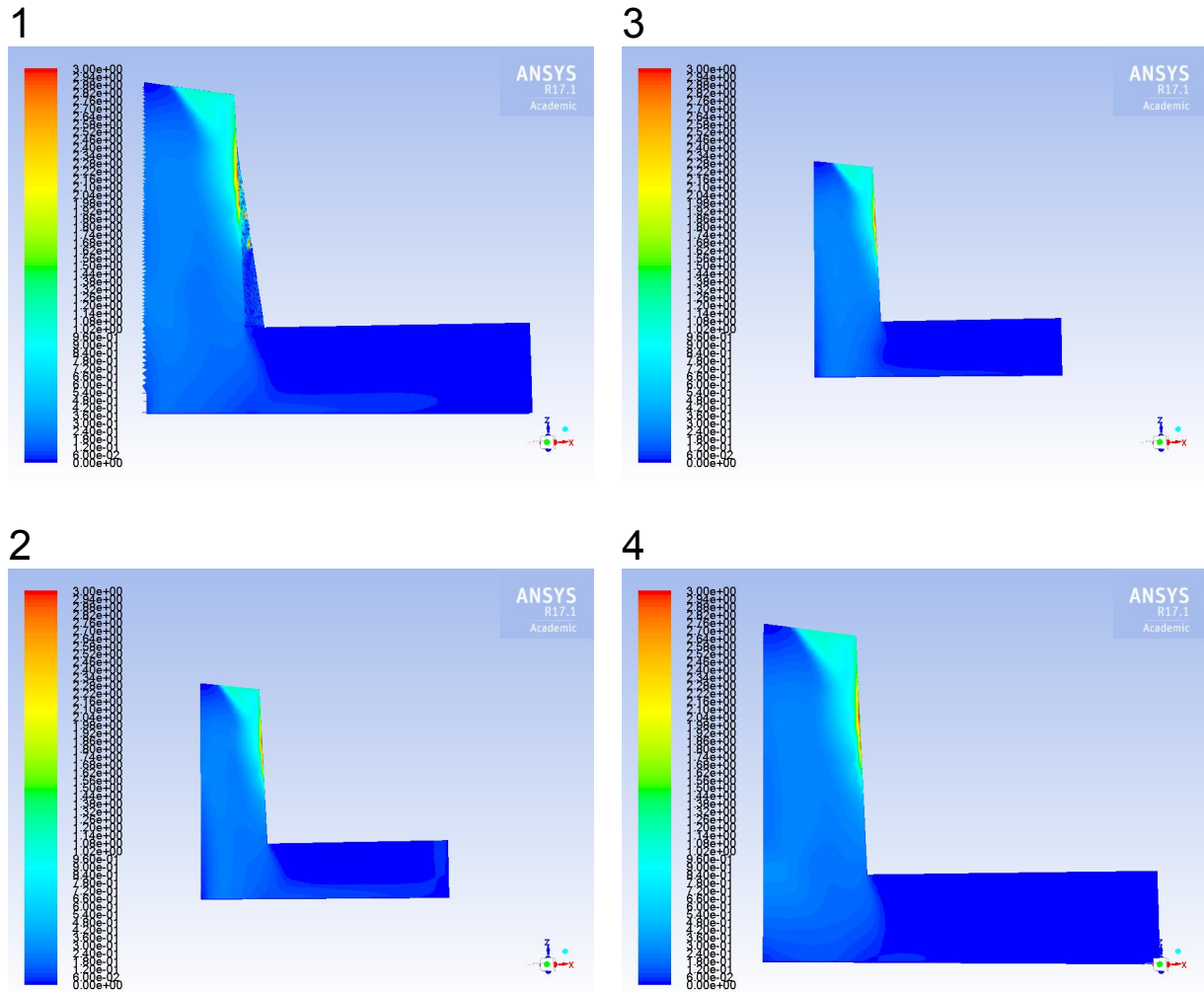
Figure D.32 Velocity magnitude @ periodic plane during one periodic residual fluctuation of 4000 iterations from 1-4 in augmenting iteration steps
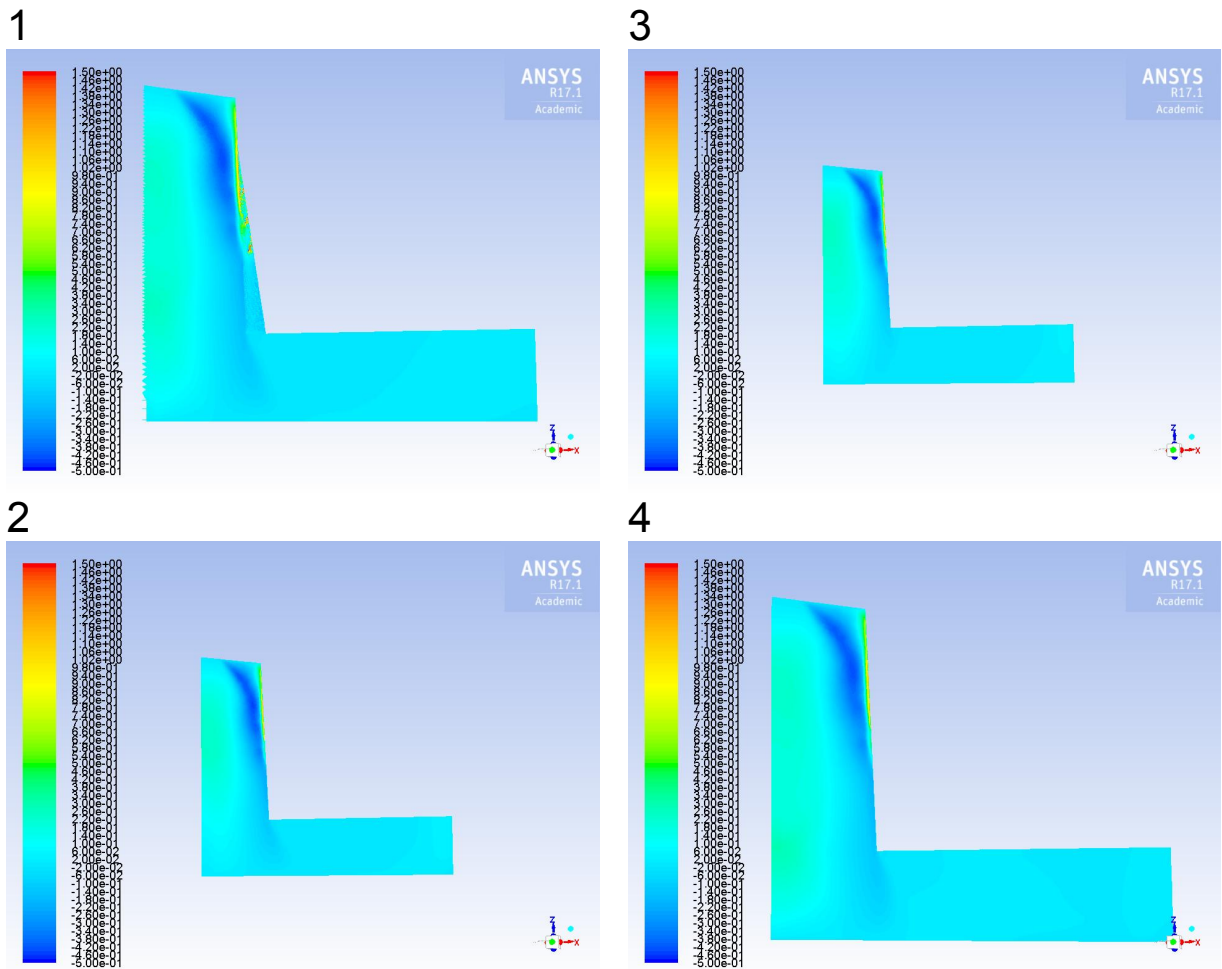
Figure D.33 Axial velocities @ periodic planes during one periodic residual fluctuation of 4000 iterations from 1-4 in augmenting iteration steps

E   Convergence monitoring Case III
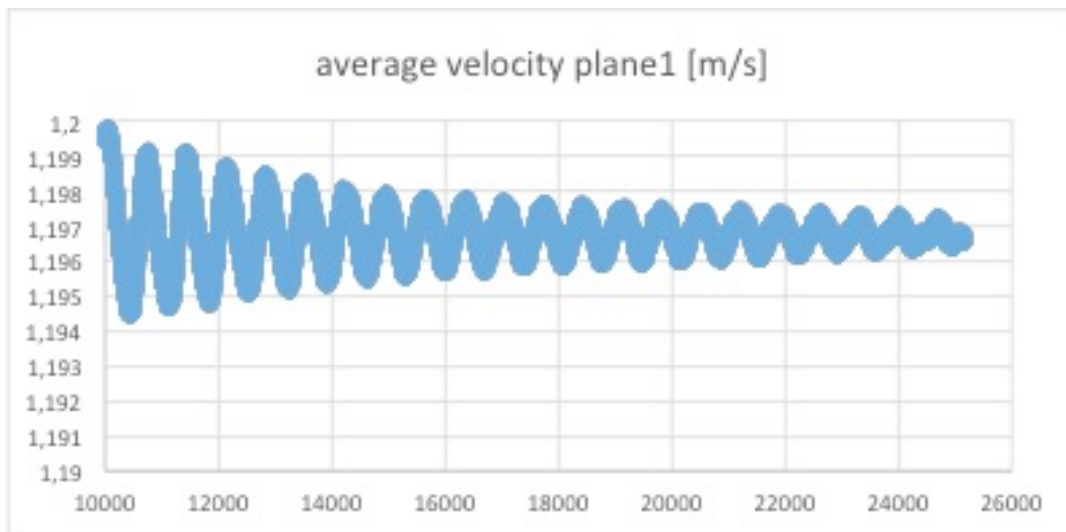
Figure E.1: velocity/iteration veloplane 1
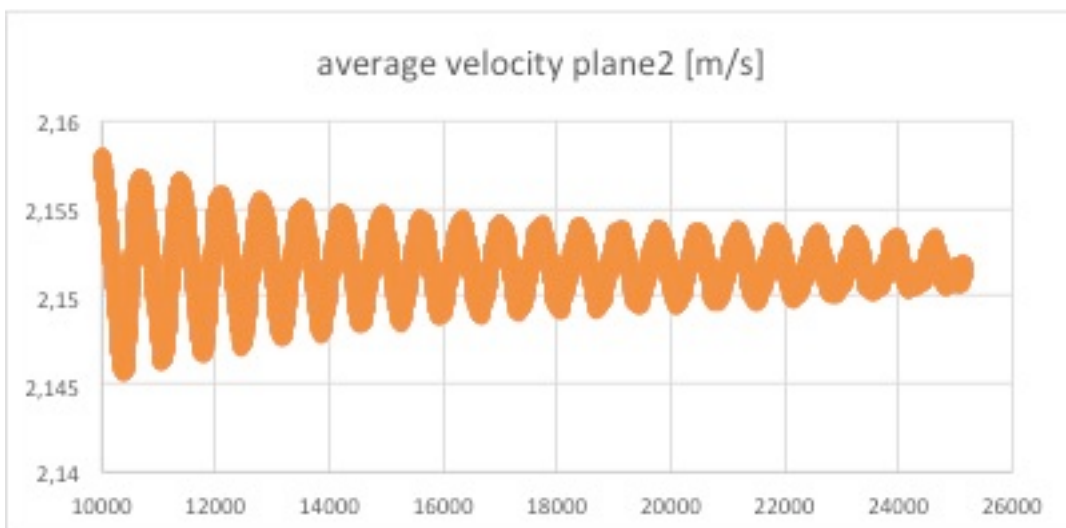
Figure E.2: velocity/iteration veloplane 2

Figure E.3: velocity/iteration veloplane 3
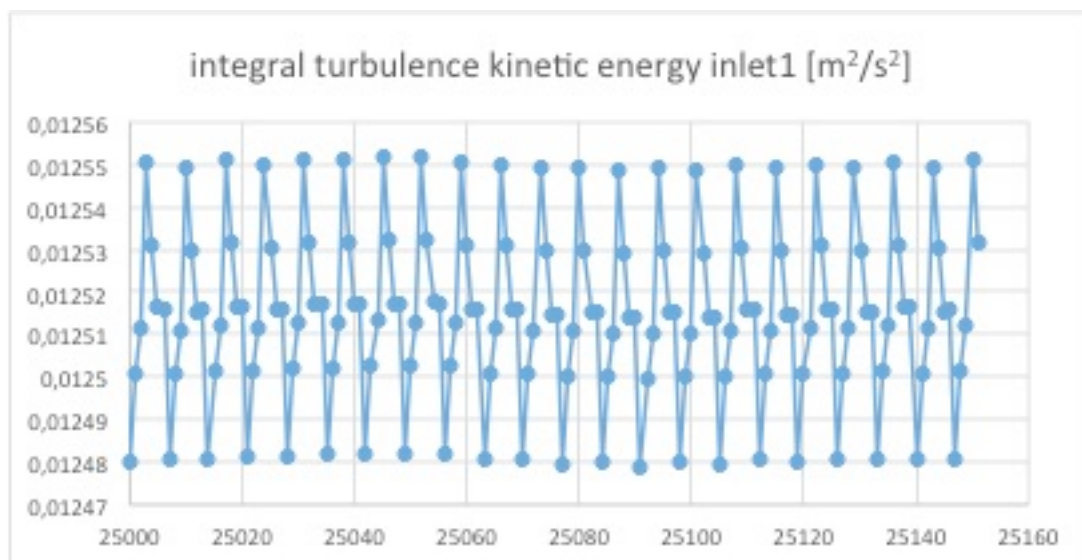
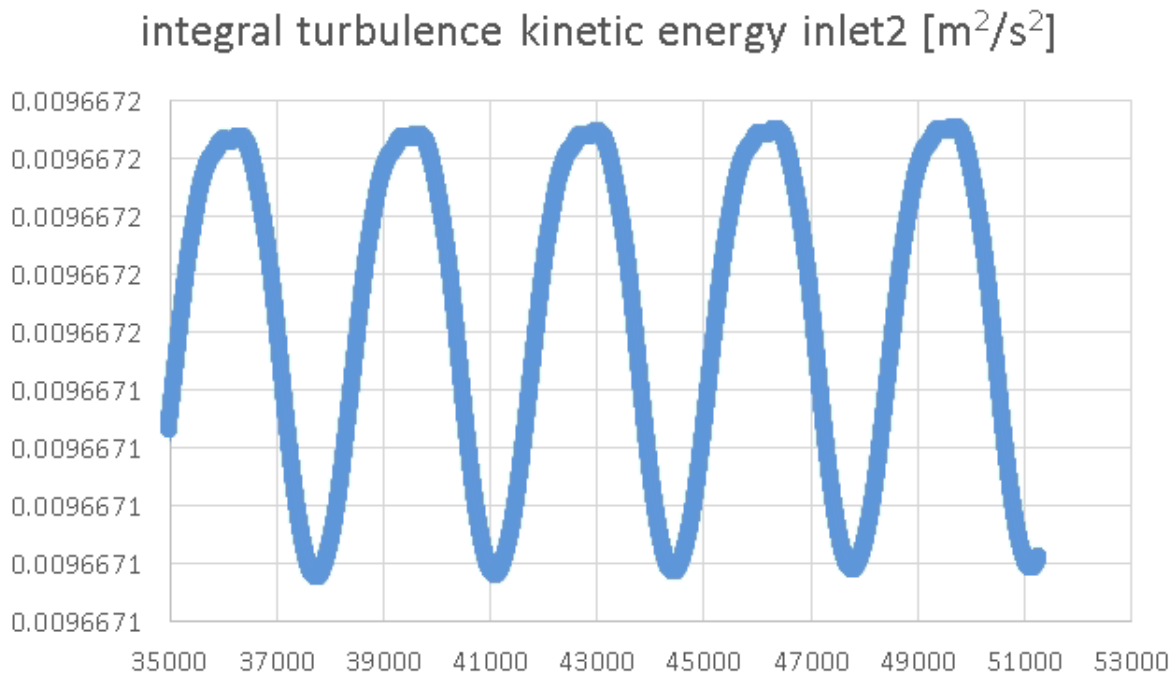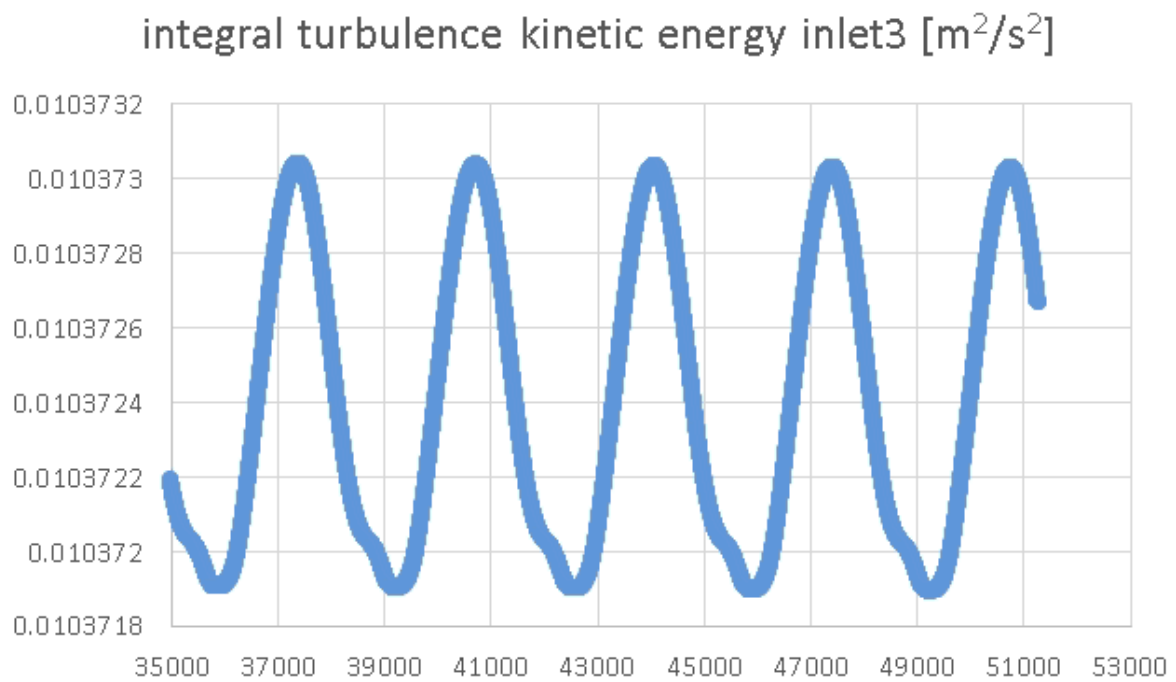**Figure E.4:** integral turbulent kinetic energy/iteration inlet 1
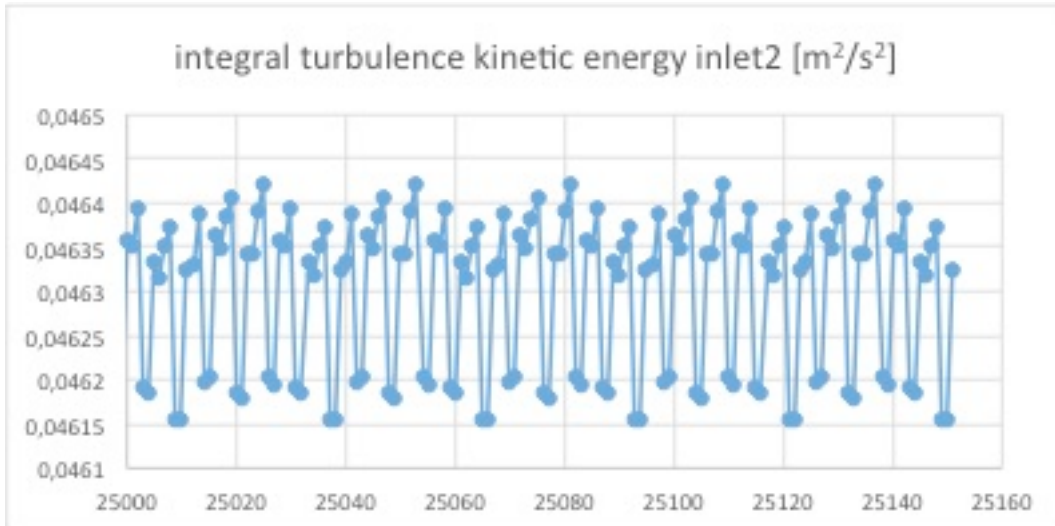
**Figure E.5:** integral turbulent kinetic energy/iteration inlet 2
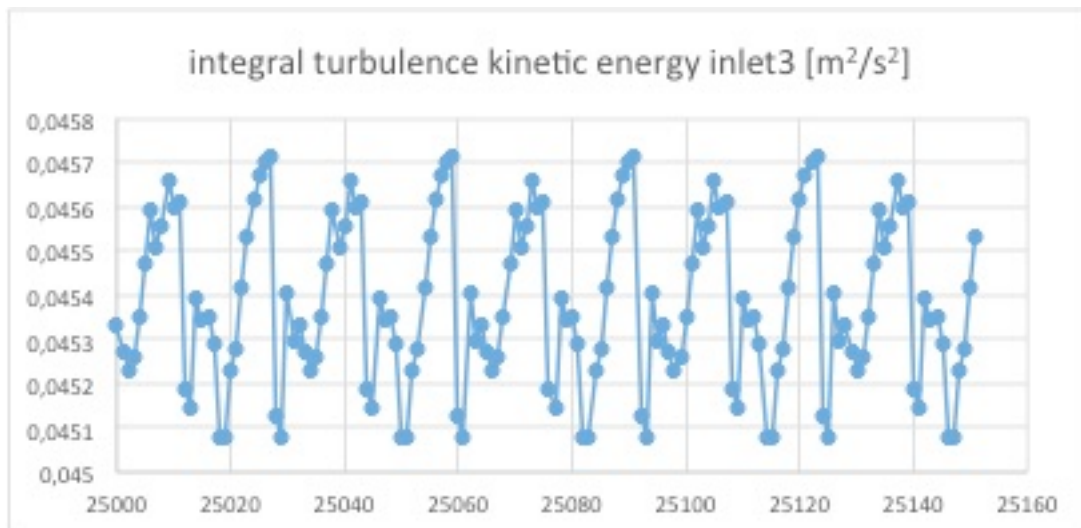
Figure E.6: integral turbulent kinetic energy/iteration inlet 3
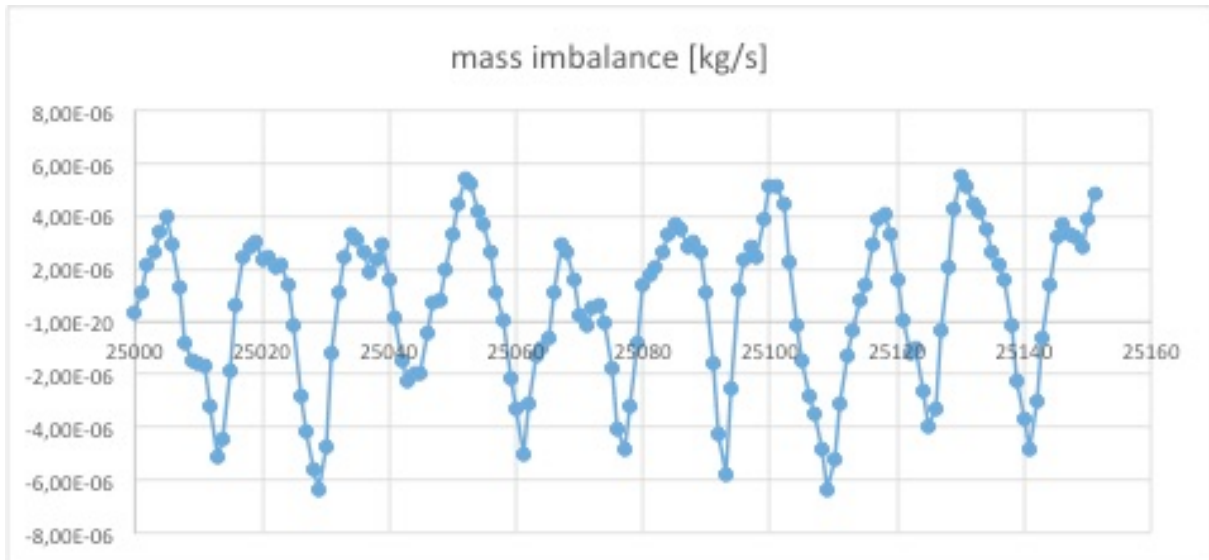
Figure E.7: mass imbalance/iteration

F Cooling Tower Calculations

Table F.1: Air and water properties depending on temperature

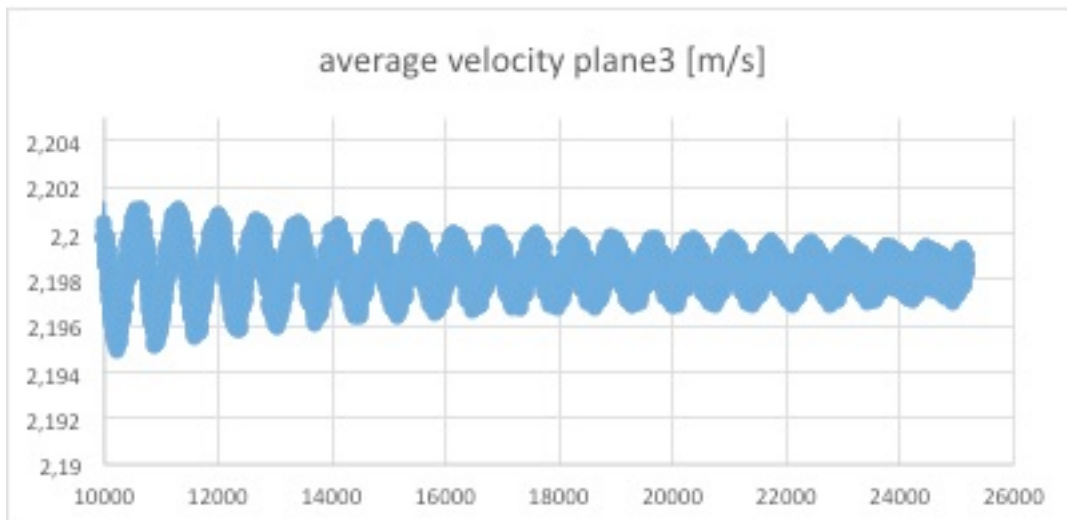| T	rho_L	cp,L	cp,v	h,L	m,w/m,L	h,vapour
[°C]	[kg/m³]	[kJ/kgK]	[kJ/kgK]	[kJ/kg]	[1]	[kJ/kg]
-20	1,39516	1,00683	1,85592	5,034	0,00077286	1,94088
-19	1,38967	1,00679	1,85606	6,041	0,000841995	2,11604
-18	1,38423	1,00675	1,8562	7,047	0,000916614	2,30527
-17	1,37881	1,00671	1,85634	8,054	0,000997086	2,50951
-16	1,37345	1,00667	1,85648	9,060	0,00108383	2,72985
-15	1,3681	1,00663	1,85662	10,066	0,00117725	2,96733
-14	1,36284	1,00659	1,85676	11,073	0,001277803	3,22316
-13	1,35760	1,00655	1,8569	12,079	0,001385962	3,49856
-12	1,35240	1,00651	1,85704	13,085	0,001502214	3,79480
-11	1,34724	1,00647	1,85718	14,091	0,001627087	4,11327
-10	1,34211	1,00643	1,85732	15,096	0,00176114	4,45543
-9	1,33703	1,00639	1,85746	16,102	0,001904938	4,82276
-8	1,33199	1,00635	1,8576	17,108	0,002059114	5,21692
-7	1,32698	1,00631	1,85774	18,114	0,002224294	5,63956
-6	1,3220	1,00627	1,85788	19,119	0,002401157	6,09245
-5	1,31708	1,00623	1,85802	20,125	0,002590427	6,57751
-4	1,31218	1,00619	1,85816	21,130	0,00279284	7,09666

T	rho_L	cp,L	cp,v	h,L	m,w/m,L	h,vapour
[°C]	[kg/m³]	[kJ/kgK]	[kJ/kgK]	[kJ/kg]	[1]	[kJ/kg]
-3	1,3073	1,00615	1,8583	22,135	0,003009185	7,65201
-2	1,3024	1,00611	1,85844	23,141	0,003240277	8,24567
-1	1,2977	1,00607	1,85858	24,146	0,003486985	8,87997
0	1,2929	1,00602	1,85872	25,151	0,003750223	9,55732

Table F.2: Humid air enthalpies depending on temperature @ 1atm

T	h100	h10	h20	h30	h40	h50	h60	h70	h90
[°C]	[kJ/kg]	[kJ/kg]	[kJ/kg]	[kJ/kg]	[kJ/kg]	[kJ/kg]	[kJ/kg]	[kJ/kg]	[kJ/kg]
-20	6,98	5,26	5,49	5,70	5,92	6,15	6,38	6,59	7,04
-19	8,16	6,29	6,52	6,77	7,01	7,26	7,49	7,74	8,21
-18	9,35	7,32	7,57	7,83	8,10	8,35	8,62	8,89	9,41
-17	10,56	8,34	8,61	8,90	9,19	9,48	9,75	10,04	10,62
-16	11,79	9,37	9,68	9,99	10,30	10,59	10,91	11,22	11,84
-15	13,03	10,40	10,73	11,06	11,39	11,75	12,08	12,41	13,08
-14	14,30	11,43	11,80	12,15	12,53	12,88	13,23	13,61	14,33
-13	15,58	12,47	12,87	13,24	13,64	14,03	14,43	14,82	15,59
-12	16,88	13,50	13,94	14,35	14,77	15,21	15,62	16,04	16,89
-11	18,20	14,55	15,01	15,46	15,92	16,38	16,84	17,28	18,19
-10	19,55	15,60	16,08	16,58	17,08	17,55	18,05	18,53	19,53
-9	20,93	16,62	17,17	17,69	18,23	18,75	19,29	19,81	20,88
-8	22,32	17,67	18,26	18,82	19,40	19,97	20,55	21,11	22,26
-7	23,75	18,74	19,35	19,97	20,58	21,20	21,81	22,44	23,67

T	h100	h10	h20	h30	h40	h50	h60	h70	h90
[°C]	[kJ/kg]	[kJ/kg]	[kJ/kg]	[kJ/kg]	[kJ/kg]	[kJ/kg]	[kJ/kg]	[kJ/kg]	[kJ/kg]
-6	25,21	19,79	20,44	21,10	21,77	22,44	23,09	23,76	25,09
-5	26,70	20,84	21,55	22,26	22,97	23,70	24,41	25,12	26,54
-4	28,23	21,90	22,66	23,43	24,21	24,96	25,73	26,51	28,04
-3	29,79	22,95	23,79	24,61	25,42	26,26	27,08	27,89	29,55
-2	31,39	24,02	24,90	25,80	26,68	27,56	28,44	29,32	31,10
-1	33,03	25,09	26,05	27,00	27,94	28,89	29,85	30,79	32,68
0	34,71	26,16	27,19	28,19	29,22	30,23	31,26	32,27	34,30

Table F.3: Absolute humidity values

T	10%	20%	30%	40%	50%	60%	70%	90%	100%
[°C]	[g/m^3]	[g/m^3]	[g/m^3]	[g/m^3]	[g/m^3]	[g/m^3]	[g/m^3]	[g/m^3]	[g/m^3]
-20	0,11	0,22	0,32	0,43	0,54	0,65	0,75	0,97	1,08
-19	0,12	0,23	0,35	0,47	0,59	0,7	0,82	1,05	1,17
-18	0,13	0,25	0,38	0,51	0,63	0,76	0,89	1,14	1,27
-17	0,14	0,27	0,41	0,55	0,69	0,82	0,96	1,24	1,37
-16	0,15	0,3	0,45	0,6	0,74	0,89	1,04	1,34	1,49

T	10%	20%	30%	40%	50%	60%	70%	90%	100%
[°C]	[g/m³]	[g/m³]	[g/m³]	[g/m³]	[g/m³]	[g/m³]	[g/m³]	[g/m³]	[g/m³]
-15	0,16	0,32	0,48	0,64	0,81	0,97	1,13	1,45	1,61
-14	0,17	0,35	0,52	0,7	0,87	1,04	1,22	1,57	1,74
-13	0,19	0,38	0,56	0,75	0,94	1,13	1,32	1,69	1,88
-12	0,2	0,41	0,61	0,81	1,02	1,22	1,42	1,83	2,03
-11	0,22	0,44	0,66	0,88	1,1	1,32	1,53	1,97	2,19
-10	0,24	0,47	0,71	0,95	1,18	1,42	1,65	2,13	2,36
-9	0,25	0,51	0,76	1,02	1,27	1,53	1,78	2,29	2,55
-8	0,27	0,55	0,82	1,1	1,37	1,65	1,92	2,47	2,74
-7	0,3	0,59	0,89	1,18	1,48	1,77	2,07	2,66	2,95
-6	0,32	0,63	0,95	1,27	1,59	1,9	2,22	2,86	3,17
-5	0,34	0,68	1,02	1,36	1,71	2,05	2,39	3,07	3,41
-4	0,37	0,73	1,1	1,47	1,83	2,2	2,57	3,3	3,66
-3	0,39	0,79	1,18	1,57	1,97	2,36	2,75	3,54	3,93
-2	0,42	0,84	1,27	1,69	2,11	2,53	2,95	3,8	4,22
-1	0,45	0,91	1,36	1,81	2,26	2,72	3,17	4,07	4,53
0	0,48	0,97	1,45	1,94	2,42	2,91	3,39	4,36	4,85